



DEFENSE INTELLIGENCE AGENCY  
WASHINGTON, D.C. 20340-5100



FAC-2C

January 08, 2021

Anthony Bragaglia



This responds to your Freedom of Information Act (FOIA) request, dated December 27, 2017 that you submitted to the Defense Intelligence Agency (DIA) for information concerning Requesting all information on test results from the UAP material from Bigelow Aerospace. I apologize for the delay in responding to your request. DIA continues its efforts to eliminate the large backlog of pending FOIA requests. In order to properly respond, it was necessary to consult with another office within the agency.

A search of DIA's systems of records located five documents (154 pages) responsive to your request.

Upon review, I have determined that some portions of five documents (154 pages) must be withheld in part from disclosure pursuant to the FOIA. The withheld portions are exempt from release pursuant to Exemptions 3 and 6 of the FOIA, 5 U.S.C. § 552 (b)(3) and (b)(6). Exemption 3 applies to information specifically exempted by a statute establishing particular criteria for withholding. The applicable statute is 10 U.S.C. § 424. Statute 10 U.S.C. § 424 protects the identity of DIA employees, the organizational structure of the agency, and any function of DIA. Exemption 6 applies to information which if released would constitute an unwarranted invasion of the personal privacy of other individuals. DIA has not withheld any reasonably segregable non-exempt portions of the records.

If you are not satisfied with my response to your request, you may contact the DIA FOIA Requester Service Center, as well as our FOIA Public Liaison at 301-394-6253.

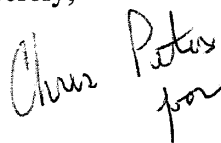
Additionally, you may contact the Office of Government Information Services (OGIS) at the National Archives and Records Administration to inquire about the FOIA mediation services they offer. You may contact OGIS by email at [ogis@nara.gov](mailto:ogis@nara.gov); telephone at 202-741-5770, toll free at 1-877-684-6448 or facsimile at 202-741-5769; or you may mail them at the following address:

Office of Government Information Services  
National Archives and Records Administration  
8601 Adelphi Road-OGIS  
College Park, MD 20740-6001

You may also exercise your right to file an administrative appeal by writing to the address below and referring to case number FOIA-00089-2018. Your appeal must be postmarked no later than 90 days after the date of this letter.

Defense Intelligence Agency  
7400 Pentagon  
ATTN: FAC-2C (FOIA)  
Washington, D.C. 20301-7400

Sincerely,

A handwritten signature in cursive script that reads "Steven W. Tumiski".

Steven W. Tumiski  
Chief, Records Management and Information Services

5 Enclosures

1. Metallic Glasses - Status and Prospects for Aerospace Applications (30 pgs)
2. Biomaterials (32 pgs)
3. Materials for Advanced Aerospace Platforms (27 pgs)
4. Metallic Spintronics (27 pgs)
5. Metamaterials for Aerospace Applications (38 pgs)

~~UNCLASSIFIED//FOR OFFICIAL USE ONLY~~



# Defense Intelligence Reference Document

*Acquisition Threat Support*

14 December 2009

ICOD: 1 December 2009

DIA-08-0911-012

## **Metallic Glasses: Status and Prospects for Aerospace Applications**

~~UNCLASSIFIED//FOR OFFICIAL USE ONLY~~

## Metallic Glasses: Status and Prospects for Aerospace Applications

**Prepared by:**

(b)(3):10 USC 424

**Defense Intelligence Agency**

**Author:**

(b)(6)

**Administrative Note**

COPYRIGHT WARNING: Further dissemination of the photographs in this publication is not authorized.

This product is one in a series of advanced technology reports produced in FY 2009 under the Defense Intelligence Agency, (b)(3):10 USC 424 Advanced Aerospace Weapon System Applications (AAWSA) Program. Comments or questions pertaining to this document should be addressed to (b)(3):10 USC 424;(b)(6), AAWSA Program Manager, Defense Intelligence Agency, (b)(3):10 USC 424 Bldg 6000, Washington, DC 20340-5100.



## Contents

Summary.....	V
Metallic Glasses.....	1
Structure.....	1
Processing.....	2
Glass-Forming Alloys.....	2
Casting and Molding .....	4
Joining .....	5
Foams .....	5
Thin Films and Coatings .....	5
Mechanical Behavior Near Room Temperature .....	5
Stiffness: Elastic Deformation .....	6
Strength and Ductility: Plastic Deformation .....	6
Fracture Toughness.....	8
Fatigue.....	9
Wear Resistance.....	10
Corrosion and Stress-Corrosion Cracking .....	10
Mechanical Behavior at Elevated Temperature .....	11
Other Properties: Magnetic, Electrical, Optical, Thermal, and Acoustic .....	12
Metallic Glass Matrix Composites .....	13
Processing and Structure of Composites .....	13
Ex Situ Composites.....	14
In Situ Composites .....	14
Mechanical Properties of Composites .....	15
Strength and Ductility: Plastic Deformation .....	16
Fracture and Fatigue .....	16
Aerospace Applications of Metallic Glasses .....	16
Structural Applications.....	16
Other Applications.....	19

<b>Current Challenges and Prospects for the Future .....</b>	<b>20</b>
<b>Alloy Design .....</b>	<b>20</b>
<b>Thermophysical Properties and Thermoplastic Processing .....</b>	<b>20</b>
<b>Composites and the Quest for Ductility .....</b>	<b>21</b>
<b>Summary and Recommendations .....</b>	<b>22</b>

**Figures**

<b>1. Amorphous Versus Crystalline Structure .....</b>	<b>1</b>
<b>2. Critical Cooling Rate .....</b>	<b>2</b>
<b>3. Examples of Processing of Metallic Glasses .....</b>	<b>4</b>
<b>4. Shear Bands .....</b>	<b>8</b>
<b>5. Fatigue Limit of Metallic-Glass-Matrix Composites .....</b>	<b>10</b>
<b>6. Deformation Map for a Metallic Glasses .....</b>	<b>11</b>
<b>7. Cast Metallic Glass Wedge .....</b>	<b>13</b>
<b>8. Microstructure of In Situ Metallic Glass Matrix Composite .....</b>	<b>15</b>
<b>9. Materials Property Charts .....</b>	<b>18</b>

**Tables**

<b>1. Selected Bulk Glass-Forming Alloys .....</b>	<b>3</b>
<b>2. Comparison of Strengths of Amorphous and Crystalline Aluminum Alloys .....</b>	<b>7</b>

## **Metallic Glasses: Status and Prospects for Aerospace Applications**

### **Summary**

**Metallic glasses combine some of the advantageous mechanical properties of metals—strength, stiffness, and in some cases toughness—with the processing flexibility usually associated with thermoplastic polymers. The absence of crystalline defects allows metallic glasses to be much stronger than conventional alloys but also means they have near-zero tensile ductility and poor fatigue resistance. In structural applications, therefore, metallic glasses are most likely to be useful in the form of composites consisting of ductile crystalline dendrites in a metallic glass matrix. These dendritic composites sacrifice some strength but can have exceptionally high fracture toughness, as well as good fatigue resistance, and could replace high-strength steels in certain load-limited structural components in aerospace vehicles where space is limited.**

**Because they are true glasses, thermoplastic forming near the glass transition temperature affords metallic glasses tremendous flexibility in processing. For instance, metallic glass components can be formed in a single step (for example, by injection molding) in complex geometries that would be difficult or impossible to produce with conventional alloys. In addition, metallic glass foams can be made with relative ease, raising the possibility of making structural foams with high strength and stiffness. Finally, because they lack a crystalline grain structure, metallic glasses can be used to form nanoscale features with high fidelity. This may make metallic glasses useful in a variety of micro-electromechanical systems (MEMS) applications.**

**Metallic glasses also have significant limitations for aerospace applications, however. Foremost among these is a lack of good glass-forming alloys; in particular, there are no good aluminum-rich glass-forming alloys, the known titanium-based alloys are either relatively dense (owing to high concentrations of alloying elements) or contain beryllium, and the known magnesium- and iron-based alloys are all quite brittle, with low fracture toughness. Although metallic glass matrix composites can have outstanding properties (particularly strength and fracture toughness), the number of good composite systems known at present is also quite limited.**

**Therefore, in order for metallic glasses (and their composites) to be of broad utility in aerospace structural applications, progress in the following areas is required:**

- Development of new lightweight alloys and composite systems, preferably by computational and/or combinatorial approaches rather than by trial and error.**
- Understanding of mechanical behavior, especially:**

- The effect of alloy composition and structure on plastic deformation.
- Microstructural design of composites for optimal toughness.
- Development of processing techniques, including thermophysical processing of complex and/or nanoscale features as well as production of metallic glass foams.

**It is highly likely that continued work over the next 20-50 years will result in significant advances in all these areas, and that metallic glasses and metallic glass matrix composites will see increasing acceptance as structural materials. Whether or not they achieve widespread use in aerospace applications, however, depends critically on the development of new, lightweight alloys.**

## Metallic Glasses

### STRUCTURE

The atomic-scale structure of most metals and alloys is crystalline; that is, the atoms are arranged in a highly ordered manner on a lattice that is periodic in three dimensions, as depicted in Figure 1(a). In contrast to this crystalline structure, metallic glasses lack the long-range order of a lattice and are therefore said to be amorphous, as depicted in Figure 1(b). Although the word "amorphous" implies a complete lack of structural order, in fact the atomic structure of metallic glasses is not truly random. Constraints on atomic packing provide strong short-range order; for instance, on average the atoms have a particular number of nearest atomic neighbors at a well-defined distance. But this short-range order persists only over distances of a few atoms; there is no long-range order as there is in a crystalline alloy. In many ways, the atomic-scale structure of metallic glasses more closely resembles the highly disordered structure of a liquid than the structure of a crystalline alloy.

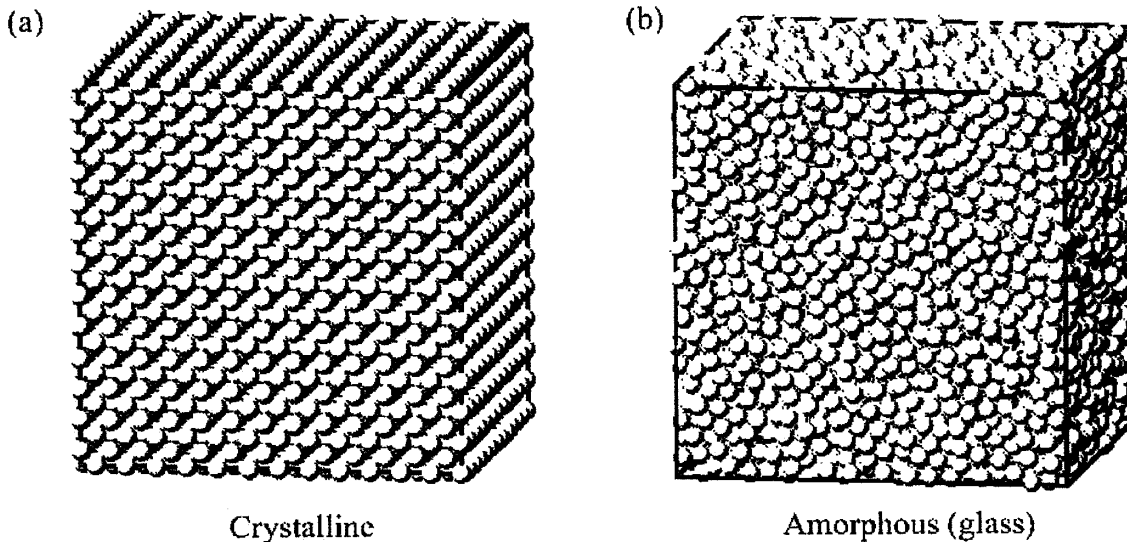


**Figure 1. Amorphous Versus Crystalline Structure.** Schematic atomic-scale structure of crystalline (a) and amorphous (b) metals. In a crystalline structure, order persists over long distances (many atomic dimensions). In a glass, there is short range order but no long-range order.

A corollary of this difference in structure is that the nature of structural defects is quite different between crystalline and amorphous alloys. Crystalline alloys, for example, have extended linear defects in the crystal structure, called dislocations, that are (in large part) responsible for determining mechanical behavior. The lack of crystalline order precludes the existence of dislocations in metallic glasses, but other sorts of defects can be present and may influence properties and behavior.

From an applications point of view, the amorphous structure of metallic glasses has two principal implications. First, the mechanical properties of amorphous alloys are significantly different from those of their crystalline counterparts; some of these differences are advantageous, but others are not. Second, because metallic glasses are

glasses in the true sense of the word, rather than melting abruptly (as crystalline metals do), they soften and flow over a range of temperatures in a manner akin to common (oxide) glasses. This creates opportunities for tremendous flexibility in the processing of metallic glasses.

## PROCESSING

### Glass-Forming Alloys

The key to making a metallic glass is to retain the disordered, liquid-like atomic scale structure during cooling from the melt. All materials have a tendency to crystallize upon cooling because the crystalline state is the most stable structure at any temperature below the melting point. But crystallization takes time, so if the cooling is fast enough, it is possible to bypass crystallization and form an amorphous structure at the glass transition temperature (Figure 2(a)). Glass formation and crystallization are therefore competitive processes; which one will occur depends on the material and the processing conditions.

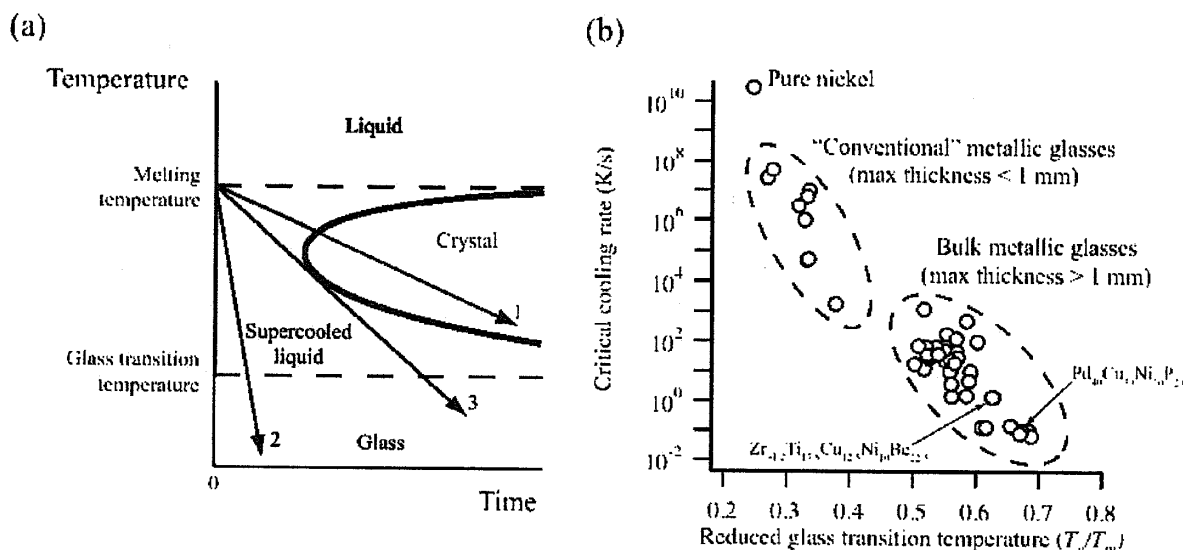


**Figure 2. Critical Cooling Rate.** (a) Effect of the cooling rate on glass formation – If the cooling rate is slow (path 1), then the melt crystallizes before going through the glass transition. If the cooling rate is fast enough (path 2), then the melt can form a glass. The critical cooling rate (path 3) is the slowest rate at which the melt can be cooled and still form a glass. (b) Critical cooling rates for various metallic alloys – The horizontal axis is the glass transition temperature normalized to the melting (liquidus) temperature.<sup>1</sup>

For some materials, such as silica (silicon dioxide) and most thermoplastic polymers, the crystallization process is slow because the crystal structures are complex and the basic structural units (for example, segments of polymer chains) are slow to rearrange into a crystalline form. These materials can therefore be produced in glassy form even at very low cooling rates; in fact, it can be difficult to crystallize them at all. Metals and alloys are another matter because the crystal structures are relatively simple and the basic structural units are individual atoms, which are highly mobile. Metallic crystals nucleate and grow quickly, making production of a metallic glass more challenging.

One way to quantify the ability of a metallic alloy to be produced in glassy form is through the critical cooling rate—the slowest rate at which a metallic liquid may be cooled and still produce a fully amorphous structure, as shown in Figure 2(a). The critical cooling rate for a variety of metallic glass-forming alloys is shown in Figure 2(b). Early metallic glasses (discovered in the 1960s and 1970s) were binary alloys with critical cooling rates typically on the order of  $10^4$  to  $10^7$  K/s. Achieving such high cooling rates requires specialized techniques (such as melt spinning) and limits the maximum thickness of the metallic glass to  $< 100 \mu\text{m}$  because of the need to rapidly extract heat from the melt. As a result, these early metallic glasses could be produced in only a limited range of forms, including ribbons, foils, wires, and powders.

Extensive research efforts in alloy design over the past two decades have resulted in the development of multi-component alloys with much lower critical cooling rates (0.1 K/s or even lower). This has enabled the production of metallic glass specimens in larger sizes—in some cases exceeding 1-cm section thickness. Common practice in the field is to refer to any alloy capable of being cast into a section at least 1-mm thick as a “bulk” metallic glass. These alloys may be cast or molded into forms suitable for structural applications.

At present, it is not possible to predict a priori the glass-forming ability of an alloy of arbitrary composition. A variety of empirical rules for selecting alloying elements and compositions have been proposed, and techniques have been demonstrated for efficient searching of composition space. But identification of alloys with good glass-forming ability is still mostly a matter of trial and error. As a result, the number of truly outstanding glass-forming alloys (loosely defined as being able to be cast as a glass to a thickness of at least 1 cm) is quite limited (see Table 1).

**Table 1. Selected Bulk Glass-Forming Alloys.** Selected alloys reported to have excellent glass forming ability, quantified here as the maximum thickness of a fully amorphous casting.<sup>2 3 4 5 6 7 8</sup>

Composition	Maximum Thickness (mm)	Reference
Mg <sub>65</sub> Cu <sub>15</sub> Ag <sub>5</sub> Pd <sub>5</sub> Gd <sub>10</sub>	10	2
Zr <sub>41.2</sub> Ti <sub>13.8</sub> Cu <sub>12.5</sub> Ni <sub>10</sub> Be <sub>22.5</sub>	50	3
Pd <sub>40</sub> Cu <sub>30</sub> Ni <sub>10</sub> P <sub>20</sub>	72	4
Cu <sub>47</sub> Zr <sub>45</sub> Ag <sub>4</sub> Al <sub>4</sub>	10	5
Pt <sub>57.5</sub> Cu <sub>14.7</sub> Ni <sub>5.3</sub> P <sub>22.5</sub>	16	6
Ti <sub>40</sub> Zr <sub>25</sub> Ni <sub>3</sub> Cu <sub>12</sub> Be <sub>20</sub>	14	7
Fe <sub>48</sub> Cr <sub>15</sub> Mo <sub>14</sub> Er <sub>2</sub> C <sub>15</sub> B <sub>6</sub>	12	8

Moving from the laboratory to industrial practice, it is important to note that factors besides alloy composition can affect glass-forming ability. In particular, some alloys are sensitive to the presence of impurities; for example, the glass-forming ability of some zirconium-containing alloys is dramatically reduced by the presence of oxygen. Processing conditions also influence the ability to make a glass; these may include the material and surface finish of the mold and the temperature of the liquid prior to casting. Finally, glass-forming ability can be quite sensitive to small variations in composition, which may be difficult to control in industrial practice.

## Casting and Molding

Like other alloys, metallic glasses can be cast into net-shape or near-net-shape geometries. Die casting into a permanent (metal) mold—because it provides the rapid heat transfer needed to meet the requirement for relatively rapid cooling—is the most common casting technique. In most cases, casting is done in either a vacuum or an inert atmosphere to prevent formation of oxide particles that promote crystallization.

Conventional casting, however, does not take advantage of the flexibility afforded by the glassy nature of these alloys. If a metallic glass is heated to a temperature above its glass transition temperature, it becomes a supercooled liquid. In this state, the viscosity drops with increasing temperature over a wide range, making it possible to control the viscosity by controlling the temperature.<sup>1</sup> This ability to control the viscosity enables many of the processing techniques commonly used in molding thermoplastic polymers to be applied to metallic glasses (Figure 3).

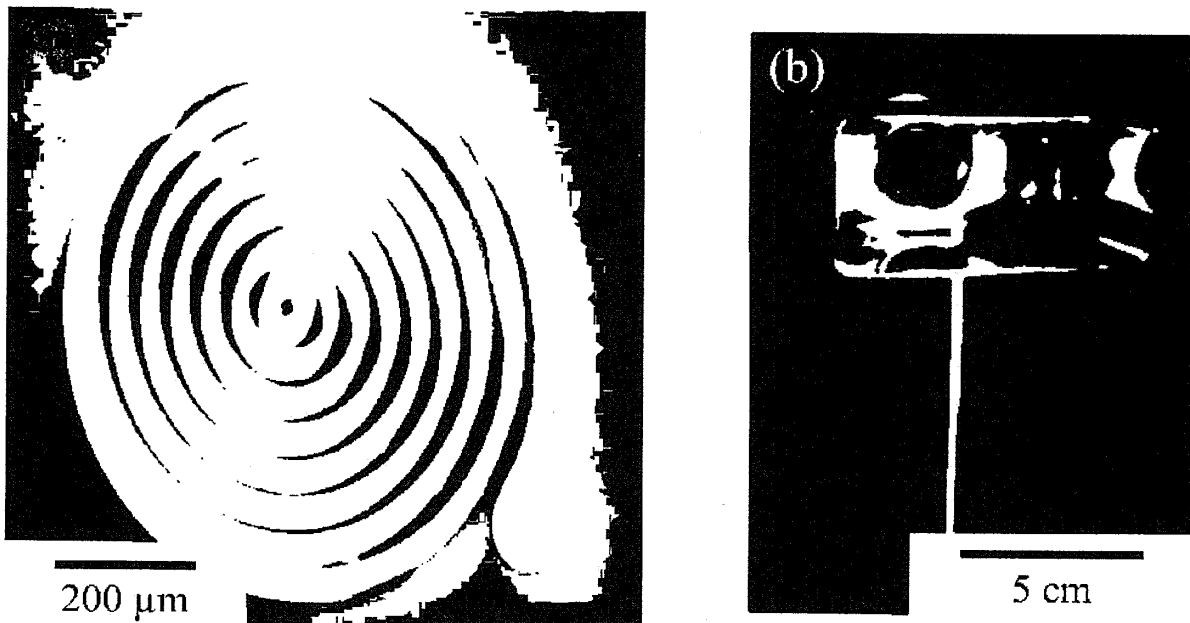


**Figure 3. Examples of Processing of Metallic Glasses.** (a) Microspring produced by lithography and (b) thin-walled bottle produced by blow molding. Images are courtesy of Professor Jan Schroers (Yale University).

There are two important limitations on processing of metallic glasses in the supercooled liquid region. First, supercooled liquids are metastable and have a tendency to crystallize, so there is a limited window of time (typically on the order of minutes) in which the processing must be completed if the glassy structure is to be maintained. Second, the viscosity of many glass-forming alloys near the glass transition temperature is too high for convenient processing. The viscosity can be reduced by increasing the processing temperature, but higher temperatures promote crystallization

<sup>1</sup> A crystalline metal, in contrast, melts abruptly, going from a rigid solid to a low-viscosity fluid very quickly.



and thus reduce the window of time available for molding. In practice, therefore, successful molding requires careful control of the processing conditions.

### **Joining**

Structural applications inevitably require joining of components, for instance by mechanical fasteners or adhesives or by welding, soldering, or brazing. The use of fasteners and adhesives is much the same for metallic glasses as for any other metal. Techniques such as welding, soldering, and brazing are potentially problematic because they involve heating the glassy alloy, running the risk of crystallization (which could make the joint more brittle). In welding, for instance, the metal to be joined is actually melted and then resolidifies upon cooling. In the case of a metallic glass, care must be taken to ensure the cooling rate is fast enough to avoid crystallization. There is also a risk that the glassy material in the heat-affected zone (near to but not in the molten region) might crystallize. Laboratory tests of a variety of welding techniques have been performed on several glass-forming alloys with mixed results, and it is clear that much remains to be done in this area.

### **Foams**

One particularly promising recent development is the ability to produce metallic glass foams. Here, the relatively high viscosity of glass-forming alloys is an advantage in producing a stable foam structure that can be solidified, leaving a high-porosity foam with metallic glass ligaments.<sup>9</sup> These foams have high specific strength (that is, strength normalized to density) and specific stiffness and could have excellent damage tolerance, although this has not been demonstrated.

### **Thin Films and Coatings**

The discussion above focuses on the processing of free-standing metallic glasses, with an emphasis on structural applications. However, it is also possible to produce amorphous alloys as thin films or coatings using techniques such as physical vapor deposition or electrodeposition. Although the thicknesses of material that can be produced in this way are limited, they are useful for making amorphous alloy coatings (for wear and corrosion resistance) or for thin films for magnetic or micro-electromechanical system (MEMS) applications. A distinct advantage of the thin film techniques is that because the effective cooling rates during vapor deposition are extremely high, a much wider range of alloys can be produced in amorphous form than is possible with casting. This allows the alloy composition to be tailored for optimization of functional properties, with less concern about glass-forming ability.

### **Mechanical Behavior Near Room Temperature**

When a material is subjected to a stress, it can experience both elastic and plastic deformations. Elastic deformation occurs at lower stresses and is recoverable when the applied stress is removed. The limit of elastic deformation is defined by the yield stress—the point at which plastic (nonrecoverable) deformation begins. Much of the current interest in metallic glasses arises because their yield stresses (that is, their strengths) can be much higher than those of crystalline alloys of similar composition; this difference is a direct result of the novel atomic-scale structure of metallic glasses. The fracture and fatigue characteristics of metallic glasses are also different from those

of conventional alloys. In this section, we review the mechanical behavior of metallic glasses, with particular attention to properties of interest for aerospace applications. We consider actual properties in detail in the section below on applications, where we compare the properties of metallic glasses with those of other advanced structural materials.

### **Stiffness: Elastic Deformation**

Stiffness is the resistance of a material to elastic deformation and is quantified by either the elastic modulus (for tensile or compressive loads) or the shear modulus (for shear loading). Metallic glasses tend to be somewhat (20-30 percent) less stiff than crystalline alloys of similar composition. The lower modulus is a consequence of the amorphous structure, in which atoms are (on average) slightly farther apart than in a crystalline alloy, enabling certain atomic relaxations that are not possible in a crystal. The lower modulus of amorphous alloys is clearly a concern in applications where stiffness is a primary criterion, but it does present some advantages. For instance, some applications (springs, for example) require the ability to store elastic strain energy (resilience), and here metallic glasses do quite well. Resilience is also a key figure of merit for snap-fit assembly of materials without fasteners. Overall, however, for structural applications, the low stiffness of metallic glasses is a disadvantage.

### **Strength and Ductility: Plastic Deformation**

The theoretical strength of perfect, defect-free crystalline metals is several orders of magnitude larger than strengths measured in typical laboratory experiments. The difference exists because metallic crystals inevitably have crystalline defects (dislocations) that are able to move at relatively low stresses and cause plastic (nonrecoverable) deformation. Because dislocations cannot exist in an amorphous structure, in principle the strength of amorphous alloys should approach theoretical limits based on the inherent strength of the atomic bonds. As shown in Table 2, the strength of aluminum-based metallic glasses can be two or three times greater than those of conventional (crystalline) high-strength aluminum alloys. Similarly high strengths are seen for other amorphous alloys; for instance, the best iron-based alloys have a strength of approximately 4 GPa—again, two or three times greater than those of conventional high-strength steels.<sup>10</sup> Such high strengths create great interest in potential structural applications of metallic glasses.

**Table 2. Comparison of Strengths of Amorphous and Crystalline Aluminum Alloys.** Compared with the theoretical maximum strength (taken to be  $\mu/30$ , where  $\mu$  is the shear modulus of pure aluminum).

	Yield Stress (MPa)	% of Theoretical Strength
Theoretical Strength (Defect-Free Crystal)	1,600	-
Typical High-Strength Aluminum Alloy (7xxx Series) <sup>11</sup>	400-500	25-31%
Best Crystalline Aluminum Alloy <sup>12</sup>	770	48%
Aluminum-Based Metallic Glass <sup>13</sup>	1,280	80%

Unfortunately, the lack of dislocations in amorphous alloys is also their Achilles' heel. In crystalline alloys, dislocations move and multiply in response to applied stresses, resulting in dislocation tangles that increase the resistance to further dislocation motion. This process, called strain hardening, is of crucial importance because it makes plastic deformation stable. If one region of a crystalline material yields and begins to plastically deform, the deforming region strain hardens, and so another region will deform instead. The result is that the plastic deformation is not concentrated but rather spreads through a large volume of material. Metallic glasses, lacking dislocations, do not strain harden and in fact strain soften in response to plastic deformation. This means that as soon as any one region yields, any further deformation will occur in the same region. This process, known as shear localization, leads to the formation of shear bands (Figure 4). In any loading geometry where the metallic glass experiences significant tensile loading, fracture occurs on a single dominant shear band with essentially zero tensile ductility.<sup>2</sup> Metallic glasses therefore fracture in an abrupt, apparently brittle manner on the macroscopic scale (even though there can be significant plasticity on a microscopic scale). This lack of ductility is of obvious concern to designers interested in structural applications. Furthermore, it limits the ability to fabricate metallic glasses into different shapes by deformation processing (by rolling or forging, for instance) after casting.

<sup>2</sup> This assumes there is no geometrical constraint preventing fracture. Some geometries (such as simple bending) can involve tensile loading, but there can still be significant plastic deformation because the geometrical constraints inhibit propagating of shear bands across the specimen.

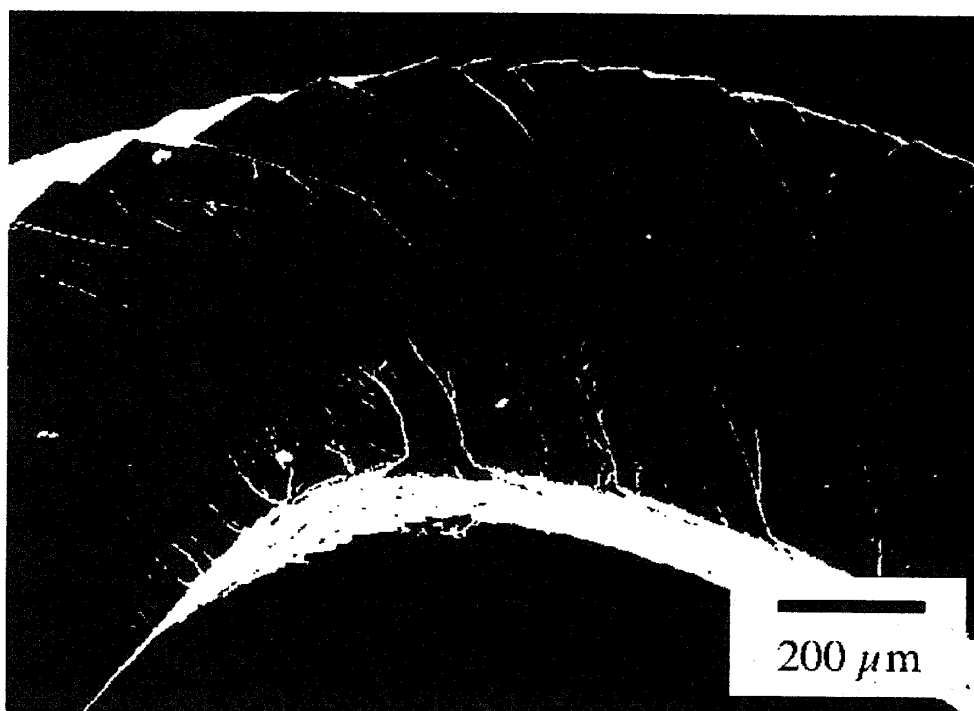


Figure 4. Shear Bands. Produced by bending of a zirconium-based metallic glass.<sup>14</sup>

## Fracture Toughness

Fracture toughness is a measure of a material's resistance to growth of cracks, a critical property for structural materials subjected to tensile loading. In very tough metals, the toughness usually results from plastic deformation that occurs near the tip of the advancing crack; plastic deformation requires energy, and the need to provide this energy translates into resistance to crack growth.<sup>3</sup> Despite their lack of tensile ductility, at least some metallic glasses are not brittle in the same sense that ceramics are, for example, because they can experience significant plastic deformation around the crack tip during fracture. For instance, the fracture toughness ( $K_{Ic}$ ) of zirconium-based metallic glasses is about  $20 \text{ MPa}\cdot\text{m}^{1/2}$ <sup>15</sup>—somewhat lower than the  $\sim 55 \text{ MPa}\cdot\text{m}^{1/2}$  typical of crystalline zirconium alloys<sup>16</sup> but much greater than the fracture toughness of ceramics (typically  $1\text{-}5 \text{ MPa}\cdot\text{m}^{1/2}$ ). The fact that metallic glasses are reasonably tough despite their lack of tensile ductility suggests structural applications are not out of the question.

However, some metallic glasses appear to be intrinsically brittle in that they fracture with only limited plastic deformation near the crack top and thus have very low values of fracture toughness. For this reason, some alloys that would otherwise be highly desirable, such as iron-based metallic glasses (for their high strength and low cost) and magnesium-based glasses (for their low density), fall into this category. The physical origins of the difference between intrinsically brittle metallic glasses and those capable of limited plastic deformation (and thus some toughness) are not well understood.

<sup>3</sup> In other materials, notably polymer-matrix composites, other mechanisms of toughening can be more important.

Even some metallic glasses with reasonable toughness may be embrittled by exposure to elevated temperatures. This may occur in the heat-affected zone during welding (as discussed above), or it may be a by-product of processing in the supercooled liquid region (as in injection molding, for instance). The causes of embrittlement are also not well understood, and there is no known way to reverse embrittlement once it occurs.

## **Fatigue**

Fatigue is a process by which materials can experience incremental crack growth owing to cyclic loading, even at stresses well below the yield stress. If unabated, fatigue cracks can grow to a critical length at which abrupt catastrophic fracture occurs. Up to 90 percent of failures of structural components in service are estimated to be caused by fatigue, making fatigue resistance of obvious importance to designers.

The fatigue resistance of metallic glasses is not very good. A common measure of fatigue resistance is the fatigue limit—the stress amplitude (range) below which no fatigue failure will occur, regardless of the number of loading cycles the material experiences. The fatigue limit for high-strength crystalline alloys is typically about 40 percent of the tensile strength, but for metallic glasses, it is only about 5 percent of the tensile strength (Figure 5). The reason for this difference has to do with the structure of the material. In a crystalline alloy, there are microstructural features (such as grain boundaries and precipitate particles) that can inhibit the growth of fatigue cracks. In metallic glasses, the microstructure is completely featureless, and there is nothing to prevent fatigue cracks from growing once they have been initiated.

The poor fatigue resistance of metallic glasses is a critical limitation for structural applications in aerospace because it implies a need to overdesign components to keep the stresses far below the yield stress. Thus, much of the advantage of having a high-strength material in the first place is lost. The desire to improve metallic glasses' fatigue performance has led to the development of metallic-glass-matrix composites with outstanding properties, as discussed below.

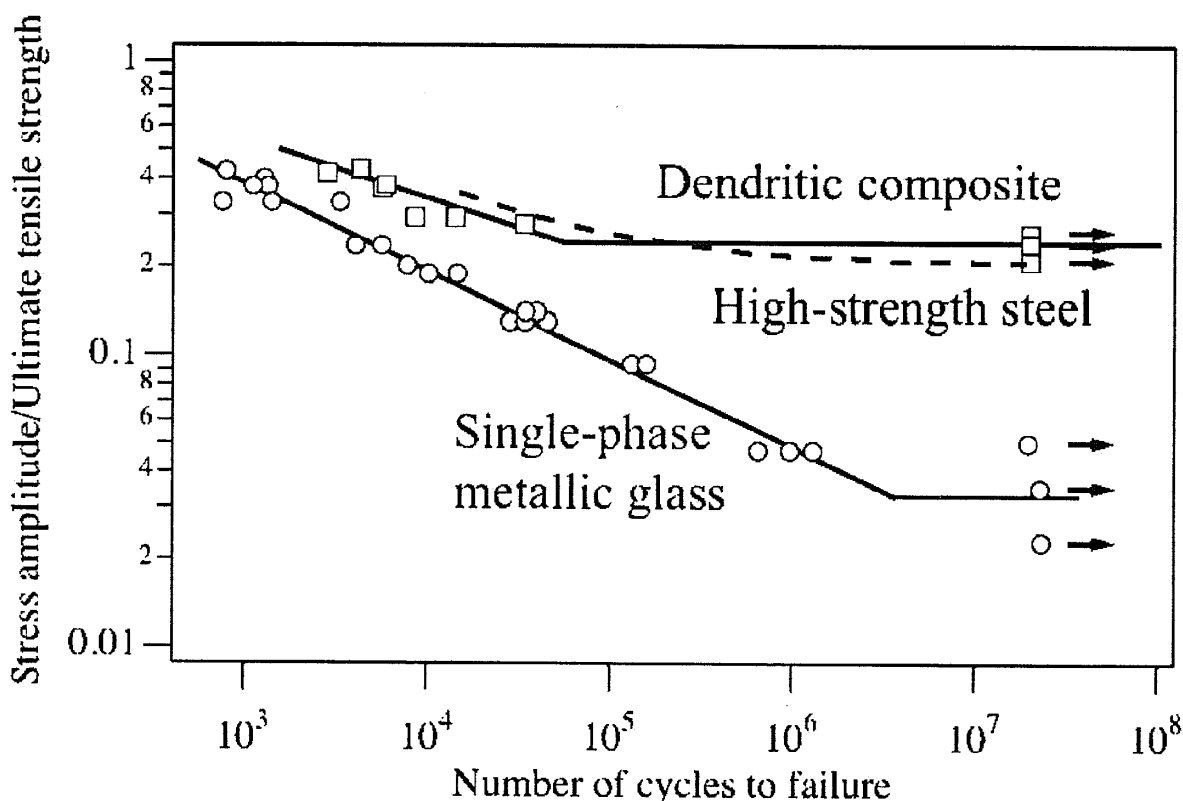


**Figure 5. Fatigue Limit of Metallic Glasses and Metallic-Glass-Matrix Composites.** Fatigue life data for single-phase zirconium-based metallic glass (red) and a dendritic metallic glass matrix composite (blue). Representative data for steel (300-M) of similar tensile strength are shown for comparison.<sup>17 18 19</sup>

## Wear Resistance

Because of their high yield strength, metallic glasses also have very high hardness. This, in turn, implies they might have good tribological behavior, which would be of particular interest when combined with the good corrosion resistance of some alloys (see below), opening up potential applications such as coatings on dry bearings for space applications.<sup>20</sup> However, the tendency of metallic glasses to form shear bands and (in some cases) partially crystallize owing to deformation means their wear resistance is perhaps not as good as their high hardness would suggest. Nevertheless, the wear resistance of metallic glasses can still be quite good, and in fact one of the principal current markets for amorphous alloys is as wear- and corrosion-resistant coatings for tools such as drill bits.

## Corrosion and Stress-Corrosion Cracking

It is frequently stated that metallic glasses have excellent corrosion resistance, but this is not always true. The lack of grain boundaries and second-phase particles makes some metallic glasses extremely resistant to corrosion, but this is not true of all alloys (some of which oxidize rapidly in air). Broadly speaking, the corrosion resistance of nickel- and iron-based metallic glasses is better than that of alloys based on zirconium, titanium, and copper (particularly in environments containing chloride ions).<sup>21</sup> Some alloys are susceptible to localized pitting corrosion, probably facilitated by the presence of crystalline inclusions.

The subject of stress-corrosion cracking of metallic glasses, despite its obvious importance for structural applications, has received scant attention in the literature. What little work that has been done has focused on zirconium-based glasses, with the observation that these alloys are very susceptible to stress-corrosion cracking in aqueous environments containing chloride ions, likely owing to the fact that they do not form protective oxide surface layers.<sup>22</sup>

### Mechanical Behavior at Elevated Temperature

The discussion above relates to mechanical behavior at temperatures well below the glass transition temperature. At elevated temperatures, the strength drops and plastic deformation transitions to a homogeneous mode, occurring throughout the specimen instead of being localized into shear bands (Figure 6). Above the glass transition temperature, the alloy becomes a fluid, with a viscosity that drops exponentially with increasing temperature. Because the strength of the material is low, temperatures either above or below the glass transition may be useful for processing, as discussed above. However, the decrease in strength and the tendency for crystallization at elevated temperatures preclude use of metallic glasses from structural applications at temperatures approaching the glass transition temperature.

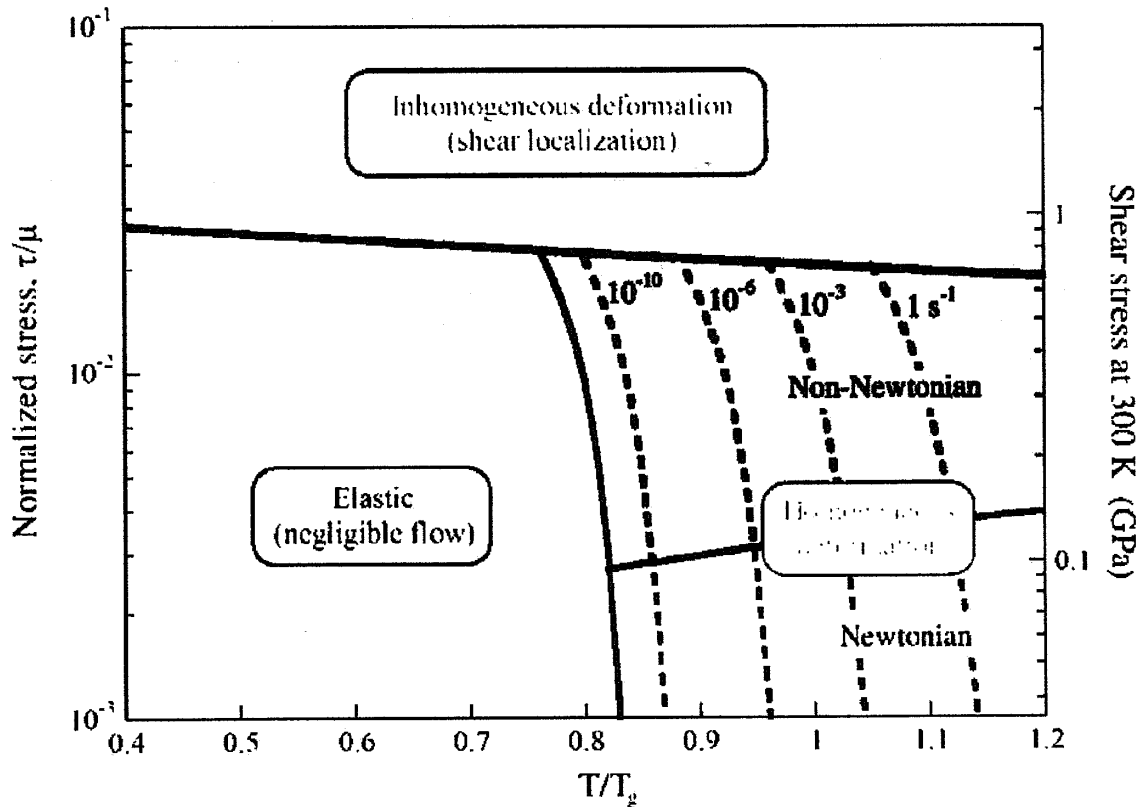


**Figure 6. Deformation Map for Metallic Glasses.** As a function of temperature (normalized to the glass transition temperature) and applied shear stress  $\tau$  (normalized to the shear modulus,  $\mu$ ). At high stresses, plastic deformation occurs inhomogeneously, being localized into shear bands. At high temperatures, plastic deformation becomes homogeneous. The dashed lines represent different strain rates. The absolute stresses given are representative of the well-studied bulk metallic glass Zr<sub>41.2</sub>Ti<sub>13.8</sub>Cu<sub>12.5</sub>Ni<sub>10</sub>Be<sub>22.5</sub>, but the general features of the map are expected to apply to all metallic glasses.<sup>23</sup>

### **Other Properties: Magnetic, Electrical, Optical, Thermal, and Acoustic**

Although most of the current interest in metallic glasses centers on their mechanical properties, it is appropriate to consider other properties of potential utility. Of these, the magnetic properties of ferromagnetic metallic glasses stand out.<sup>24</sup> A variety of ferromagnetic glass-forming alloys exist, mostly based on transition metals (iron, nickel, and cobalt). The presence of alloying elements (necessary to make the material glass-forming) means the saturation magnetization of metallic glasses is not as large as that of the pure elements. However, some amorphous alloys have very low coercivity (a measure of how strong a magnetic field must be to change the direction of magnetization of the material) owing to the lack of crystalline defects (such as grain boundaries) and magnetocrystalline anisotropy. In addition, the relatively high electrical resistivity of amorphous alloys (see below) minimizes eddy current losses caused by high-frequency magnetization/demagnetization. Some amorphous alloys also have strong magnetoelastic effects (coupling between magnetic properties such as susceptibility or magnetization and elastic strain). Current and potential future applications of these magnetic properties are discussed below.

Like crystalline alloys, metallic glasses have conduction electrons that make them both electrically and thermally conductive,<sup>25</sup> although their structural disorder and high alloy content make them poor conductors. In addition, in a behavior that is useful in some applications, the conductivity of metallic glasses is not very sensitive to temperature; an exception is near absolute zero, where some amorphous alloys become superconducting.

Another consequence of the amorphous structure of metallic glasses is that they tend to have very low acoustic damping. This may be useful in applications such as vibrating-structure gyroscopes for vehicle orientation.<sup>26</sup>

A common misperception among those hearing about metallic glasses for the first time is to think they are transparent. This is not the case; amorphous alloys are highly reflective, with a shiny luster similar to that of other metals (Figure 7). This is a result of the presence of the conduction electrons, which scatter and absorb incident light.



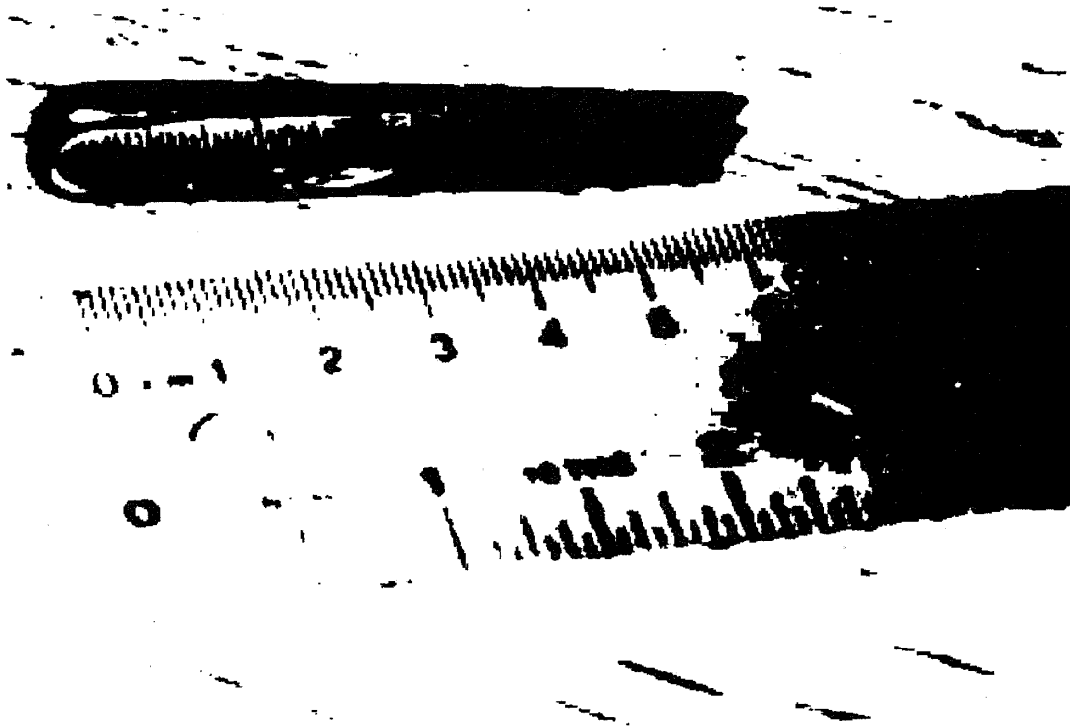


**Figure 7. Cast Metallic Glass Wedge.** Wedge of a zirconium-based bulk metallic glass produced by casting. Note the shiny metallic luster, typical of metallic glasses.<sup>27</sup>

## **Metallic Glass Matrix Composites**

As discussed above, the lack of crystalline defects gives metallic glasses high strength but compromises their ductility and fracture toughness. In particular, the tendency for plastic deformation to localize into shear bands prevents the material from deforming in a "graceful" manner. So it should not be surprising that there have been many attempts to control shear band initiation and propagation by making composite materials consisting of particles or fibers of some other material (most commonly a ductile crystalline metal) in a metallic glass matrix. The idea is to produce a material with improved ductility, fracture toughness, and fatigue properties while (hopefully) not sacrificing the qualities—especially strength and processing flexibility—that make metallic glasses interesting in the first place.

### **PROCESSING AND STRUCTURE OF COMPOSITES**

Broadly speaking, there are two kinds of metallic glass matrix composites: ex situ and in situ. In ex situ composites, the metallic glass and the crystalline phase (be it in the form of particles or fibers) are physically combined, for instance by adding particles to the melt before casting. In situ composites are different in that the crystalline phase is produced directly from the melt (by precipitation) during processing. This fundamental difference in processing leads to significant differences in structure and therefore in properties.

## **EX SITU COMPOSITES**

There are two basic ways of making ex situ composites, in which the metallic glass matrix and the crystalline phase are combined physically, without a chemical reaction:

- Add crystalline particles to a melt of a glass-forming alloy and then cast under conditions that allow the matrix to form a metallic glass.
- Make a preform of a crystalline phase (by packing fibers into a mold, for instance) and then cast the glass-forming alloy around the preform.

Both approaches have limitations. In the first, the addition of particles to the melt increases the viscosity (which is already quite high relative to non-glass-forming alloys) considerably, ultimately to a point where casting becomes impossible. This limits the volume fraction of particles that can be added, which in turn limits the control one has over the microstructure and, in particular, the spacing of the particles. With a preform, the volume fraction of the crystalline phase can be much higher (up to about 80 percent by volume), but the problem then is how to infiltrate the high-viscosity melt into the preform without leaving voids and while still ensuring sufficiently rapid cooling to form a glassy matrix. With both approaches, interfacial reactions between the crystalline phase and the melt can cause partial or complete crystallization of the matrix, degrading the mechanical properties.

## **IN SITU COMPOSITES**

The difficulty of making satisfactory ex situ composites has led to the development of a new approach in which the crystalline phase is precipitated directly from the melt, either during casting<sup>28</sup> or in a separate step prior to casting.<sup>29 30</sup> Precipitation during casting, although easier, is problematic from a practical standpoint because variations in the cooling rate (from the surface to the center of a casting, for instance) lead to significant variations in structure and, hence, in properties.

One of the most promising recent advances in the metallic glass field is the development of in situ composites in which the crystalline phase is precipitated as dendrites, either during casting (Figure 8) or by holding the alloy at an elevated temperature prior to casting.<sup>31</sup> By suitably choosing alloy composition, holding time, and temperature, the volume fraction, size, and spacing of the dendritic phase can be controlled. This control provides great flexibility in determining the mechanical properties of the resulting material. Because the crystalline phase is produced prior to casting, variation in the cooling rate across the casting is much less important, though the cooling rate must still be sufficiently high to ensure the matrix forms a glass during cooling. Once the glassy matrix is formed, the composite can be reheated above the glass transition temperature, allowing for thermoplastic forming in a manner similar to single-phase metallic glasses (as described above). Finally, the presence of the dendritic second phase allows for deformation processes (for example, by cold rolling or forging), similar to crystalline alloys.<sup>32</sup>

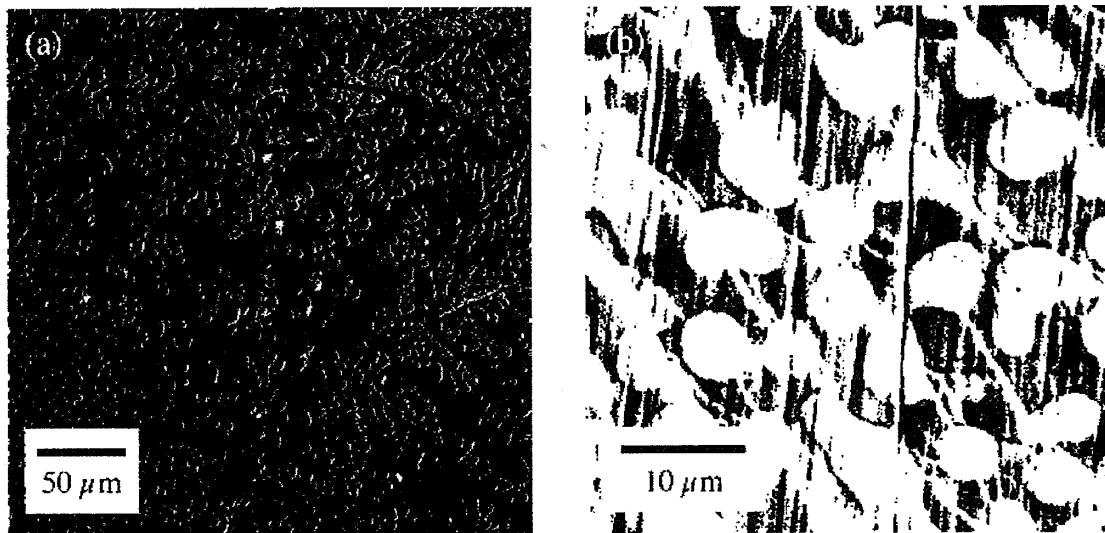


**Figure 8. Microstructure of In Situ Metallic Glass Matrix Composite.** With ductile crystalline dendrites.  
 (a) Scanning electron micrograph showing the dendrites (light gray) in the glassy matrix (dark gray).  
 (b) Composite after plastic deformation; note the multiplicity of slip steps, indicating extensive interaction of shear bands with the dendrites.<sup>33</sup>

The key limitation of these in situ composites is that not every alloy system is capable of forming them. While any alloy will form crystalline phases at elevated temperatures, usually the crystalline phases that form are brittle intermetallics that degrade rather than enhance the mechanical properties. To be effective in controlling shear bands, the precipitated phase needs to be ductile, have a shear modulus lower than that of the glassy matrix, and (preferably) form as dendrites. To date, the only published reports of systems that satisfy these criteria concern alloys based on early transition metals, notably zirconium and titanium. Whether in situ composites can be developed in other alloy systems remains to be seen.

## MECHANICAL PROPERTIES OF COMPOSITES

The ability to produce mixed amorphous-crystalline microstructure provides the ability to control the formation and propagation of shear bands. The resulting materials can have good fracture and fatigue resistance while retaining the high strength and processing flexibility associated with metallic glasses.

The origin of these effects is related to the development of a region of plastic deformation at the tip of an advancing crack. For a crack opening under tensile loading, the size of the plastic region is approximately given by:

$$R_p \approx \frac{1}{2\pi} \left( \frac{K_{Ic}}{\sigma_y} \right)^2, \quad (\text{Equation 1})$$

where  $K_{Ic}$  is the plane-strain fracture toughness (mentioned above) and  $\sigma_y$  is the yield strength. The size of the plastic zone varies from  $\sim 1 \mu\text{m}$  for "intrinsically brittle" metallic glasses to  $\sim 1 \text{mm}$  for glasses capable of some plastic deformation.<sup>34</sup> If the material has structure on this length scale (or if the sample itself is of this size), then

deformation can proceed in a stable manner by generation and subsequent arrest of shear bands. The key to composite design is to produce a microstructure with the correct length scale to prevent propagating shear bands from becoming catastrophic cracks. This turns out to be relatively difficult with ex situ composites, for reasons of processing described above. As a result, the recently developed dendritic in situ composites have the most promising properties, and we focus the remainder of our discussion on them.

## **STRENGTH AND DUCTILITY: PLASTIC DEFORMATION**

As with other composite materials, the yield strength of metallic glass matrix composites can be approximated as a simple rule of mixtures based on the volume fraction of the two phases. Because the ductile crystalline phases useful for limiting shear band propagation are weaker than the amorphous matrix, in producing a composite, some sacrifice in strength is inevitable. However, the gains in tensile ductility can be significant. For instance, monolithic titanium-based metallic glasses (like all metallic glasses) have essentially zero tensile ductility, but in situ composites based on titanium have been reported with tensile elongation as large as 12 percent.<sup>35</sup> This is comparable to the ductility of Ti-6Al-4V (the most common conventional titanium alloy), but in a material with about 30 percent greater strength. The properties of metallic glass matrix composites and more conventional materials are further compared below.

## **FRACTURE AND FATIGUE**

The development of a stable plastic zone means additional energy is required for crack propagation, making in situ composites much more resistant to fracture and fatigue than are single-phase glasses. For instance, the plane-strain fracture toughness of some zirconium-based in situ composites can exceed  $170 \text{ MPa m}^{1/2}$ —7 times greater than that of single-phase glasses and greater than that of virtually any other metallic alloy.<sup>36</sup> This resistance to crack propagation is also manifested as improved fatigue performance. The fatigue strength of the zirconium-based in situ composites is 20-30 percent of the tensile strength; in comparison, monolithic metallic glasses have a fatigue strength of only  $\sim 5$  percent of the tensile strength.<sup>37</sup> The fatigue strength of the in situ composites is thus comparable to that of conventional structural alloys.

## **Aerospace Applications of Metallic Glasses**

### **STRUCTURAL APPLICATIONS**

The key properties of materials for structural applications in aerospace are:

- Strength.
- Stiffness (Young's modulus).
- Density (weight).
- Fracture toughness (damage tolerance).

- Fatigue resistance (including resistance to both fatigue crack initiation and fatigue crack growth).
- Corrosion resistance (including stress-corrosion cracking).
- Cost (including raw materials, shaping, and assembly).

Figure 9 illustrates the mechanical properties of metallic glasses and metallic glass matrix composites compared with other structural materials. Since weight is a particular concern in aerospace applications, in Figure 9(a) we normalize both yield strength ( $\sigma_y$ ) and stiffness ( $E$ ) to density ( $\rho$ ); two materials with the same specific strength ( $\sigma_y/\rho$ ) or specific stiffness ( $E/\rho$ ) could be used to produce a component with the same overall strength or stiffness, respectively, at the same weight. Materials in the upper-right corner of the plot have the best combination of strength and stiffness for a given weight. Notice that the metallic glasses (and dendritic composites) can be stronger than virtually all crystalline metals, although the stiffness of metallic glasses tends to be somewhat smaller than that of crystalline alloys of similar composition.

Figure 9(b) illustrates the damage tolerance of metallic glasses compared with other materials. By plotting the fracture toughness ( $K_{Ic}$ ) against modulus ( $E$ ), we can also compare the fracture energy ( $G_{Ic} \approx (K_{Ic})^2/E$ ) of the materials; the dashed diagonal lines are lines of constant fracture energy. Figure 9(b) reveals several interesting aspects of the damage tolerance of metallic glasses. First, although the fracture toughness of some metallic glasses is comparable to that of crystalline metals, some metallic glasses—most notably those based on iron (Fe) and magnesium (Mg)—are as brittle as any ceramic. Second, both the fracture toughness and the fracture energy of the dendritic metallic glass matrix composites can be superior to those of all but the most fracture-resistant metals.

These considerations suggest the dendritic metallic glass matrix composites might indeed find applications as structural materials in aircraft and/or spacecraft. The most obvious applications would be to replace steel in certain components where strength is critical but space is limited. These might include pylon structures and landing gear,<sup>38</sup> although it has yet to be demonstrated that the composites can be fabricated in the sizes necessary. Furthermore, the corrosion and stress-corrosion cracking resistance of these materials has not been fully evaluated.

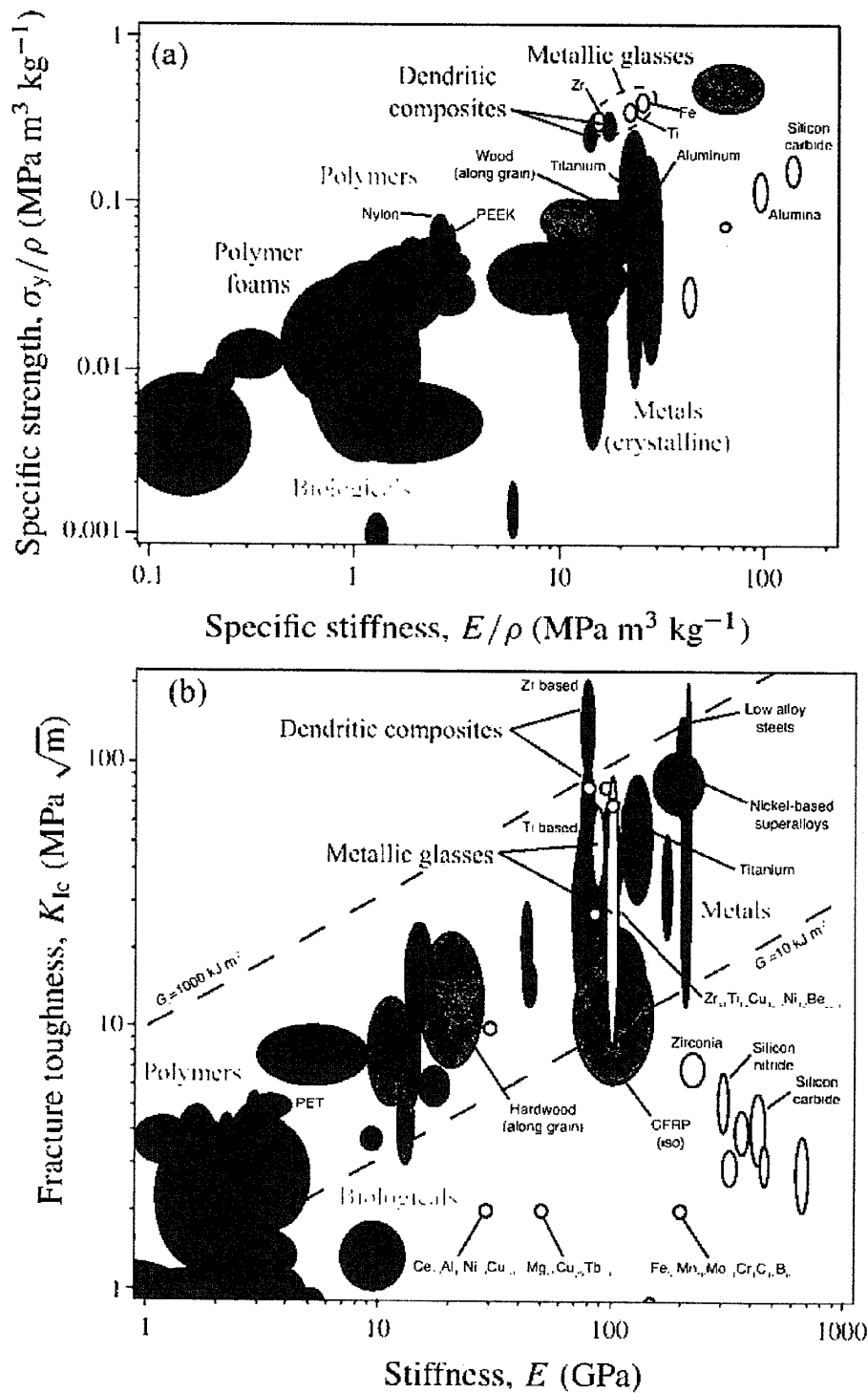


**Figure 9. Materials Property Charts.** (a) Strength and stiffness (both normalized to density) of metallic glasses (yellow) and dendritic metallic glass matrix composites (red) compared with other materials. (b) Damage tolerance. On this plot, the dashed lines represent contours of equal fracture energy. In both plots, polymer composites (CFRP and GFRP) are represented by isotropic averages; continuous fiber composites can have greater strength and stiffness in a direction parallel to the fibers.<sup>39</sup>

Metallic glass foams (see above) also provide intriguing possibilities for structural applications. It has recently been shown that metallic glass foams with outstanding strength can be formed by controlling the size of the ligaments between pores.<sup>40</sup> This is a new development, and these foams have not been fully characterized, but it seems likely that optimized foams will have a specific stiffness ( $E/\rho$ ) superior to that of polymer foams, along with high strength and acoustic damping. Such structural foams could be useful in applications requiring strength and stiffness under compressive loads, such as structural panels for extraterrestrial buildings. Conceivably, such structural foams might even be produced on site (from raw feedstock), reducing the volume of material that needs to be launched.

A final possibility is that metallic glasses might be combined with polymer composites into metal-fiber laminate materials. Similar laminates (with crystalline aluminum alloys) are being employed in large quantities on the new Airbus 380 and are likely to find increased application in the future.<sup>41</sup> The use of metallic glasses in these laminates is appealing because of their high specific strength (although the specific stiffness is lower than that of aluminum). Furthermore, the individual layers in the laminate are sufficiently thin that a wide range of glass-forming alloys might be considered (in contrast to thicker structural sections, which will be limited by the glass-forming ability of the alloy).

## **OTHER APPLICATIONS**

Monolithic metallic glasses are unique among metallic materials in having no microstructure at length scales of more than a few atomic spacings. In principle then, metallic glasses should be capable of replicating features down to this scale. This possibility is facilitated by the ability of metallic glasses to be formed in the supercooled liquid temperature range with controllable viscosity. Indeed, superplastic forming of metallic glass surfaces with features as small as 13 nanometers has been demonstrated.<sup>42</sup> This ability could be exploited for direct embossing of nanostructures in polymers or other materials. Structures on this length scale are also potentially useful as diffraction gratings for ultraviolet and soft x-ray radiation.

In a related area, metallic glasses have a variety of useful properties for application in micro-electromechanical system (MEMS) actuators, including large elastic strains and high resilience (elastic strain energy storage), good corrosion and wear resistance, and an excellent surface finish.<sup>43</sup> The scale of these devices is smaller than the plastic zone size (Equation 1 above), making brittle fracture unlikely. Furthermore, a much wider variety of amorphous alloys can be made in thin film form (by vapor deposition) than is possible by casting.

Finally, the magnetic properties of certain amorphous alloys have long been exploited. For instance, their low coercivity and high electrical resistivity make ferromagnetic amorphous alloys attractive as high-efficiency electrical transformers, particularly at high frequencies. Such applications are likely to continue well into the future.

## **Current Challenges and Prospects for the Future**

### **ALLOY DESIGN**

A critical limitation of existing metallic glass technology (and related composites) is the relative dearth of alloys with good glass-forming ability. The best glass-forming alloys are either based on expensive elements (for example, palladium) or contain toxic elements (for example, beryllium in the best zirconium- and titanium-based alloys). For aerospace applications, the most glaring lack is that, despite significant alloy design efforts in the United States (through the DARPA Structural Amorphous Metals program), Japan, China, and elsewhere, there are no good glass-forming alloys based on aluminum. Attempts to make aluminum-based metallic glass components by consolidating amorphous powders have met with limited success. Similarly, all of the good iron-based metallic glasses contain considerable amounts of nonmetallic elements (notably carbon, boron, silicon, and/or phosphorus), which are thought to contribute to the very low fracture toughness of these alloys (Figure 9(b)).

However, there is reason to expect that further progress is possible. Recent experimental results have shown that some of the empirical "rules" of glass-forming ability<sup>44</sup> are actually quite flexible, and that glass-forming ability is much more sensitive to composition than had been previously appreciated.<sup>45</sup> So it is highly probable that some excellent glass-forming alloys compositions remain to be discovered, possibly including some low-density glasses based on aluminum.

Identifying these good glass-forming alloys will be a challenge. Most alloy development to date has been done with a brute-force approach, but combinatorial techniques<sup>46</sup> are likely to enable much more rapid screening. One issue is identification of suitable metrics for glass-forming ability, since the combinatorial approaches use vapor-deposited thin films, and it is not clear what characteristics of such a film correlate with glass-forming ability in the bulk. Similarly, continued development of ab initio molecular dynamics techniques should enable identification of candidate alloys from computer simulations, particularly as computers continue to increase in power.

One area that has received insufficient attention is the influence of processing conditions on glass-forming ability. For instance, application of electromagnetic vibrations during cooling reportedly significantly enhances the glass-forming ability of magnesium-based metallic glasses.<sup>47</sup> This approach could, in principle, be applied to other alloys, possibly greatly extending the range of alloys and compositions that can be produced as bulk metallic glasses.

### **THERMOPHYSICAL PROPERTIES AND THERMOPLASTIC PROCESSING**

Most of the practical interest in single-phase (monolithic) metallic glasses centers on the potential for thermoplastic processing near to or above the glass transition temperature. However, the thermophysical properties and behavior of metallic glasses are not well understood. For instance, the viscosity of the metallic glass melt (or supercooled liquid) is of critical importance, but we do not know how and why alloy composition influences viscosity. From an engineering point of view, the practical aspects of molding of metallic glasses are just beginning to be explored. Certainly many



parallels can be drawn with thermoplastic forming of polymers, but there are certain to be many differences as well.

Continued developments in this area are highly likely to result in the ability to produce complex net-shape parts in a single processing step. This ease of processing could offset the higher raw materials costs for metallic glasses, making them competitive in a much wider range of applications. Furthermore, as noted above, the ability to replicate extremely small features (< 20 nanometers) in metallic glasses is likely to be exploited in the manufacture of nanostructured devices.<sup>48 49</sup>

Finally, development of metallic glass foams will continue and will be aided by improved understanding of thermophysical properties. It is highly likely that foams will be produced in a wide range of glass-forming alloys, and that techniques will be developed for precise control of the porosity, pore size, ligament size, and connectivity. This will allow the properties of these foams to be tailored to particular applications.

### **COMPOSITES AND THE QUEST FOR DUCTILITY**

From the point of view of structural applications, localization of plastic deformation into shear bands is the single biggest challenge because this tendency limits the tensile ductility, fracture toughness, and fatigue crack resistance of metallic glasses. There may well be no solution to this problem for monolithic metallic glasses, for the simple reason that they lack any microstructure to interact with shear bands.

Progress is likely to occur on two fronts. First, it is now well established that some alloys are inherently brittle, in the sense that they experience very little plastic deformation around a crack tip, while other alloys show extensive plastic deformation (albeit localized into shear bands). The precise reason for this difference is not understood at present, but it seems likely that it will be resolved with continued work on fundamental aspects of plastic deformation and fracture. This is likely to lead to development of new alloys with reasonable fracture toughness, although not to tensile ductility. However, even this will be an important step if such alloys can be used as matrices for composites.

Second, in order to achieve tensile ductility, it appears to be necessary to have some microstructural features to interact with shear bands. Furthermore, the length scale of the microstructure is clearly a critical parameter in arresting shear band propagation. Again, the precise reasons for this are not known, but continued research quite likely will lead to an improved understanding of the interactions between second-phase particles and shear bands.

At present, the most promising approach to producing composite materials with the proper microstructural length scale is the formation of dendritic composites, as discussed above. A critical limitation is that this process has been demonstrated in only two, closely related alloys and does not appear to be a general phenomenon.

Unfortunately, our understanding of thermodynamics and phase formation in complex multicomponent alloys is not such that we can predict a priori which alloys are capable of producing ductile dendrites in a glass-forming matrix. Until that understanding is developed, discovery of new dendritic composite materials will remain a matter of trial

and error. The potential benefits are significant, however, because there exists the possibility of making materials with exceptionally high strength, fracture toughness, and fatigue resistance.

## **Summary and Recommendations**

Metallic glasses combine some of the advantageous mechanical properties of metals—strength, stiffness, and in some cases toughness—with the processing flexibility usually associated with thermoplastic polymers. The absence of crystalline defects allows metallic glasses to be much stronger than conventional alloys but also means they have near-zero tensile ductility and poor fatigue resistance. In structural applications, therefore, metallic glasses are most likely to be useful in the form of composites consisting of ductile crystalline dendrites in a metallic glass matrix. These dendritic composites sacrifice some strength but can have exceptionally high fracture toughness, as well as good fatigue resistance, and could replace high-strength steels in certain load-limited structural components in aerospace vehicles where space is limited.

Because they are true glasses, thermoplastic forming near the glass transition temperature affords metallic glasses tremendous flexibility in processing. For instance, metallic glass components can be formed in a single step (for example, by injection molding) in complex geometries that would be difficult or impossible to produce with conventional alloys. In addition, metallic glass foams can be made with relative ease, raising the possibility of making structural foams with high strength and stiffness. Finally, because they lack a crystalline grain structure, metallic glasses can be used to form nanoscale features with high fidelity. This may make metallic glasses useful in a variety of micro-electromechanical systems (MEMS) applications.

Metallic glasses also have significant limitations for aerospace applications, however. Foremost among these is a lack of good glass-forming alloys; in particular, there are no good aluminum-rich glass-forming alloys, the known titanium-based alloys are either relatively dense (owing to high concentrations of alloying elements) or contain beryllium, and the known magnesium- and iron-based alloys are all quite brittle, with low fracture toughness. Although metallic glass matrix composites can have outstanding properties (particularly strength and fracture toughness), the number of good composite systems known at present is also quite limited.

For metallic glasses (and their composites) to be of broad utility in aerospace structural applications, progress in the following areas is required:

- Development of new lightweight alloys and composite systems, preferably by computational and/or combinatorial approaches rather than by trial and error.
- Understanding of mechanical behavior, especially:
  - The effect of alloy composition and structure on plastic deformation.
  - Microstructural design of composites for optimal toughness.
- Development of processing techniques, including thermophysical processing of complex and/or nanoscale features as well as production of metallic glass foams.

It is highly likely that continued work over the next 20-50 years will result in significant advances in all these areas, and that metallic glasses and metallic glass matrix composites will see increasing acceptance as structural materials. Whether or not they achieve widespread use in aerospace applications, however, depends critically on the development of new, lightweight alloys.

- <sup>1</sup> Z. P. Lu, Y. Liu, and C. T. Liu, Chapter 4 in *Bulk Metallic Glasses*, M. Miller and P. K. Liaw, eds. (Springer, 2009).
- <sup>2</sup> H. Men, W. T. Kim, and D. H. Kim, *Mater. Trans.* 44, 2142 (2003).
- <sup>3</sup> A. Peker and W. L. Johnson, *Appl. Phys. Lett.* 63, 2342 (1993).
- <sup>4</sup> N. Nishiyama and A. Inoue, *Mater. Trans. JIM* 37, 1531 (1996).
- <sup>5</sup> W. Zhang, Q. S. Zhang, and A. Inoue, *Mater. Trans.* 50, 679 (2009).
- <sup>6</sup> J. Schroers and W. L. Johnson, *Appl. Phys. Lett.* 84, 3666 (2004).
- <sup>7</sup> F. Guo, H. Wang, S. J. Poon, and G. J. Shiflet, *Appl. Phys. Lett.* 86, 091907 (2005).
- <sup>8</sup> V. Ponnambalam, S. J. Poon, and G. J. Shiflet, *J. Mater. Res.* 19, 1320 (2004).
- <sup>9</sup> A. H. Brothers and D. C. Dunand, *Scripta Mater.* 54, 513 (2006).
- <sup>10</sup> X. J. Gu, S. J. Poon, and G. J. Shiflet, *J. Mater. Res.* 22, 344 (2007).
- <sup>11</sup> Data from MatWeb, <[www.matweb.com](http://www.matweb.com)>.
- <sup>12</sup> Data from MatWeb, <[www.matweb.com](http://www.matweb.com)>.
- <sup>13</sup> Y. He, G. M. Dougherty, G. J. Shiflet, and S. J. Poon, *Acta Metall. Mater.* 41, 337 (1993).
- <sup>14</sup> Graphic reproduced from C. A. Schuh, T. C. Hufnagel, and U. Rammamurty, *Acta Mater.* 55, 4067 (2007) and used with the permission of Elsevier, Ltd. Original micrograph is from R. D. Conner, W. L. Johnson, N. E. Paton, and W. D. Nix, *J. Appl. Phys.* 94, 904 (2003).
- <sup>15</sup> P. Lowhaphandu and J. J. Lewandowski, *Scripta Mater.* 38, 1811 (1998).
- <sup>16</sup> Data from MatWeb, <[www.matweb.com](http://www.matweb.com)>.
- <sup>17</sup> C. J. Gilbert, V. Schroeder, and R. O. Ritchie, *Metall. Mater. Trans. A* 30, 1739 (1999).
- <sup>18</sup> B. Menzel and R. H. Dauskardt, *Acta Mater.* 54, 935 (2006).
- <sup>19</sup> M. E. Launey, D. C. Hofmann, W. L. Johnson, and R. O. Ritchie, *Proc. Nat. Acad. Sci.* 106, 4986 (2009).
- <sup>20</sup> A. L. Greer, K. L. Rutherford, and I. M. Hutchings, *Int. Mater. Rev.* 47, 87 (2002).
- <sup>21</sup> B. A. Green, P. K. Liaw, and R. A. Buchanan, Chapter 8 in *Bulk Metallic Glasses*, M. Miller and P. K. Liaw, eds. (Springer, 2009).
- <sup>22</sup> V. Schroeder and R. O. Ritchie, *Acta Metall.* 54, 1785 (2006).
- <sup>23</sup> Graphic reproduced from C. A. Schuh, T. C. Hufnagel, and U. Rammamurty, *Acta Mater.* 55, 4067 (2007) and used with the permission of Elsevier, Ltd.
- <sup>24</sup> A. Hernando and M. Vazquez, Ch. 17 in *Rapidly Solidified Alloys*, H. H. Liebermann, ed. (Marcel Dekker, 1993).
- <sup>25</sup> T. Richmond and H.J. Guntherodt, Ch. 14 in *Rapidly Solidified Alloys*, H. H. Liebermann, ed. (Marcel Dekker, 1993).
- <sup>26</sup> C. Haon, D. Camel, B. Drevet, and J. M. Pelletier, *Metall. Mater. Trans. A* 39, 1791 (2008).
- <sup>27</sup> Photograph by Todd Hufnagel.
- <sup>28</sup> C. C. Hays, C. P. Kim, and W. L. Johnson, *Phys. Rev. Lett.* 84, 2901 (2000).
- <sup>29</sup> C. Fan, R. T. Ott, and T. C. Hufnagel, *Appl. Phys. Lett.* 81, 1020 (2002).
- <sup>30</sup> D. Hofmann, J.-Y. Suh, A. Wiest, G. Duan, M.L. Lind, M. D. Demetriou, and W. L. Johnson, *Nature* 451, 1085 (2008).
- <sup>31</sup> D. Hofmann, J.-Y. Suh, A. Wiest, G. Duan, M.L. Lind, M. D. Demetriou, and W. L. Johnson, *Nature* 451, 1085 (2008).
- <sup>32</sup> D. Hofmann, J.-Y. Suh, A. Wiest, G. Duan, M.L. Lind, M. D. Demetriou, and W. L. Johnson, *Nature* 451, 1085 (2008).
- <sup>33</sup> Graphics reproduced from C. A. Schuh, T. C. Hufnagel, and U. Rammamurty, *Acta Mater.* 55, 4067 (2007) and used with the permission of Elsevier, Ltd. Original artwork provided by Charlie Hays, Caltech.
- <sup>34</sup> M. F. Ashby and A. L. Greer, *Scripta Mater.* 54, 321 (2006).
- <sup>35</sup> D. C. Hofmann, J.Y. Suh, A. Wiest, M.L. Lind, M. D. Demetriou, and W. L. Johnson, *Proc. Nat. Acad. Sci.* 105, 20136 (2008).
- <sup>36</sup> D. Hofmann, J.-Y. Suh, A. Wiest, G. Duan, M.L. Lind, M. D. Demetriou, and W. L. Johnson, *Nature* 451, 1085 (2008).
- <sup>37</sup> M. E. Launey, D. C. Hofmann, W. L. Johnson, and R. O. Ritchie, *Proc. Nat. Acad. Sci.* 106, 4986 (2009).
- <sup>38</sup> N. Barrington and M. Black, Ch. 1 in *Aerospace Materials*, B. Cantor, H. Assender, and P. Grant, eds. (Institute of Physics, 1998).
- <sup>39</sup> Data for metallic glasses are from X. J. Gu, S. J. Poon, and G. J. Shiflet, *J. Mater. Res.* 22, 344 (2007); D. Hofmann, J.-Y. Suh, A. Wiest, G. Duan, M.L. Lind, M. D. Demetriou, and W. L. Johnson, *Nature* 451, 1085 (2008); M. F. Ashby and A. L. Greer, *Scripta Mater.* 54, 321 (2006); D. C. Hofmann, J.Y. Suh, A. Wiest, M.L. Lind, M. D. Demetriou, and W. L. Johnson, *Proc. Nat. Acad. Sci.* 105, 20136 (2008); J. J. Lewandowski, W. H. Wang, and A. L. Greer, *Phil. Mag. Lett.* 85, 77 (2005). Data for other materials are from Cambridge Materials Selector, <<http://www.grantadesign.com/>>.

- 
- <sup>40</sup> M. D. Demetrlou, C. Veazey, J. S. Harmon, J. P. Schramm, and W. L. Johnson, *Phys. Rev. Lett.* 101, 145702 (2008).
- <sup>41</sup> C. Vermeeren, ed. *Around Glare: A New Aircraft Material in Context* (Kluwer, 2002).
- <sup>42</sup> D. V. Louzguine-Luzgin, D. B. Miracle, and A. Inoue, *Adv. Eng. Mater.* 10, 1008 (2008).
- <sup>43</sup> A. L. Greer, *Materials Today* 12(1-2), 14 (2009).
- <sup>44</sup> D. V. Louzguine-Luzgin, D. B. Miracle, and A. Inoue, *Adv. Eng. Mater.* 10, 1008 (2008).
- <sup>45</sup> Y. Li, Q. Guo, J. A. Kalb, and C. V. Thompson, *Science* 322, 1816 (2008).
- <sup>46</sup> Y. Li, Q. Guo, J. A. Kalb, and C. V. Thompson, *Science* 322, 1816 (2008).
- <sup>47</sup> T. Tamura, K. Amiya, R. S. Rachmat, Y. Mizutani, and K. Miwa, *Nature Mater.* 4, 289 (2005).
- <sup>48</sup> G. Kumar, H. X. Tang, and J. Schroers, *Nature* 457, 868 (2009).
- <sup>49</sup> A. L. Greer, *Materials Today* 12(1-2), 14 (2009).

UNCLASSIFIED//~~FOR OFFICIAL USE ONLY~~



# Defense Intelligence Reference Document

Acquisition Threat Support

7 January 2010

ICOD: 1 December 2009

DIA-08-0912-006

## Biomaterials

UNCLASSIFIED//~~FOR OFFICIAL USE ONLY~~

## Biomaterials

**Prepared by:**

(b)(3):10 USC 424

**Defense Intelligence Agency**

**Author:**

(b)(6)

**Administrative Note**

COPYRIGHT WARNING: Further dissemination of the photographs in this publication is not authorized.

This product is one in a series of advanced technology reports produced in FY 2009 under the Defense Intelligence Agency, (b)(3):10 USC 424 Advanced Aerospace Weapon System Applications (AAWSA) Program. Comments or questions pertaining to this document should be addressed to (b)(3):10 USC 424;(b)(6) AAWSA Program Manager, Defense Intelligence Agency, ATTN: (b)(3):10 USC 424 Bldg 6000, Washington, DC 20340-5100.

## Contents

Introduction.....	vi
Importance of Biocompatibility.....	vii
Science of Biomaterials.....	vii
Biomaterials for Biosensors.....	1
Biomaterials for Biomedicine.....	2
Biomedical Silicones - Polydimethylsiloxanes.....	2
Silicone Chemistry.....	4
Silicone in Biomedical Products.....	4
Teflon.....	6
Biodegradable Polymers.....	7
Biodegradation Advantages.....	8
Degradable Biomaterials.....	8
Polylactic Acid and Polyglycolic Acid.....	8
Polyethylene Glycol or Polyethylene Oxide.....	10
Hydrogels.....	10
Titanium – Hip and Knee Joints.....	11
BioCeramics.....	11
Dental Ceramics.....	13
Tissue Constructs as Biomaterials.....	13
Cardiovascular Biomaterials.....	15
Stent Biomaterials.....	18
Nitinol as a Biomaterial.....	19
Contact Lenses.....	19
Drug Delivery Polymers.....	20
Medical Titanium as a Biomaterial.....	22

Biomaterials in Dialysis ..... 24

Summary and Recommendations ..... 25

**Figures**

Figure 1. Biomaterial Applications in Medical Devices .....vi

Figure 2. Common Medical Devices That Use Biomaterials .....viii

Figure 3. Biomaterials Such as Polycarbonates, Cellulose, and Silicones Used in Membranes for Sensors, Dialyzers, and Oxygenators ..... 1

Figure 4. Photograph of Silicone (polydimethylsiloxane) Biomedical Implants Used in Breast Reconstructive Surgery ..... 3

Figure 5. Silicone Chemical Groups ..... 4

Figure 6. Silicone Tracheostomy Tube ..... 5

Figure 7. Silicone Sheets Used Under the Skin as a Physical Supporting Layer for Repair of Scar Tissue..... 5

Figure 8. Teflon Structure ..... 6

Figure 9. Expanded PTFE (Gore-Tex or ePTFE) Used in Lip Implants..... 7

Figure 10. Biodegradable Polymers..... 7

Figure 11. Structure of Polylactic Acid (a Biodegradable Polymer) ..... 9

Figure 12. Biodegradable PLA as an Antiadhesion Barrier after Open-Heart Surgery ..... 9

Figure 13. Biodegradable Polymers Based on Copolymers of Polylactic Acid and Polyethylene Glycol (Polysciences Inc) ..... 10

Figure 14. Dots of Hydrogel..... 10

Figure 15. Various Titanium Components Used in Hip Joint Replacement ..... 11

Figure 16. Hydroxyapatite Porous Bone-Like Structure After Commercial Processing ..... 12

Figure 17. Bioceramic Used in Artificial Hip Replacement Component..... 12

Figure 18. Computer-Based Sculpted Ceramic Teeth ..... 13

Figure 19. Scaffold-Guided Tissue Regeneration ..... 14

Figure 20. Biodegradable Material CSLG Deposited in a Honeycomb Structure to Allow Infiltration by Living Cells While in a Submerged Cell Culture ... 15

Figure 21. Some of the More Popular Biomedical Devices and Duration of Their Blood Contact..... 16

Figure 22. Gore Medical Teflon Foam Used in Vascular Grafts ..... 16

Figure 23. Illustration of Treatment of an Atrial Septal Defect Using a Teflon-Based Product Manufactured by Gore, Inc. .... 17

Figure 24. Stainless Steel and Teflon Bjork Shiley Heart Valve ..... 18

Figure 25. Illustration of Stent Placement ..... 18

Figure 26. Nitinol Stent ..... 19

Figure 27. Contact Lens..... 20

Figure 28. Schematic Representation of Biodegradable (Bioerodible) Drug Delivery Device ..... 21

Figure 29. Photomicrograph of Titanium Metal (Appears Black in This Photo) in an Intimate Integration With Living Bone..... 23

Figure 30. Illustration (Left) and Photograph (Right) of a Blood Dialyzer as Used in Medicine ..... 24

Figure 31. Cuprophane Membrane Passes Blood Waste Products (Violet and Orange Dots) Through Pores and Blocks Passage of Red Blood Cells .. 25



## Biomaterials

### Introduction

Biomaterials are metals, ceramics, polymers, glasses, carbons, and composite materials intended to interface with biological systems. They are often used to treat, augment, or replace bodily tissues, organs, or functions. Such materials are used in various forms, including molded or machined parts, coatings, fibers, films, foams, and fabrics. Biomaterials are usually nonliving, but recent definitions also include living skin and tissues produced in culture.

A biocompatible material is different from a biological material produced by a biological system, such as bone. Artificial hips, vascular stents, artificial pacemakers, and catheters are all made of biocompatible materials that typically have a synthetic origin. An extraordinarily wide range of medical devices are made from biomaterials. Figure 1 shows some representative examples of medical devices that use biomaterials.

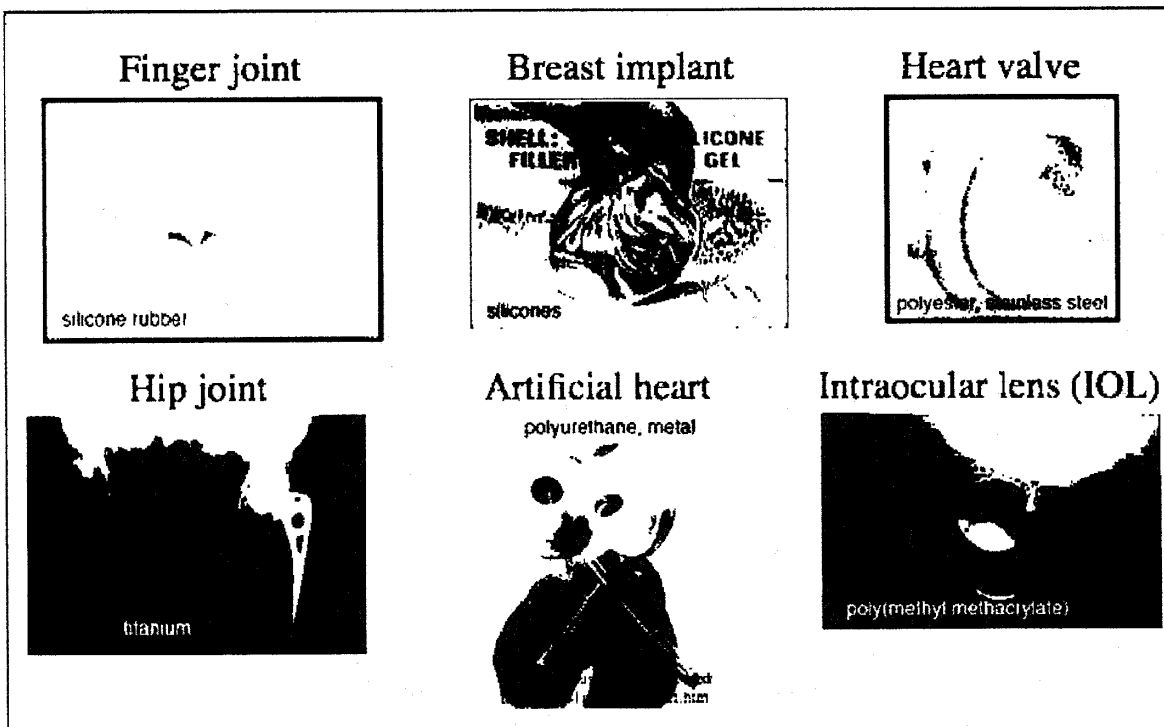


Figure 1. Biomaterial Applications in Medical Devices

Encompassing elements of medicine, biology, chemistry, and materials science, biomaterials science has experienced steady and strong growth over its approximately half-century history.

Although biomaterials are used primarily for medical applications, they are also used to grow cells in culture, to assay for blood proteins in the clinical

laboratory, in processing biomolecules in biotechnology, for fertility regulation implants in cattle, in diagnostic gene arrays, in the aquaculture of oysters, and for investigational cell-silicon "biochips." The common thread in these applications is the interaction between biological systems and synthetic or modified natural materials.

Biomimetic materials, in contrast, are not made by living organisms but have compositions and properties similar to materials made by living organisms. For example, the calcium hydroxyapatite coating found on many artificial hips—used as metal-bone interface cement to make it easier to attach implants to bone—is similar to the coating found in mollusk shells.

### **IMPORTANCE OF BIOCOMPATIBILITY**

Biocompatibility is an important issue in biomedical implants and sensors. A material-tissue interaction that results from implanting a foreign object in the body is a major obstacle to developing stable and long-term implantable devices and sensors.

The processes that occur when sensors are placed in the complex living environment of the human body are sometimes known as biofouling. In biofouling, the physical or chemically sensitive portion of the sensor interface becomes coated with proteins, blood-formed elements, adherent immunological cells, and sometimes forms of scar tissue that tend to isolate the sensor from the rest of the body environment. This response of tissue is a foreign body reaction to any object introduced in tissue that does not express surface characteristics that identify it as part of the host tissues.

Experiences of many investigators (more than 600 reported studies since 1996) with the biocompatibility of biomaterials related to the function of implanted biosensors have been poor such that many companies have abandoned implantable sensor devices altogether. Rather, the recent trend in medical biosensors is toward placing them outside the body. Newer sensors are often based on optical principles in an effort to obviate the biocompatibility and biomaterial issues of placing sensors inside the human body.

### **SCIENCE OF BIOMATERIALS**

The study and use of biomaterials bring together researchers from diverse academic backgrounds who must communicate clearly. Professions that intersect in the development, study, and application of biomaterials include bioengineer, chemist, chemical engineer, electrical engineer, mechanical engineer, materials scientist, biologist, microbiologist, physician, veterinarian, ethicist, nurse, lawyer, regulatory specialist, and venture capitalist.

The number of medical devices used each year in humans is very large. Figure 2 estimates usage for common devices, all of which employ biomaterials.

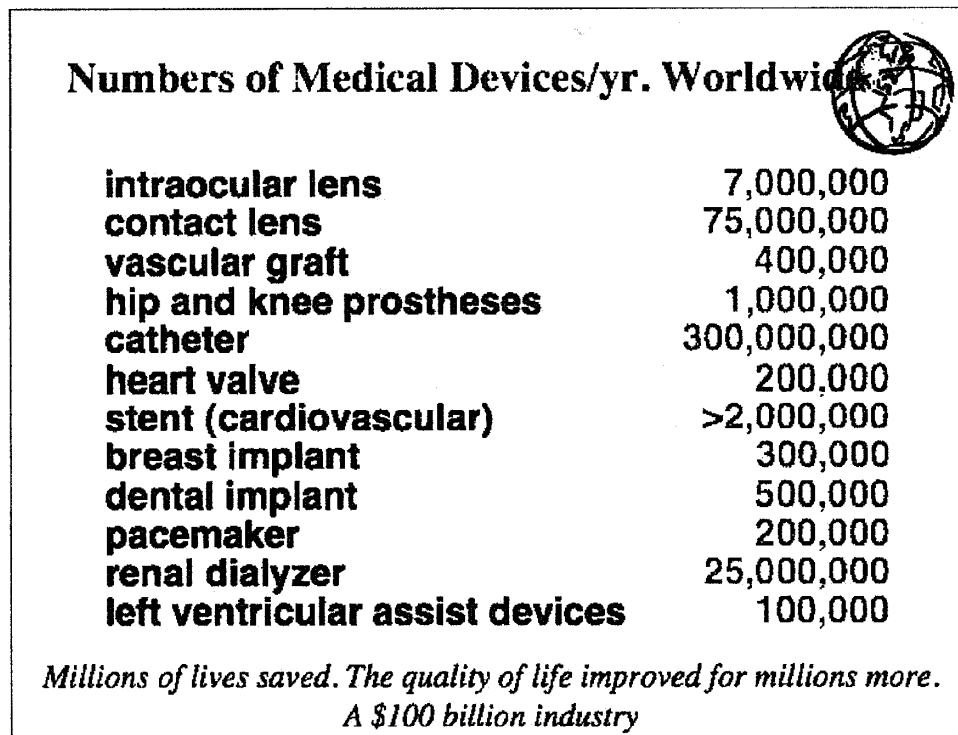


Figure 2. Common Medical Devices That Use Biomaterials

The development of biomaterials is the junction of materials science and chemistry. Medical devices may be composed of a single biomaterial or a combination of several materials. A heart valve might be fabricated from polymers, metals, and carbons. A hip joint might be fabricated from metals and polymers (and sometimes ceramics) and will be interfaced to the body through a polymeric bone cement.

Biomaterials by themselves do not make a useful clinical therapy but rather have to be fabricated into devices. This is typically an engineer's role, but the engineer might work closely with synthetic chemists to optimize material properties and with physicians to ensure the device is useful in clinical applications.

Biomaterials must be compatible with the body, and there are often issues that must be resolved before a product can be placed on the market and used in a clinical setting. Because of this, biomaterials are usually subjected to the same very stringent safety requirements as those of new drug therapies.

## Biomaterials for Biosensors

Implantable biosensors for the human body place some of the greatest functional demands on biomaterials. Biosensors monitor the physiologic state of tissues for medical therapeutics or for assessing human performance. Sensors for glucose, oxygen, blood pH, adrenal hormones, nervous activity, heart performance, and blood pressure monitors are all of interest.

Blood biochemistry sensors are the most difficult sensors to keep functioning over time primarily because the sensor interface materials provoke low-level foreign-body reactions in tissues. These types of responses are not specifically important to implantable devices that have structural rather than sensing functions, such as heart valves, but they can completely render a biosensor for blood glucose, for example, useless after a few days.

Chemically sensitive biosensor interfaces to tissue and body environments employ membranes in an effort to protect the biosensor active-sensing surface from possible body reactions. The membrane allows small molecules of interest to pass through its pores while excluding larger proteins, blood-formed elements, and cells like macrophages that would engulf the sensor.

The membrane's biomaterial composition, pore size, and long-term physical integrity are critical components in the functioning of the sensor. If the biomaterial chosen retards the adhesion of proteins and does not provoke a biological response, then this improves sensor longevity. Figure 3 shows some representative biomembranes.

No one biomaterial is best for all sensor applications, primarily because different biomaterials behave differently relative to the substance being sensed. Membranes that pass glucose, for example, may not pass oxygen that is needed for a sensor to function. Membrane biofouling starts immediately upon contact of the sensor with the body cells. Proteins and other biological components adhere to the sensor surface, and in some cases, impregnate the pores of the material. This process retards diffusion of the molecules of interest to the sensor surface and either slows the sensor's response to changes in concentration or reduces the overall response to the point where the sensor falls out of calibration.

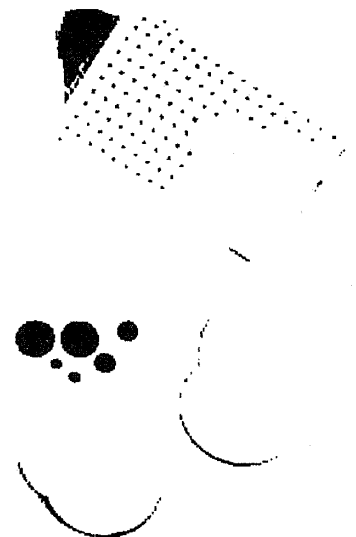


Figure 3. Biomaterials Such as Polycarbonates, Cellulose, and Silicones Used in Membranes for Sensors, Dialyzers, and Oxygenators

The design of sensor membrane materials has been found to be critically dependent on subtle features of the membrane's chemistry, material thickness, and porosity, as well as, more generally, where in the human body the sensor is located. The blood stream is

the most hostile location both for sensor performance and in terms of the potential for danger to the patient through the provocation of blood clotting.

The most successful biomembrane materials have been porous forms of Teflon, polyurethanes, and cellulose-based materials such as cellulose acetate. As important as the material composition is for sensors, so are aspects of a membrane's structure and mechanical properties, such as its ability resist abrasion and adhere to sensor surfaces.

## **Biomaterials for Biomedicine**

In this review, we look at representative biomaterials as well as representative applications. These biomaterials are among the most popular of those used in medicine today, and the applications in some cases represent multibillion-dollar-a-year markets.

Some of the best known of the biomaterials are:

- Silicone
- Teflon
- Biodegradable polymers
- Hydrogels
- Titanium alloys
- Ceramics
- Tissue constructs

Some of the largest applications are:

- Cardiovascular – stents, synthetic blood vessels, heart valves
- Hip and knee joints
- Contact lenses
- Drug delivery devices
- Kidney dialysis

### **BIOMEDICAL SILICONES- POLYDIMETHYLSILOXANES**

Perhaps the most well known of all biomaterials are the silicones—soft, pliable, and semitransparent materials that are used in many different applications in modern society, ranging from water sealants to fibrous insulations.

Silicone is often mistakenly called "silicon." Although silicones contain silicon atoms, they are an organic material of greater complexity and are not made up exclusively of silicon. Silicone is used in an exceptionally large number of biomedical applications. It is blood compatible, sterilizable, rugged, and strong but flexible. Its mechanical properties

can be tailored to varying degrees of hardness and strength for stiffness in catheter applications.

Biomedical silicones attracted notoriety in 1995 when a class-action lawsuit against Dow Corning, Inc., brought a huge settlement resulting from the supposed dangers of silicone breast implants.

After reviewing years of evidence and research concerning silicone gel-filled breast implants, the national Institute of Medicine found that "evidence suggests diseases or conditions such as connective tissue diseases, cancer, neurological diseases or other systemic complaints or conditions are no more common in women with breast implants than in women without implants." Dow moved out of the medical silicone business and has since been replaced by an array of smaller companies offering specialized silicone products.

Figure 4 shows the present form of silicone used for reconstructive surgery following a mastectomy, particularly after breast cancer in women.

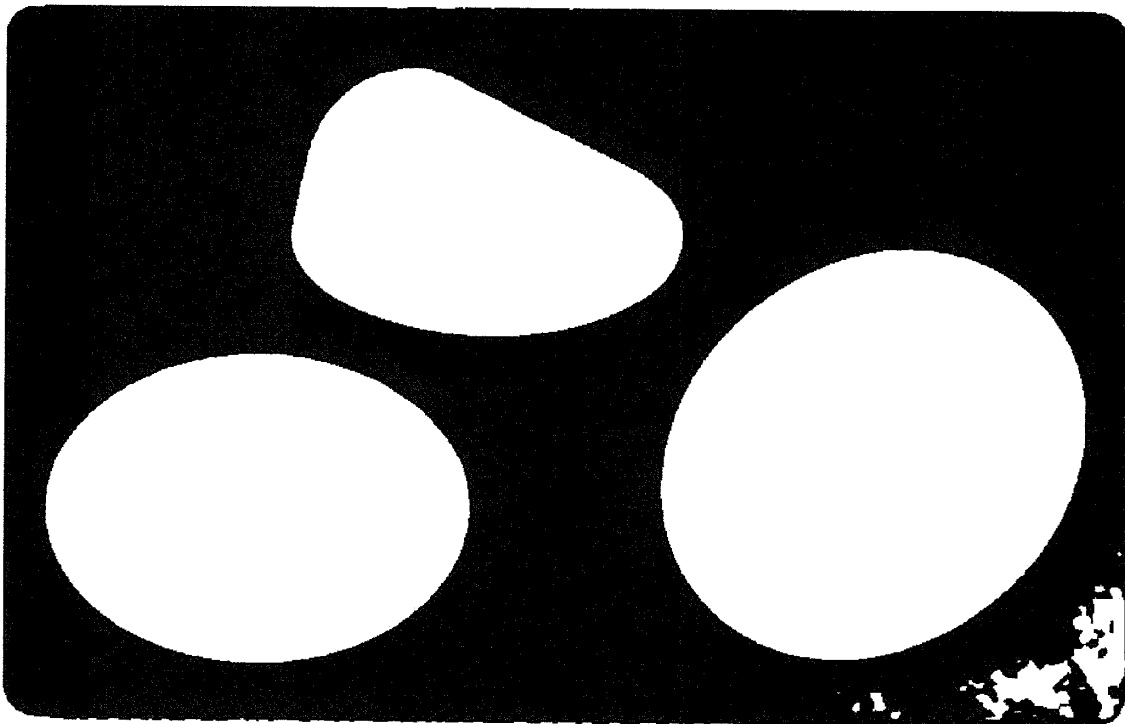


**Figure 4. Photograph of Silicone (polydimethylsiloxane) Biomedical Implants Used in Breast Reconstructive Surgery**

## SILICONE CHEMISTRY

Silicone is actually a common name for the chemical compound polydimethylsiloxane (PDMS), a class of synthetic polymers with repeating units of silicon and oxygen. Figure 5 shows the polymeric repeating structure of medical silicones. Various functional groups—often methyl—can be attached to that backbone to change the material properties. Silicone polymers can easily be transformed into linear or cross-linking materials without using any toxic plasticizers. The resulting materials are elastic at body temperature.

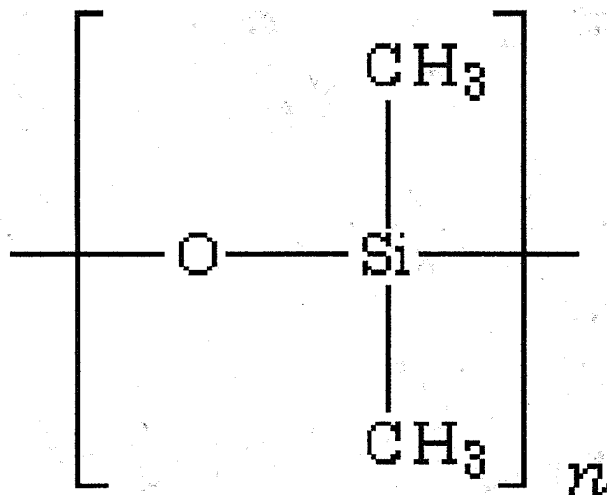


Figure 5. Silicone Chemical Groups

The simultaneous presence of different groups attached to the silicon-oxygen backbone gives silicones a range of viscous and mechanical properties that allow their use as fluids, emulsions, compounds, resins, and elastomers in numerous applications. Thus, silicone is a versatile polymer, although its use is often limited by its relatively poor mechanical strength. However, this limitation can be overcome by reinforcing silicone with a silica filler or by chemically modifying the backbone.

The stability, lack of toxicity, and excellent biocompatibility of PDMS make these materials well suited for use in personal care, pharmaceutical, and medical device applications. Silicone is easily molded and cast using room temperature curing (known as RTV) or through the use of an organic catalyst.

## SILICONE IN BIOMEDICAL PRODUCTS

Silicone membranes are made by casting the silicone liquid precursor into thin sheets. Such membranes are often used in oxygen and carbon dioxide blood biosensors because membranes made of this material are highly transmissive to these gases while they block most other chemical substances present in the blood stream. In addition, silicone's resistance to protein adhesion and its excellent overall biocompatibility make it one of the most commonly used materials for encapsulating biosensors for tissue or blood contact.

Recent formulations of silicone can be patterned with ultraviolet light and, thus, lend themselves to manufacture with biosensors made by photolithography.

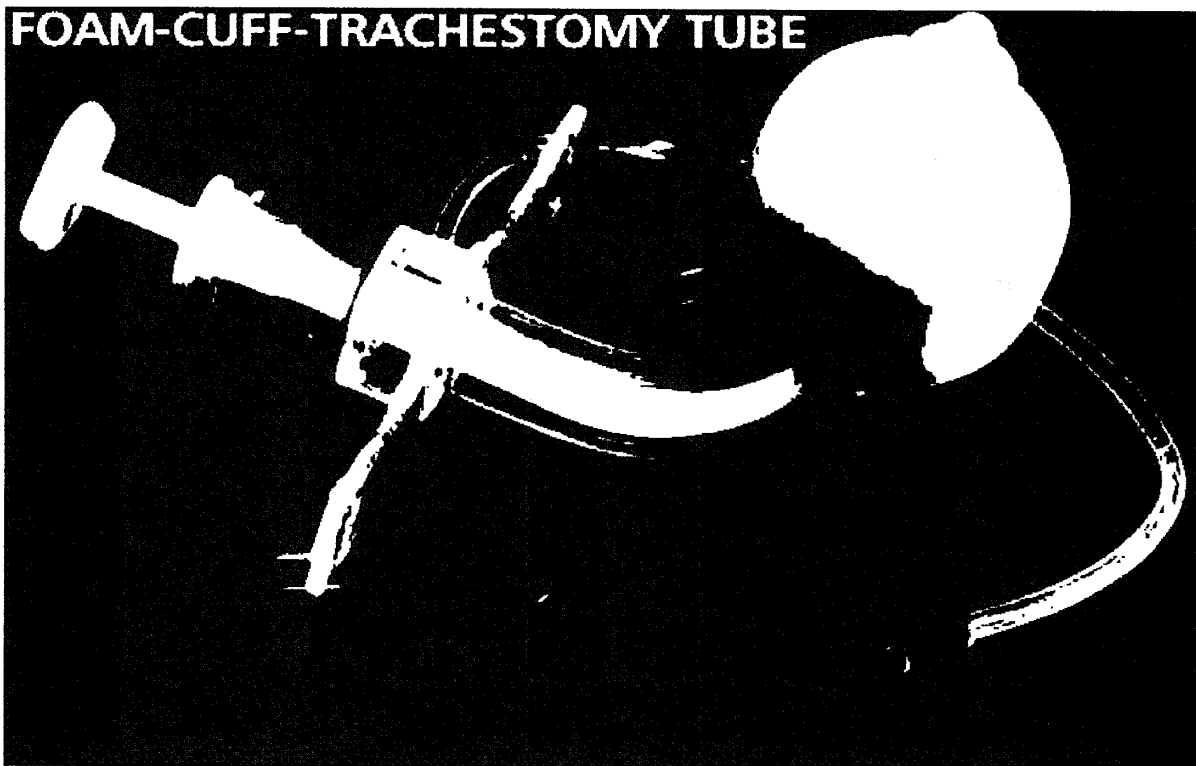


Figure 6. Silicone Tracheostomy Tube

Figure 6 is a representative example of silicone-based medical products involving tubes or catheters. A tracheostomy tube, or "trach tube," is a 2- to 3-inch-long curved metal or plastic tube placed in a surgically created opening (tracheostomy) in the windpipe to keep it open. Versions of these products are used in cases where patients have difficulty breathing on their own, such as in a spinal cord injury.

A product known as Mepiform™ is an example of silicone use in a sheet form for the management of scars, particularly keloid scars. Figure 7 shows this product.



Figure 7. Silicone Sheets Used Under the Skin as a Physical Supporting Layer for Repair of Scar Tissue



## TEFLON

Biomedical materials must be inert to the complex chemistry of biological fluids so they neither suffer nor instigate change in tissue. Teflon™ admirably fulfills these requirements. Teflon is a trade name for polytetrafluoroethylene (PTFE), a fluorocarbon-based polymer. It is made by free radical polymerization of tetrafluoroethylene and has a carbon backbone chain in which each carbon has two fluorine atoms attached to it.

This polymer is hydrophobic (water hating), biologically inert, and nonbiodegradable and also has low friction characteristics and excellent "slipperiness." The chemical inertness (stability) of PTFE is related to the strength of the fluorine-carbon bond that makes it resistant to adhesion. Figure 8 shows the structure of this material. It is a long chain of repeating chemical units, as shown in the right of the figure.

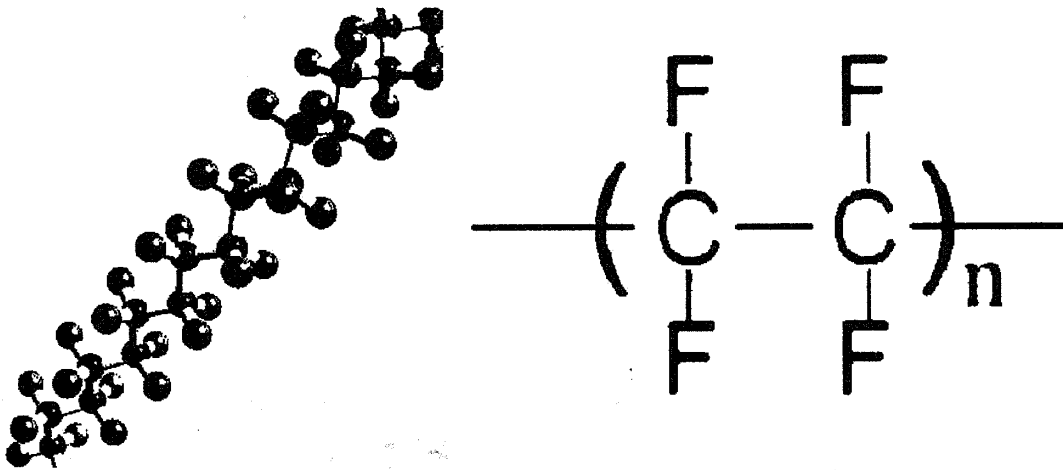


Figure 8. Teflon Structure

Goretex® is a medical form of Teflon (PTFE) that, when stretched and extruded, entraps air cells in its microstructure much like foam does and, thus, is relatively soft and repellant to most liquids. This material is known as e-PTFE (expanded PTFE).

PTFE can be fabricated in many forms, including pastes, tubes, strands, and sheets, while ePTFE can be woven into a porous, fabric-like mesh. When implanted in the body, this strong mesh allows tissue to grow into its pores, making it ideal for medical devices such as vascular grafts.

Preformed ePTFE subcutaneous implant materials have been used to improve facial reconstruction and cosmetic surgery outcomes. Figure 9 is a manufacturer's product information showing the utility of using ePTFE in cosmetic surgery.

PTFE has relatively low wear resistance, but under compression or in situations where rubbing or abrasion can occur, it can produce wear particles. These can result in a chronic inflammatory reaction, an undesirable outcome. For a given application, the biomaterials engineer must consider many aspects of the physical and biological properties of the materials. Thus, although PTFE is highly inert in the body, applying it in the wrong circumstances (for example, to a device that is under compression or exposed to wear) may lead to a reaction that no longer qualifies as "biocompatible."

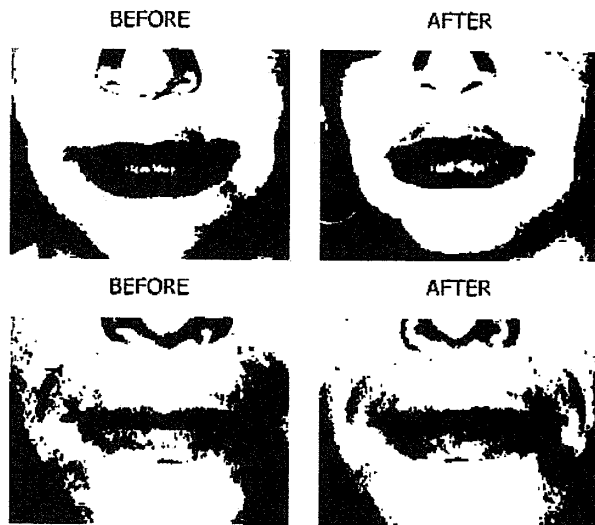


**Figure 9. Expanded PTFE (Gore-Tex or ePTFE) Used in Lip Implants.** This is a synthetic implant that has been used in the face and body for many years. The main advantage is that it is not absorbed over time and the results are permanent.

## BIODEGRADABLE POLYMERS

Biodegradable polymers are an important and relatively large category of biomaterials that are used extensively in the medical and food industries. In the latter, they are used as food wrappings and other packaging derived from natural food substances that slowly degrade—by evaporation into water vapor and carbon dioxide—when exposed to the sun and outdoor environments, thus minimizing waste disposal. Figure 10 shows a complex shape made from polylactide (PLA), a biodegradable polymer.

Biodegradable polymers can be either natural or synthetic. In general, synthetic polymers offer greater advantages than do natural materials in that they can be tailored to give a wider range of properties and more predictable lot-to-lot uniformity than can materials from natural sources. Synthetic polymers also represent a more reliable source of raw materials—

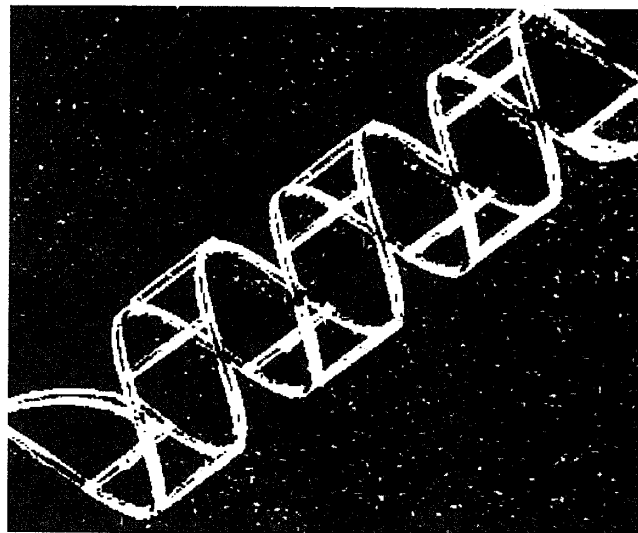


**Figure 10. Biodegradable Polymers.** Polymers such as PLA are much like conventional plastics and, as such, have qualities of clarity, flexibility, and strength.

one free from concerns of immunogenicity. These polymers can be optically clear, exhibit good flexibility, and have strength comparable to that of many plastics.

### **BIODEGRADATION ADVANTAGES**

In the human body, biodegradable polymers have good compatibility but also decompose to harmless materials and over time dissolve altogether. Biodegradable polymers undergo a chemical hydrolysis in the salty and wet environment of tissues by way of a labile chemical backbone of the polymer. The degradation starts immediately upon water exposure and occurs in two steps.

In the first step, the material thoroughly hydrates, and the water attacks the polymer chains, converting long chains into shorter, water-soluble fragments. The desirable aspect of this process is a reduction in molecular weight without a loss in physical properties, since the device matrix is still held together, even with the shorter chains.

In the second step, the shorter polymer chains are attacked by enzymes that are naturally present in tissues. Basically, a metabolization of the fragments by the body tissues results in a rapid loss of polymer mass, what is referred to as bulk erosion. All the commercially available synthetic devices and sutures degrade by bulk erosion.

### **DEGRADABLE BIOMATERIALS**

Different biodegradable polymers have different lifetimes in tissues, ranging from a few days to years. Combining two different biopolymers—for example, short-lived (days) PLA (polylactide) and longer lived (months) PGA (polyglycolide)—reveals that polymers can be produced with intermediate decomposition times. Thus, their decay times can be custom determined through their formulation.

Biodegradable polymers fulfill a physician's desire to have an implanted device that will not require a second surgical intervention for removal, which is desirable in many applications. In orthopedic applications, for example, a fractured bone that has been fixated with a rigid, nonbiodegradable stainless implant has a tendency for refracture upon removal of the implant, making removal undesirable. This refracturing results from the offloading of the stress on the bone by the stainless steel support because the bone has not carried a sufficient load during the healing process. However, a fixation system prepared from a biodegradable polymer can be engineered to degrade at a rate that will slowly transfer the load to the healing bone, thereby avoiding the risk of refracture and eliminating the need to remove the implant.

### **POLYLACTIC ACID AND POLYGLYCOLIC ACID**

Polylactic acid (PLA), polyglycolic acid (PGA), and their copolymers are the most widely used of the biodegradable polymers. These materials, when exposed to the sun and weather, will degrade into water and carbon dioxide and essentially vanish, given sufficient time.

In the human body, combinations of PLA and PGA are used to control the longevity of a material by controlling its degradation rate when exposed to tissues. The degradation products in the human body are also water and carbon dioxide.

PLA, or polylactide, is a thermoplastic, long-chained organic material derived from renewable resources, such as corn starch (in the United States) or sugarcane (in the rest of the world). PLA has been recognized for more than a century and is of commercial interest primarily because of its biomedical applications. Figure 11 shows the chemical structure of PLA.

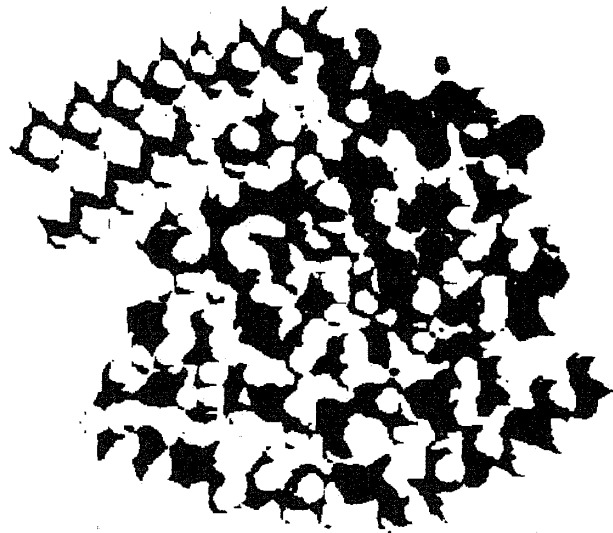


**Figure 11. Structure of Polylactic Acid (a Biodegradable Polymer)**

These materials are popular because they have already been used in many approved medical implant devices and have been shown to be safe, nontoxic, and biocompatible. They have been used in the development of several commercially available medical products, including sutures, tissue screws and tacks, guided tissue-regeneration membranes for dentistry, internal bone-fixation devices, microspheres for implantable drug delivery systems, and meniscus and cartilage repair systems.

These polymers can potentially be used in the design of vascular and urological stents and skin substitutes. This is possible through the manipulation of the polymer characteristics of these materials, such as their three-dimensional architecture, their mechanical and structural integrity, and their biodegradability. The materials can also be used as scaffolds for tissue engineering and for tissue reconstruction.

A medical application of these materials in thin-sheet form is their placement as a thin barrier layer that prevents entry of debris into wounds and as an underlayer to the skin and body tissue. Figure 12 is an artist's conception of a layer of PLA polymer being placed over the heart after open-heart surgery.

### *The Clear Choice*



*Protection in case there is a re-operation...*

**Figure 12. Biodegradable PLA as an Antiadhesion Barrier after Open-Heart Surgery**

The PLA sheet acts as a barrier and spacer to prevent the healing heart wall from growing an attachment to the chest wall and from forming adhesions onto the overlying

tissues. The barrier remains in place only for a week or so during the healing process before biodegrading so no foreign body is left inside of the body.

### **POLYETHYLENE GLYCOL OR POLYETHYLENE OXIDE**

Polyethylene glycol (PEG) is a widely used material in biomedicine, pharmaceuticals, cosmetics, and agriculture. Its chemical compatibility, water solubility, nontoxicity, biocompatibility, and multiple physical states allow it be used as coatings and in solid form to create surfaces that are very acceptable to biology. Figure 13 shows the marketing of PEG to broad markets that include biodegradable polymers.

One of PEG's major applications is in the creation of "nonfouling" surfaces when exposed to blood or biological environments. The nonfouling, or cell- and protein-resistant, properties of surfaces containing PEG are due to the material's highly hydrated state.

PEG is used in drug delivery systems to improve the solubility of drugs and to help stabilize immunogenic or unstable protein drugs. This can enhance the circulation times and stabilities of drugs in the body.

### **HYDROGELS**

Hydrogels are liquid or semisolid materials that have a strong affinity for water. Poly(hydroxyethyl methacrylic acid, or poly(HEMA), is one of the most important hydrogels in the biomaterials world because it has many advantages over other hydrogels. These include a water content similar to living tissue, inertness to biological processes, resistance to degradation, permeability to metabolites, and resistance to absorption by the body.

Poly(HEMA) can easily be manufactured into many shapes and forms and be easily sterilized. This is due to its structure, which is



Figure 13. Biodegradable Polymers Based on Copolymers of Polylactic Acid and Polyethylene Glycol



Figure 14. Dots of Hydrogel

composed of long-chain molecules crosslinked to one another to create many small empty spaces that can absorb water or other liquids like a sponge. Hydrogels can be extruded into nearly any shape. Figure 14 shows them as small dots.

If the spaces are filled with a drug, the hydrogel can dispense the drug gradually as the structure biodegrades. Hydrogels are also used for tissue engineering and tissue repair, where the spaces in the gel might be filled with stem cells, tissue-growth factors, or a combination of the two.

Hydrogels are cross-linked polymer networks that are insoluble in body fluids but are able to swell and often have a water content of up to 90 percent. These can be formed by crosslinking one or several types of monomer units into a network, forming a homopolymer, copolymer, or multipolymer. With the incorporation of different monomers, gels with wide-ranging chemical and physical properties can be formed. The gels can be neutral or charged, soft or stiff, strong or brittle. Hydrogels are routinely used for biomedical and pharmaceutical applications such as drug release, artificial tendons, wound-healing bioadhesives, artificial kidney membranes, artificial skin, and contact lenses.

### **TITANIUM – HIP AND KNEE JOINTS**

Titanium-based hip and knee implants are quite successful and are among the most common orthopedic procedures. When a hip replacement is performed, the arthritic, damaged hip joint is removed. The ball-and-socket hip joint is then replaced with an artificial implant.

Hip implants often show no visible sign of their existence in either walking gait or functionality. In adults, they can last a lifetime. Knee implants are also known to be successful. Figure 15 shows an assortment of titanium hip joint assemblies. The long shaft part of the device fills a drilled hole in the long bone of the femur.

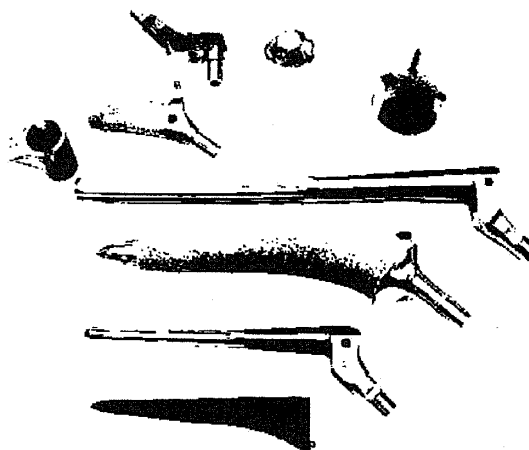


**Figure 15. Various Titanium Components Used in Hip Joint Replacement**

### **BIOCERAMICS**

Ceramic materials are sometimes used directly or modified for use in applications in the human body and, so, become known as bioceramics.

The most common applications are in bone repair, dentistry, and the use of ceramics in hip and knee joint replacements, where their exceptional hardness can be put to advantage in wear joints.

Bioceramics range in biocompatibility from the ceramic oxides, which are inert in the body, to the other extreme of resorbable materials, which are eventually replaced by the materials they were used to repair.

Two common ceramics used in dentistry and hip prostheses are alumina and hydroxyapatite (HA). HA is a major component of the inorganic compartment of bone. Commercially prepared HA is processed using a technique of phosphoric acid and hydrothermal exchange that produces a porous, "bone-like" morphology in the resulting structure. Figure 16 shows this result. When implanted into bone defects, HA supports bone growth through the pores and, thus, becomes an intermediate scaffold, as well as an eventual support matrix.



Figure 16. Hydroxyapatite Porous Bone-Like Structure After Commercial Processing

Hydroxyapatite composites have been successfully used to repair, reconstruct, and replace diseased or damaged body parts, especially bone. They have been used in vertebral prostheses, intervertebral spacers, bone grafting, middle-ear bone replacements, and jawbone repair.

Aluminum oxide, or alumina ( $Al_2O_3$ ), has been used in orthopedic surgery for more than 20 years as the joint surface in total hip prostheses because of its exceptionally low coefficient of friction and minimal wear rates. Alumina has excellent corrosion resistance, good biocompatibility, high strength, and high wear resistance, making it ideal for orthopedic applications.

Other bioceramics include coral skeletons, which can be transformed into hydroxyapatite by high temperatures. Their porous structure allows relatively rapid ingrowth of living cells at the expense of initial mechanical strength. The high temperature also burns away any organic molecules, such as proteins, preventing graft-versus-host disease and rejection.



Figure 17. Bioceramic Used in Artificial Hip Replacement Component

an increase in the interfacial area between the implant and the tissues. This tissue ingrowth results in an increased resistance to device movement within the tissue. As in natural bone, proteins adsorb to the calcium phosphate surface to provide the critical intervening layer through which the bone cells interact with the implanted biomaterial. Figure 17 shows an example of this.

## **DENTAL CERAMICS**

Dental ceramics are a major subclass of biomaterials. Porcelains are hard ceramic materials that are based on a glass of silica and alumina, with fluxes used to lower their fusion temperature. Dental porcelains can have a hardness that exceeds that of the enamel of natural teeth, but they are often more brittle and more likely to fracture. They also do not have the same optical properties, thermal conductivity, or natural fluorescence as biological materials.

Full-porcelain (ceramic) dental materials include porcelain, ceramic, or glasslike fillings and crowns (a metal-free option known as a jacket crown). They are used as inlays, onlays, crowns, and aesthetic veneers. A veneer is a very thin shell of porcelain that can replace or partially cover tooth enamel. Full-porcelain (ceramic) restorations are particularly desirable because their color and translucency mimic natural tooth enamel.

Zirconium oxide is a very strong and refractory material that has recently appeared as a dental material. With a three-point bending strength exceeding 900 megapascals, zirconium oxide is expected to be applicable to many new applications in dentistry, including bridges, implant suprastructures, and root dowel pins.

Casting the shape of a broken tooth into a natural shape or one that resembles the fragment of the broken tooth is greatly facilitated by the use of computerized CAD/CAM technologies. These technologies are used to make molds for the casting of dental ceramics. Figure 18 illustrates natural-looking teeth made from dental porcelains defined by a computer-generated mold.

## **TISSUE CONSTRUCTS AS BIOMATERIALS**

**Figure 18. Computer-Based Sculpted Ceramic Teeth**

Living tissues are sometimes considered biomaterials if they have been cultured prior to application to the human body or utilized much the same way as a synthetic material would be utilized. The formation of living tissues into constructs is sometimes called tissue engineering. This is a bit of a misnomer in that it is an advanced form of cell culture and cellular biology and has little in common with engineering in the classical sense of application of mathematics and physics to problems.

Rather, tissue engineering is the application of biological and cell culturing techniques to encourage the growth of tissues in certain ways and in the development of viable substitutes that restore and maintain the function of human tissues. This is a form of



medical therapeutics and differs from standard drug therapy or permanent implants in that the culture becomes integrated within the patient, affording a potentially permanent and specific cure of the disease state.

There are many approaches to tissue engineering, but all involve one or more of the following key ingredients: harvested cells, introduction of specialized signaling molecules, and three-dimensional matrices.

The approach involves seeding highly porous biodegradable matrices (or scaffolds) in the shape of the desired bone or tissue, with cells and signaling molecules (for example, protein growth factors), then culturing and implanting the scaffolds into the defect to induce and direct the growth of new bone or tissue. The goal is for the cells to attach to the scaffold, multiply, differentiate (that is, transform from a nonspecific or primitive state into cells exhibiting the specific functions), and organize into normal, healthy tissue as the scaffold degrades. The signaling molecules can be adhered to the scaffold or incorporated directly into the scaffold material. Figure 19 illustrates the sequence of steps in this process.

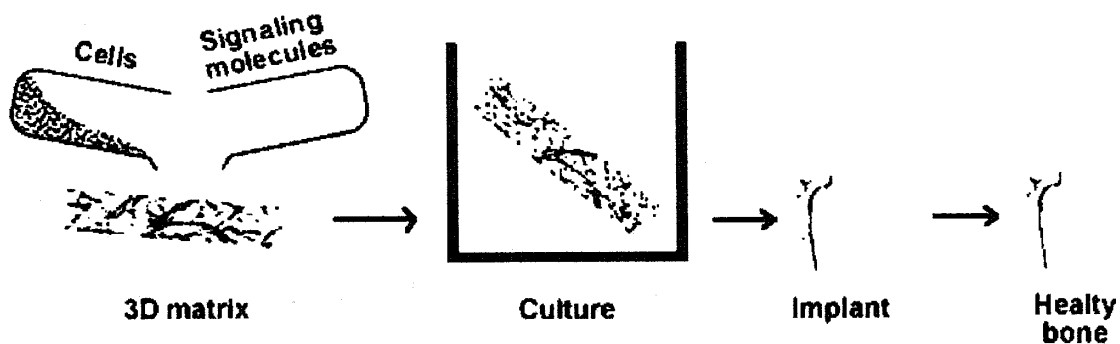


Figure 19. Scaffold-Guided Tissue Regeneration

Perhaps the biggest challenge for tissue engineering is how to ensure angiogenesis in a timely fashion within the scaffold construct; without a blood supply, cells will die, and mass infection will occur.

In biology, "autologous" refers to cells, tissues, or even proteins that are reimplanted into the same individual they were taken from. Bone marrow, skin biopsy, cartilage, and bone can be used as autografts. In contrast, cells or tissues transplanted from a different individual are referred to as allogeneic, homologous, or an allograft.

### TISSUE SCAFFOLD BIOMATERIALS

An intriguing idea in tissue engineering is the use of biodegradable polymers as a scaffold for growing tissues of a certain defined shape—for example, the cartilage of an ear pinna lost in an accident.

Biodegradable polymers have been used with computer-based rapid prototyping machines to form porous shapes where tissue cells can ingrow. The result after many weeks of submersion in tissue culture is that the polymer slowly degrades, leaving the cultured tissue in the shape of the predefined scaffold. Although this approach cannot grow complex organs, like a heart or kidney, that have many different tissues, it can be used to create simple structures of cell products—for example, of cartilage excreted by fibroblast cells. These structures do not create their own networks of blood vessels, a problem whose solution lies in the future.

Figure 20 shows CSLA (Crosslinkable Star Lactide-co-Glycolide), a biodegradable polymer deposited into a honeycomb structure by a process not unlike ink-jet printing. The ink-jet pen is supplied with a hot liquid form of the CSLA polymer, which then hardens when it cools and is exposed to the air. Using a computer to rewrite successive layers on top of one another, a three-dimensional structure is built.

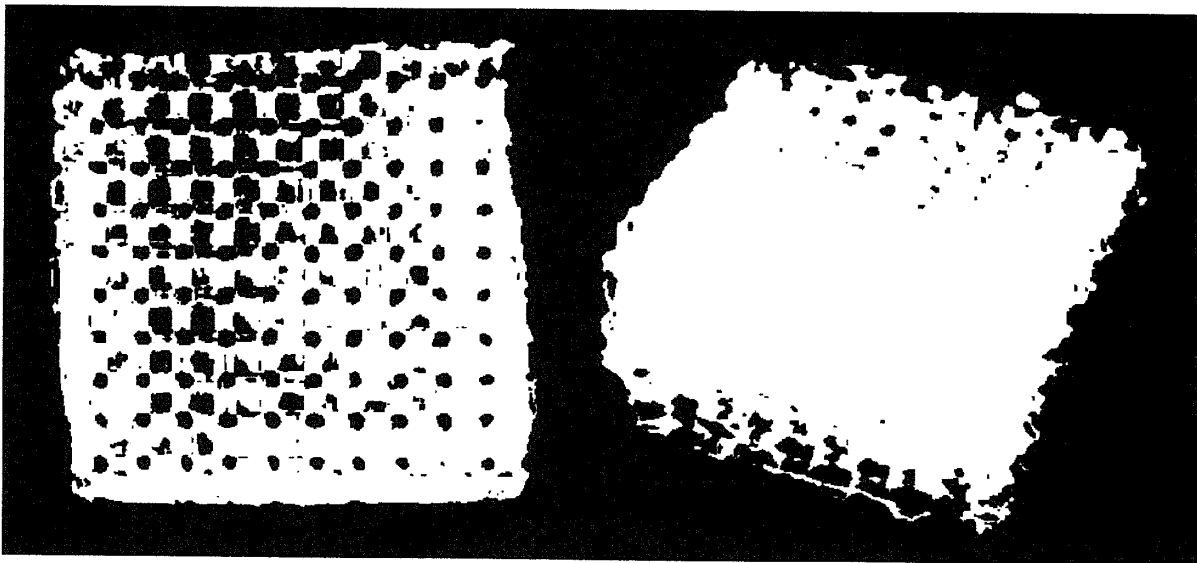


Figure 20. Biodegradable Material CSLG Deposited in a Honeycomb Structure to Allow Infiltration by Living Cells While in a Submerged Cell Culture

## CARDIOVASCULAR BIOMATERIALS

Biomaterials are often made into medical devices rather than being sold in raw form. Among the largest and most demanding of all biomaterial applications are devices that come into direct contact with blood. In general, various derivatives of Teflon and silicone are the most widely used for blood contact, while metals and ceramics are more often used in tissues.

Cardiovascular (heart and blood vessel) applications are one of the most important categories of implant biomaterials. Biomaterials for cardiovascular applications are usually prepared using polymers, because polymers are available in a wide variety of compositions with adequate physical and mechanical properties and can easily be manufactured into products with the desired shape. In addition, some metals and ceramics are used in the blood stream. Figure 21 lists some of the common cardiovascular devices and how long they are in contact with blood.

<b>Medical Devices Used in the Bloodstream</b>
--

	<u>Blood contact time</u>
<b>Catheters</b>	<b>Min-days</b>
<b>Guidewires</b>	<b>Min-hrs</b>
<b>Sensors</b>	<b>Min-months</b>
<b>Pacemaker</b>	<b>10 yrs</b>
<b>Vascular Graft</b>	<b>lifetime</b>
<b>Heart Valve</b>	<b>lifetime</b>
<b>Stent</b>	<b>lifetime</b>
<b>Extracorporeal Oxygenation</b>	<b>hrs</b>
<b>Artificial Kidney (hemodialyzer)</b>	<b>hrs</b>
<b>Total Artificial Heart</b>	<b>10 yrs</b>
<b>Left Ventricular Assist Device (LVAD)</b>	<b>Days-yrs</b>

**Figure 21. Some of the More Popular Biomedical Devices and Duration of Their Blood Contact**

Biomaterials are used as vascular grafts for artery replacements in which they are connected (grafted) onto natural blood vessels at both ends. When arteries, particularly the coronary arteries and the vessels of the lower limbs, become blocked by fatty deposits (atherosclerosis), segments in some cases can be replaced with grafts. Figure 22 shows commercial vascular grafts made by Gore Medical (Flagstaff, Arizona, USA).

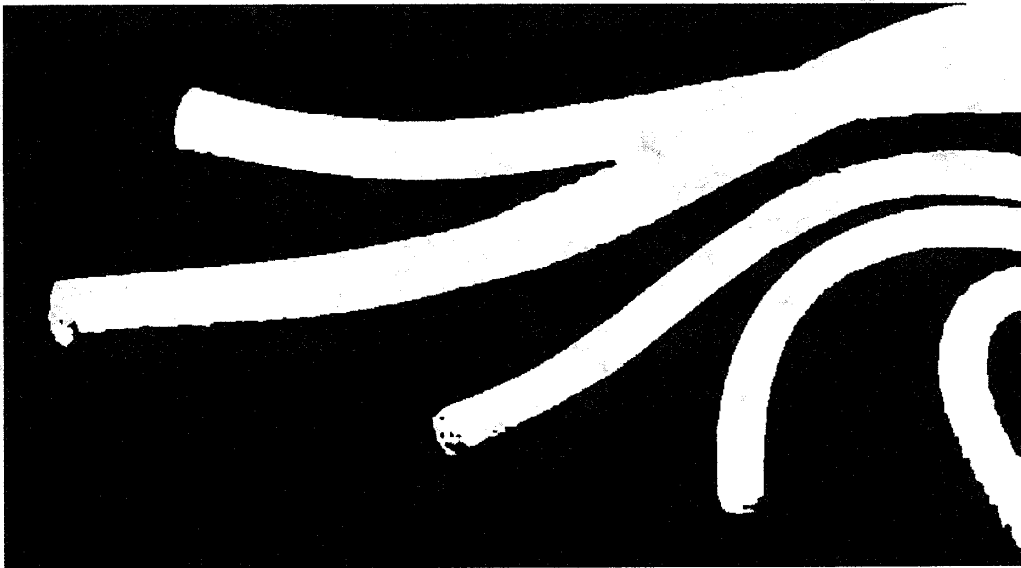


**Figure 22. Gore Medical Teflon Foam Used in Vascular Grafts.** These are artificial blood vessels used to replace blood vessels in the human body damaged by accident, atherothrosclerosis, or diabetic vascular disease.

A problem most materials cause when in blood contact is that they trigger the rapid formation of thrombus (an aggregation of blood cells). The formation of a thrombus is dangerous, as the thrombus could either adhere to the surface of the biomaterial or be detached. If a thrombus is detached, it can travel in the blood stream and occlude smaller vessels in the brain (called a stroke) or lungs (called an embolism). Some small-diameter vascular grafts (< 5-millimeter internal diameter) and prostheses for reconstruction of diseased veins are "safe" only when anticoagulant drugs are used.

In addition to thrombus formation, biomaterials can become colonized with infection-causing bacteria. Some microorganisms found in hospitals are extremely resistant to antibiotic therapy, and infections cannot be fully resolved until the biomaterial is removed. This is particularly a problem with hip and knee implants, where there is poor blood flow near the joint and the body's immune system has limited access. Methicillin-resistant staphylococcus aureus infections are dangerous in these situations.

The high tolerance of the body for woven and formed Teflon allows it to be used as a flexible patch material for other blood-contacting surfaces, in addition to blood vessels. For example, Gore, Inc., makes a Teflon-based material that is used to patch holes in the heart of infants born with atrial septal defects. Figure 23 is an artist's conception of how the patch is inserted into the hole in the atrial wall using a catheter.



**Figure 23. Illustration of Treatment of an Atrial Septal Defect Using a Teflon-Based Product Manufactured by Gore, Inc.**

Heart valves are another application of biomaterials in which the materials are in direct contact with blood. They are typically constructed using a form of stainless steel and woven Teflon (or Dacron) as a suture ring to anchor the device. Figure 24 shows one of these devices.

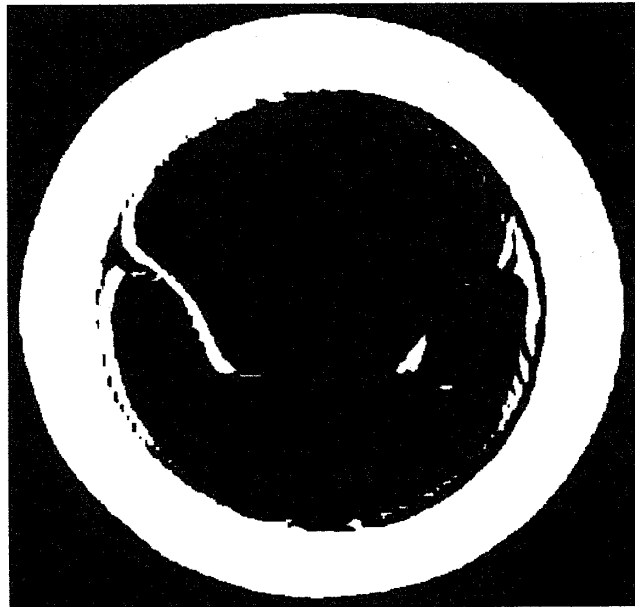


Figure 24. Stainless Steel and Teflon Bjork Shiley Heart Valve

### STENT BIOMATERIALS

A stent is a metal mesh tube that looks something like a Chinese finger puzzle and is used to prop open a clogged artery. These are delivered to the heart in a catheter on the end of a wire usually inserted into an artery in the groin.

The stent is collapsed to a small diameter and placed over a balloon catheter. It is then surgically moved into the area of the blockage. When the balloon is inflated, the stent expands, locks into place, and forms a scaffold that holds the artery open. Figure 25 shows an artist's conception of this process.

The stent stays in the artery permanently, holds it open, improves blood flow to the heart muscle, and relieves symptoms (usually chest pain). Within a few weeks after the stent was placed, the inside lining of the artery (the endothelium) grows over the metal surface of the stent.

Stents are often made from a form of stainless steel that is ductile enough to be expanded by a balloon and then resist closure forces of the vessel wall after the balloon is removed.

The insertion and use of the balloon to expand the stent involves some hazards that can be overcome if the stent is made from a self-expanding metal called Nitinol™. With a nitinol stent, the stent is placed into the body collapsed while it is held cold by a flow of refrigerated saline through the catheter. When allowed to heat up to body temperature by shutting off the cold water to the catheter, the stent expands and more reproducibly applies a calibrated amount of pressure to the blood vessel walls.

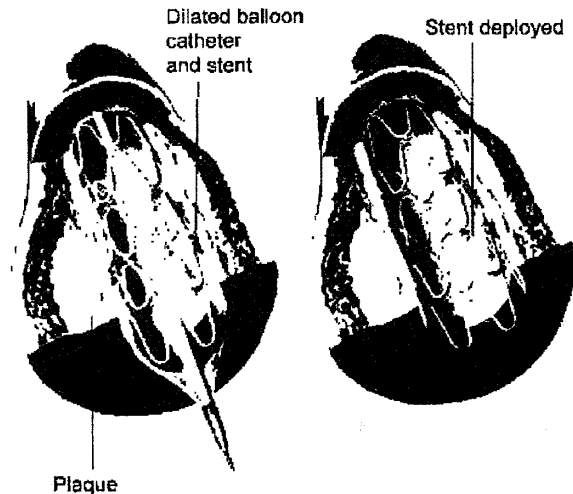


Figure 25. Illustration of Stent Placement. The stent is used to expand the luminal opening of a clogged blood vessel.

## NITINOL AS A BIOMATERIAL

The use of nitinol metal in stents is a clever application of the properties of a class of materials called shape memory alloys (SMAs). SMAs are mixtures of metals that, after being stress treated, can be deformed significantly but then triggered to return to their original shape.

SMAs have a rather remarkable property: they remember their shape. This "smart" property is the result of the substance's ability to undergo a phase change. This occurs at the atomic level, where atoms in the solid subtly shift their positions in response to a stimulus, such as a change in temperature or the application of mechanical stress.

Once the metal is formed at a high temperature it remembers this shape. Subsequent distortions of the material when it is cold remain locked in place while the material remains at a low temperature. However, warming the material to a specific temperature that is relatively closer to its formation temperature will trigger a return to its original formed shape.

In stents, the web is collapsed while it is cold for easy insertion into a blood vessel and held cold by a flow of cold saline out of the catheter. When the stent warms up as the catheter is removed, it expands itself and the surrounding blood vessel. Figure 26 shows a Nitinol stent.

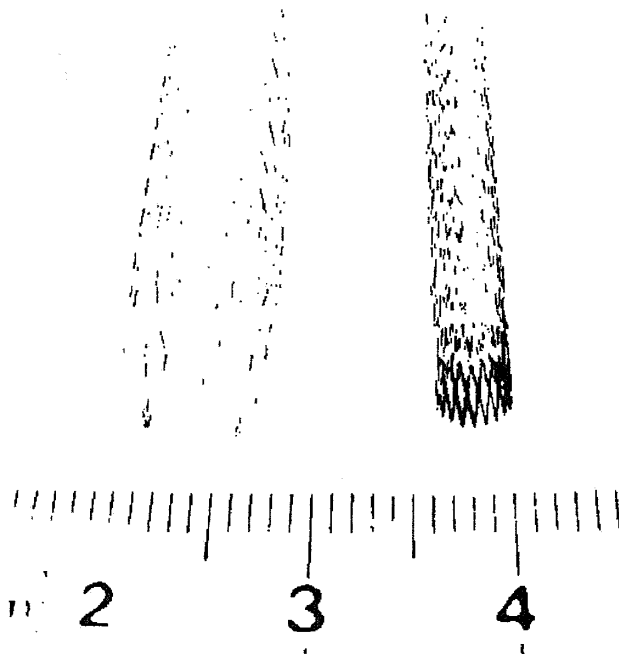


**Figure 26. Nitinol Stent.** Nitinol is an alloy of titanium. It is biocompatible and also a shape memory material.

## CONTACT LENSES

Contact lenses are used to correct vision in the same way as worn glasses but are lightweight and virtually invisible. Their practicality and popularity ultimately depend on the biomaterials of which they are made.

Modern soft contact lenses were invented by Czech chemist Otto Wichterle and his assistant, Drahoslav Lím who also invented the first gel used for their production. However, it was not until the employment of poly-methyl-methacrylate, known as PMMA (a cousin of acrylic plastics, such as Plexiglas™), that they began to enjoy mass appeal. Figure 27 shows a gas-permeable contact lens.

PMMA, however, is not an ideal contact lens material since no oxygen is transmitted through the lens to the conjunctiva and cornea. This can cause a number of adverse clinical effects. To solve this problem, a range of oxygen-permeable but rigid materials were developed. These materials, referred to as "rigid gas-permeable" or "RGP" materials or lenses, were made by synthetically adding dimethylsiloxane (a form of silicone) to acrylate plastics. Silicones have a very high level of oxygen transport, and amalgamating them with plastics adds this quality, while the acrylics provide strength and hardness. The easy diffusion of oxygen across silicones is thought to be a result of an intermediate solubility of oxygen in the gas phase with the gel phase of silicone.

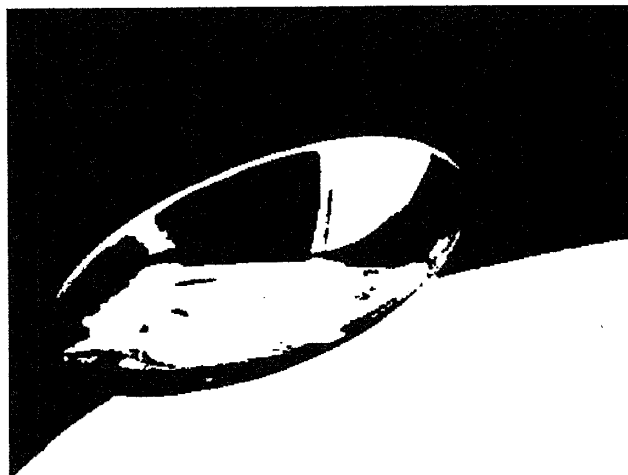


**Figure 25. Contact Lens.** Modern contact lenses are made of a mixture of acrylics and silicones that readily pass oxygen to the cornea.

Occasionally, the term "gas permeable" is used to describe RGP lenses, but this is potentially misleading, as soft lenses are also gas permeable in that they allow oxygen to move through the lens to the ocular surface.

In 1999, first silicone hydrogels were launched on the contact lens market. These new materials had the advantage of high oxygen permeability, with the comfort and clinical performance of the conventional hydrogels that had been used for the previous 30 years. These lenses were initially advocated primarily for extended (overnight) wear, although more recently, daily (no overnight) wear silicone hydrogel contact lenses have been launched.

## **DRUG DELIVERY POLYMERS**

One area of biomaterials research is the use of biodegradable materials in the design of systems for controlled drug delivery. Much of this work is driven by the need for the slow release of insulin for the control of brittle diabetes. Mechanical insulin delivery pumps are moderately successful but usually are worn on the outside of the body and are cumbersome.

The ability to introduce insulin and other drugs in a controlled-release manner using biopolymers has clear advantages in terms of user convenience. Similarly, the slow release of other drugs, such as chemotherapeutic agents, is necessary to maintain the drug in the desired therapeutic range with just a single dose.

The basic strategy with some of these systems is to encapsulate drugs in membranes, capsules, microcapsules, liposomes, and hollow fibers. Another approach is to disperse

the active agent in a biodegradable polymer, as shown in Figure 28. The polymer host to the drug dissolves, releasing the drug in a controlled manner over time.

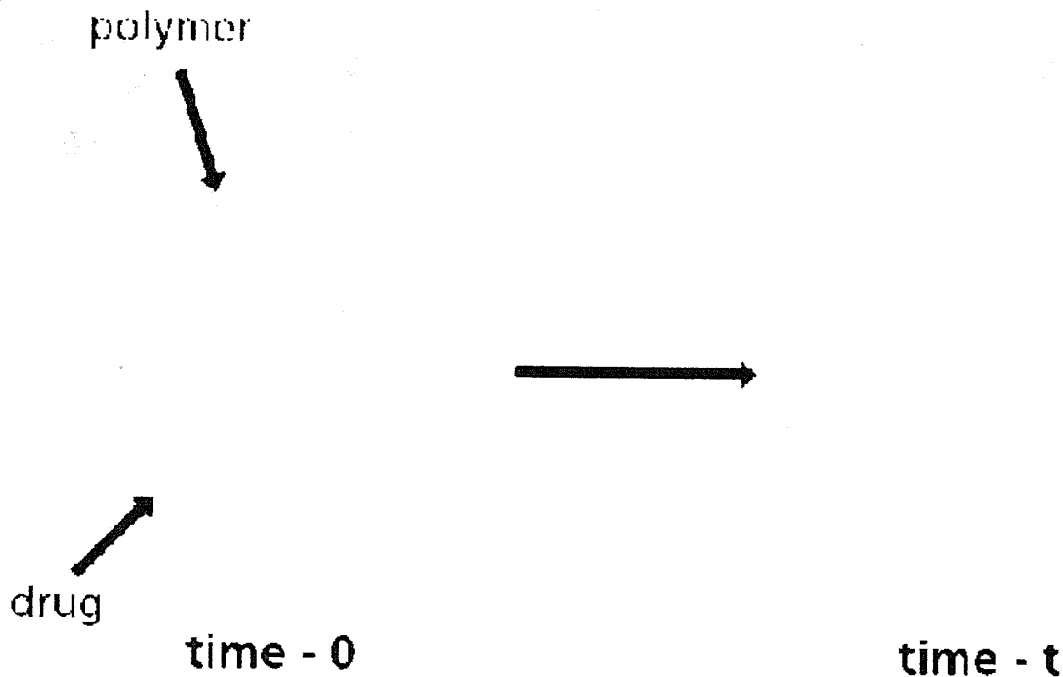


Figure 26. Schematic Representation of Biodegradable (Bioerodible) Drug Delivery Device

The use of biodegradable materials allows the drug to be introduced without much concern for the build-up of the polymer carrier. The carrier is eventually absorbed by the body and, thus, need not be removed surgically.

Drug diffusion through the polymer matrix can also determine the drug dosage rate without actual loss of the polymer. This rate is determined by the choice of polymer, the size of its pores, and the rate at which the drug diffuses from the pores.

The three key advantages polymeric drug delivery products can offer are:

- **Localized Delivery of Drugs:** The polymer-drug combination can be implanted directly at the site where drug action is needed and, hence, whole-body exposure of the drug can be reduced. This becomes especially important for toxic drugs, such as the chemotherapeutic drugs.
- **Sustained Delivery of Drugs:** Once injected, the encapsulated drug is released over extended periods, thereby eliminating the need for multiple injections. This feature can improve patient compliance, especially with drugs for chronic indications that require frequent injections (such as for deficiency of certain proteins).
- **Stabilization of the Drug:** The polymer can protect the drug from the physiological environment and hence improve its stability in vivo. This particular feature makes this technology attractive for the delivery of labile drugs, such as proteins.



An appropriate selection of the polymer matrix is necessary in order to develop a successful drug delivery system. The most commonly used polymers for this application, polylactide (PLA) and poly(lactide-co-glycolide) (PLGA), have been used in biomedical applications for more than 20 years and are known to be biodegradable, biocompatible, and nontoxic. A vast amount of literature is available on the characterization of these polymers and their biodegradation and drug-release properties.

### **MEDICAL TITANIUM AS A BIOMATERIAL**

Titanium metal has qualities of strength, inertness, and a biological compatibility that make it desirable as a biomaterial. Essentially all pacemakers, neurostimulators, and various other implanted medical devices use titanium as a packaging case material.

Titanium metal exposed briefly to the atmosphere oxidizes to form a microscopically thin layer of titania (titanium oxide). Titania is a hard, adherent, and inert ceramic-like compound and is thought to be largely responsible for titanium's acceptability in biomedical applications where metal corrosion in warm, salty body fluids ordinarily would be a problem.

Titanium is used for its high strength in replacement hip and knee joints. In these cases, it is important how the metal integrates with living tissue and bone because load must be transferred from the metal to the bone. Titanium generally does exceedingly well and is used as the metal of choice in nearly all biomedical applications where high strength and impact resistance is important.

Titanium has a particular ability among the various metals that might otherwise be chosen in that it can integrate itself well with living bone. The recognition of this dates back to 1952, when Swedish Professor Per-Ingvar Brånemark conducted an experiment in which he studied blood flow in living rabbit bone. The bone was fixed in a roughly machined titanium holder. At the conclusion of the experiment, after many days, he found that the bone had integrated so completely with the titanium that removing it was impossible. He called this osseointegration and saw the possibilities for human use.

Figure 29 shows a photomicrograph of a titanium-bone interface. The close approximation of the titanium (black) to the tissue is an indicator of a close-metal-tissue integration. Osseointegration was first implemented in dentistry to fixate teeth. It is now also used for head and jaw reconstruction.

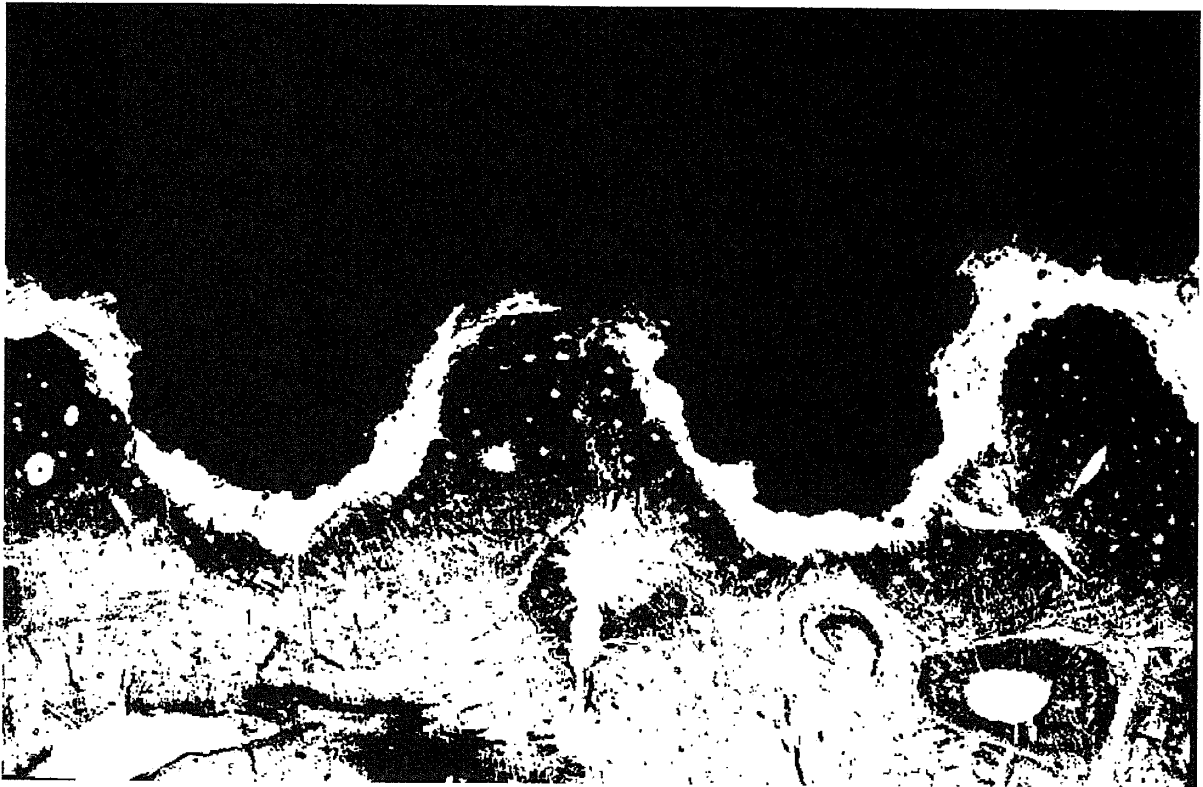


**Figure 27. Photomicrograph of Titanium Metal (Appears Black in This Photo) in an Intimate Integration With Living Bone.** The intersection of the two materials shows a thin barrier layer and then healthy tissue very close to the metal. It does not show inflammation or scar tissue formation.

Optimization of the bone integration with titanium has been much studied over the years. It has been found that if single cells can nestle into pores on the metal surface and then can reach out and attach to their neighbors, this forms a particularly good adhesive interface. This observation has led to new types of surface treatments for titanium to improve its ability to attach to bone. The need for a particular porosity size scale for optimal bone integration has only recently been recognized.

Sand blasting of the titanium surface has long been done, but, recently, plasma etching and pitting with the use of acids have been found effective. Some of the more recent (2008) innovations have been the use of lasers to create a surface modification by melting pits.

Another good approach is to coat metal implants with bioactive materials, such as hydroxyapatite (HA). HA has excellent biocompatibility, bioactivity, and bone-binding properties. It forms a bond with titania thin films on the surface of titanium implants and so prepares the surface for adhesion. Researchers recently determined that making this layer thick (about 1 micron) encourages cell proliferation and bonding.

Recent improvements in HA have included manufacturing it in the form of a spherical nanopowder that is more acceptable to tissues than are spicule forms of its natural occurrence. Using HA in the form of a nanopowder stimulates bone formation leading to a natural, as well as chemical, adhesion, much like glue.

Another recent discovery is that treating the titanium surface with a silane compound will create a surface chemistry that attracts certain biomaterials known as proteoglycans. From this point, it is possible to lay down layers of collagen on the surface from which connective tissues will form.

Titanium metal used for implants is usually a biomedical alloy, Ti-6Al-4V, since biomedical alloys provide good corrosion resistance and reasonable fatigue life and are much stiffer than cortical bone. The Ti-6Al-4V alloy is more suitable than is the Co-Cr alloy for coating with HA because it has less potential proximal stress shielding and bone resorption.

### **BIOMATERIALS IN DIALYSIS**

Medical therapeutic dialysis, often called hemodialysis, is a method of removing uric acid and other waste products from blood, a necessity when the kidneys fail. It is also useful in removing exogenous poisons like ethanol, aspirin, barbiturates, and boric acid from the blood in cases of poisoning.

Hemodialysis accesses the blood stream through the use of two large needles—one in an artery and one in a vein—in order to flow a patient's blood through a series of hair-thin, hollow-membrane, tube-like fibers.

A dialyzer is composed of thousands of tube-like hollow fiber strands encased in a clear plastic cylinder several inches in diameter. Blood flows on the inside of the membrane fiber, and a dialysate (extraction stream) flows across the outside. Low-molecular-weight waste products pass out through the membrane, while blood cells and other large molecules in the blood are retained. Figure 30 shows an illustration (left) and photograph (right) of dialyzers used to treat kidney failure.

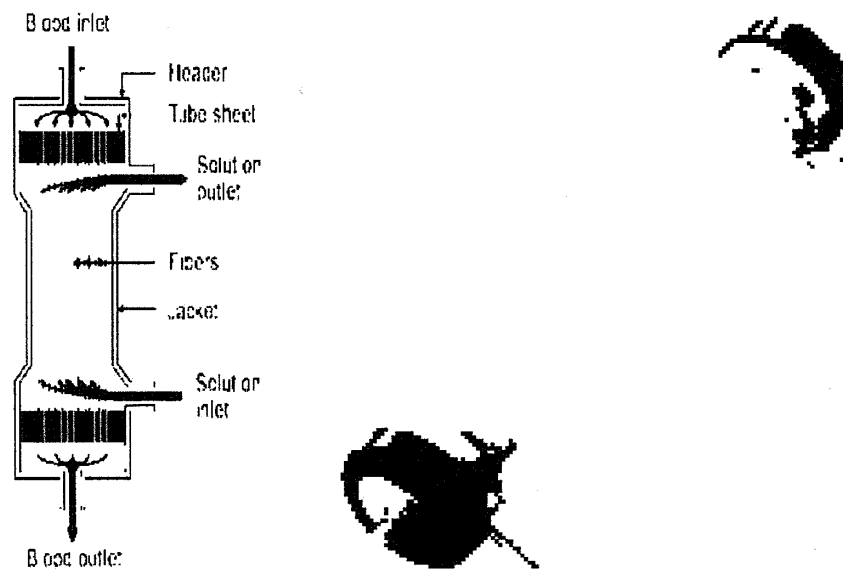


**Figure 28. Illustration (Left) and Photograph (Right) of a Blood Dialyzer as Used in Medicine**

Dialysis works on the principles of natural diffusion of metabolic waste products in the blood across a semipermeable membrane. Waste products in high concentration in the blood will diffuse across the membrane. The membrane allows the passage of certain-sized molecules across it but prevents the passage of other, larger molecules of the blood, thus helping to get rid of waste products. Figure 31 illustrates this idea. The blood cells are kept on the outside of the membrane (orange) while waste product solutes (violet and yellow dots) pass through.



**Figure 29. Cuprophane Membrane Passes Blood Waste Products (Violet and Orange Dots) Through Pores and Blocks Passage of Red Blood Cells**

Advances in bioengineering and in the technical aspects of dialysis machines have made hemodialysis a safe and effective procedure.

The design of dialyzers is primarily an exercise in biomaterial selection. Biomembrane materials play the critical role in cleansing the blood, but they must not damage the blood or provoke thrombus. The most common biomaterial used in dialyzers is a semipermeable membrane made of cellulose acetate trade-named Cuprophane™.

Dialyzer membranes come with different pore sizes. Nanotechnology is being used in some of the most recent high-flux membranes to create a uniform pore size. The goal of high-flux membranes is to pass relatively large molecules, such as beta-2-microglobulin (MW 11,600 daltons), but not albumin (MW ~ 66,400 daltons). Dialysis membrane materials are crucial to the practical performance of medical hemodialysis systems. These systems/materials support the survival of millions of people in kidney failure that undergo routine dialysis, usually for several hours during the day and three to four times a week.

## Summary and Recommendations

The performance of biomaterials underlies the success of many medical devices that must be acceptable to body tissues. These materials often serve critical—perhaps life-and-death—functions and, so, require large amounts of money and time to rigorously test. This appears to be the reason the biomedical industry is slow to produce and accept new materials.

Existing materials for implants are generally based on materials that have been available for more than 20 years. Biodegradable materials, particularly the polylactide and glycolide, have a long history of safe and effective use. Building on this solid foundation, most of the innovation is occurring in devising new ways to embody the materials and apply them to new applications. Thus, the markets are expanding for biomaterials, and physicians can look forward to new products that will help speed patient recovery.

~~UNCLASSIFIED//FOR OFFICIAL USE ONLY~~



# Defense Intelligence Reference Document

*Acquisition Threat Support*

12 January 2010

ICOD: 1 December 2009

DIA-08-0912-008

## Materials for Advanced Aerospace Platforms

~~UNCLASSIFIED//FOR OFFICIAL USE ONLY~~

## **Materials for Advanced Aerospace Platforms**

**Prepared by:**

(b)(3):10 USC 424

**Defense Intelligence Agency**

**Author:**

(b)(6)

**Administrative Note**

COPYRIGHT WARNING: Further dissemination of the photographs in this publication is not authorized.

This product is one in a series of advanced technology reports produced in FY 2009 under the Defense Intelligence Agency, (b)(3):10 USC 424 Advanced Aerospace Weapon System Applications (AAWSA) Program. Comments or questions pertaining to this document should be addressed to (b)(3):10 USC 424;(b)(6), AAWSA Program Manager, Defense Intelligence Agency, ATTN: (b)(3):10 USC 424 Bldg 6000, Washington, DC 20340-5100.

## Contents

Introduction.....	iv
Launch Vehicles .....	1
Reusable Crew Modules.....	9
Reusable Single-Stage-to-Orbit Vehicles .....	10
Advanced Al Alloys .....	11
Polymer Matrix Composites.....	11
Al Matrix Composites.....	12
Ti Alloys .....	12
Ti Matrix Composites.....	14
Ni-base Alloys .....	16
Refractory Metal Alloys .....	18
Ceramic Matrix Composites .....	18
Carbon-Carbon Composites .....	19
Titanium Aluminides .....	20
Propulsion Systems.....	21
Summary and Recommendations .....	22

## Figures

1. Schematic Diagram of Friction Stir Welding .....	2
2. Specially Modified 747 Transporter Unloading a Boeing 787 Composite Fuselage Barrel Section .....	4
3. Micrograph Showing Phase Formation at the Surface of a Ti Alloy That has Been Exposed to Air at Elevated Temperature .....	13
4. Cross-Section Micrograph of a Ti Matrix Composite.....	15

## Tables

1. Potential Materials by Use Temperature Regime and Property .....	10
2. Example of Properties of Ti Matrix Composites .....	14

## Materials for Advanced Aerospace Platforms

### Introduction

"Advanced aerospace platforms" is a broad topic that can be divided into several narrower subtopics to enable a more concise discussion of materials advances, challenges, and opportunities. Consequently, this document discusses the areas of launch vehicles, space vehicles, and space propulsion systems separately because their key requirements are often application specific, which affects materials selection decisions. In addition, single-use and reusable boosters have different durability requirements that directly impinge on design and materials selection. Furthermore, current engineering practice has evolved to the point that design synthesis must integrate the structure and construction materials to achieve optimum product performance. For example, the space shuttle was designed to meet customer-imposed mission requirements (range, payload, empty weight, landing capability, and so forth) without significant real-time consideration of materials capability. This approach led to significant compromises at later stages in the shuttle's development and maturation. (Arguably, the shuttle could be designed as a more efficient vehicle today.) In the extreme, a spectacular engineering failure was the National Aerospace Plane (also dubbed the Orient Express), which was launched as a military project and was intended to be a mach 12 reusable strike vehicle. This project rapidly became materials limited and was canceled in 1993, after about \$750 million in federal R&D expenditures and a substantial private sector investment. The point is that any "clean sheet of paper design" must start with an assessment of the requirements for construction materials and be accompanied by a realistic assessment of the capability of currently available materials to meet these needs. If these two assessments indicate a gap between requirements and existing materials capability, a risk assessment and a risk-mitigation plan must be developed before expending engineering hours and funds.

Since the inception of manned space flight, the approach to design has changed to include the concept of damage tolerance. This shift in design philosophy was prompted by the (eventual) recognition that complex structures cannot be designed and produced with zero defects. With the maturation of fracture mechanics and means of reducing these concepts to practice, the transition from zero defects to defect tolerance became the norm. This new approach in turn led to recognition that high-performance materials required not only high specific strength and stiffness but pacing increases in strength with simultaneous improvements in fracture toughness and fatigue crack growth resistance. The introduction of damage tolerance was accompanied by a renewed emphasis on nondestructive inspection capabilities. This latter thrust was driven by the need to demonstrate the capability to reproducibly locate small flaws that could become failure initiation sites, either because of static or because of cyclic loading conditions. In the case of atmospheric flight, the U.S. Air Force has introduced standards for airframes (the Aircraft Structural Integrity Program) and propulsion systems (the Engine Structural Integrity Program) that tie structural life and reliability to



**UNCLASSIFIED//~~FOR OFFICIAL USE ONLY~~**

**this demonstrated inspections capability. Implementation of these standards, starting with the B-1 bomber and the F-100 and F-110 engines, has dramatically reduced (but not eliminated) the incidence of catastrophic failures of critical components that endanger crews, vehicles, or both.**

**Taking these changes into account, this document outlines the current situation regarding the design and production of high-performance structures for aerospace platforms, including launch vehicles, space vehicles, and propulsion systems for transporting space vehicles (and payloads) into orbit.**

**UNCLASSIFIED//~~FOR OFFICIAL USE ONLY~~**

## Materials for Advanced Aerospace Platforms

### LAUNCH VEHICLES

For the purposes of this document, launch vehicles are defined as the structure that supports and/or encloses the propulsion system, the fuel supply, and the crew or payload module. Launch vehicles today are either single use or multiple use after recovery and extensive refurbishment. This approach adds considerably to the cost of transporting a pound of payload into earth orbit, regardless of whether an unmanned satellite or a manned orbiting crew module that must withstand the temperatures and loads associated with safe reentry to earth. Furthermore, the larger the payloads are, the greater are the reaction forces the launch vehicle must withstand during launch. With the total weight of the payload, the empty weight of the launch vehicle, and fuel all needing to be lifted initially, fuel-efficient propulsion and lightweight launch vehicles are essential to maximizing the payload. Except in the area around the propulsion system exhaust, the temperatures experienced by launch vehicles during launch are not demanding. Therefore, advanced, high-strength aluminum (Al) alloys and polymer matrix carbon fiber composites (PMCs) are prime candidates for the parts of the structure that experience aerodynamic loads and where aerodynamic heating does not exceed about 125 °Celsius. One class of advanced Al alloys is the lithium (Li)-bearing alloys, such as Al alloy 2090. This alloy contains enough Li to reduce its density by 8 percent while increasing the elastic modulus (E) by 10 percent. Other, newer advanced Al alloys, such as 7050 and 2050, have been developed to have improved damage tolerance. These alloys have excellent specific strength at or near room temperature and experience no major loss of ductility at cryogenic temperatures. The newer variants of the 2000 and 7000 Al alloys also have substantially improved resistance to most types of corrosion, including exfoliation and stress corrosion cracking. This can be important in a reusable vehicle.

Perhaps the most important aspect of the improved Al alloys is their higher fracture toughness, accomplished through a combination of alloy composition control and improved processing. In alloy composition control, the concentrations of the residual elements iron (Fe), chromium (Cr), manganese (Mn), and silicon (Si) are reduced at the ingot stage. These elements combine with Al to form hard, brittle intermetallic compounds known as constituent phases. The advanced alloys contain fewer, smaller constituent phases, leading to improved fracture resistance and higher fracture toughness values. In applications such as body skins for commercial aircraft, this improved toughness has enabled an increase in the spacing of the circumferential fuselage frames, or "hat sections," that serve both as stiffeners and as crack stoppers to prevent a catastrophic failure during pressurization. For any given operating stress—in this case the pressurization stress—the spacing of the frames is directly related to the critical crack size of the body skin. Higher toughness alloys have larger critical crack sizes, and the frames can be spaced further apart without increasing the risk of catastrophic failure. The increased spacing ultimately allows a fuselage design that requires fewer frames. Consequently, the airplane benefits from a commensurate reduction both in weight and in manufacturing cost. Similar possibilities exist for the design of a fail-safe launch vehicle that has a lower empty weight. Clearly, the advanced Al alloys offer intrinsic improvements over the alloys used in the Saturn launch vehicle and introduce the prospect of new, more efficient launch vehicle designs.

The newer Al alloys also can be specially processed to render them superplastically formable. This capability opens a realm of possibilities to replace structures that, in the absence of this capability, are machined from thick plate. Very large structures are produced in sections that must be joined. Conventional fusion welding techniques do not work for high-strength Al alloys such as 7075, 7050, 2024, or 2050 because either the welds lead to cracks or the welds made under conditions that avoid cracking have greatly reduced tensile properties. Because these alloys are not amenable to welding, heavier, fatigue-prone mechanically fastened joints must be used. Recently, scientists developed a joining process that permits joining of Al alloys such as 7050. This process, called friction stir welding (FSW), allows joint designs in a variety of configurations that were not considered possible when fusion welding was the only alternative.

In FSW, a rotating steel tool is inserted into the seam between the two Al alloy pieces to be joined. As the rotating tool is driven forward, the friction between the tool and the work piece generates enough heat to soften the Al alloy without melting it. A schematic of this process is shown in Figure 1.

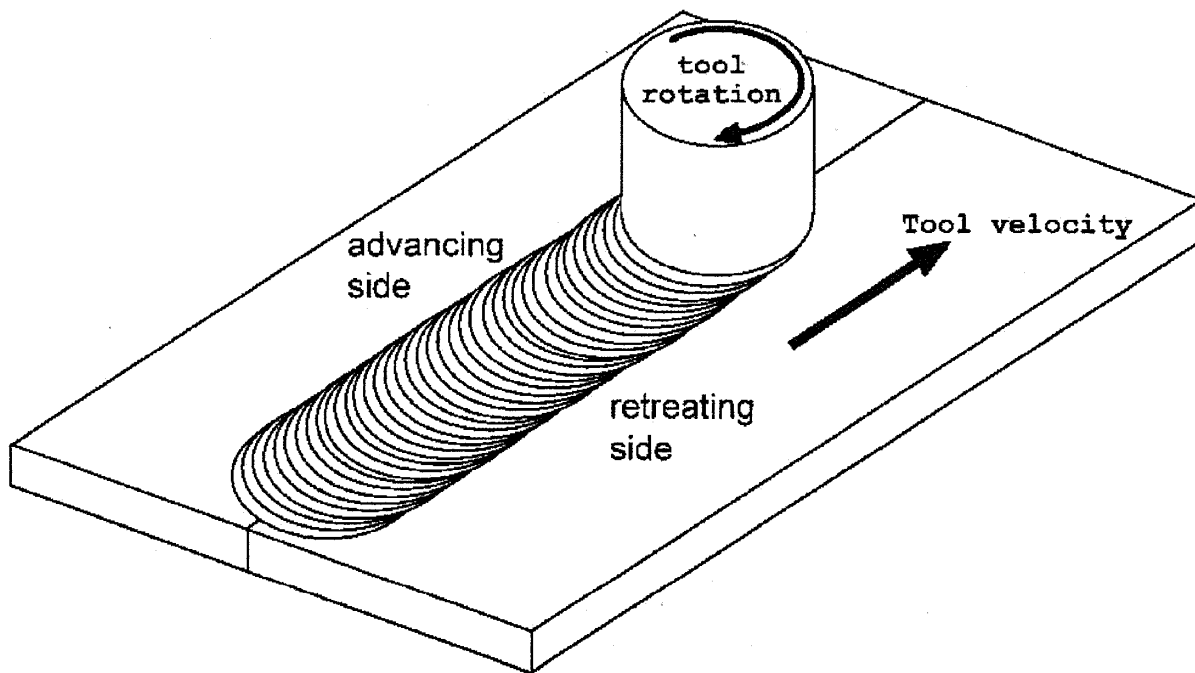


Figure 1. Schematic Diagram of Friction Stir Welding

The combined action of the rotation and the traversing of the tool essentially kneads the two pieces together, leaving a mechanically sound joint. Although the weld properties may be somewhat inferior to those of the base metal, they are good enough that a relatively small increase in thickness at the joint position can compensate. Although substantial development of the FSW process is ongoing, FSW already has been put into practice. For example, the current external propellant tank on the space shuttle is made from an Al-Li alloy fabricated through FSW. The weight advantage of using welded as opposed to bolted joints in a large structure such as a launch vehicle is considerable. With earlier high-strength alloys such as 7075, concerns about fracture toughness in conjunction with monolithic structures would have caused a welded

construction to be considered too risky. Today, the combination of higher toughness alloys and FSW opens up the possibility of greater design flexibility resulting in lighter large structures with equal or greater reliability than earlier ones.

In sum, metallic, nonreusable (at least nominally so) launch vehicles made from advanced Al alloys and fabricated through FSW constitute an incremental but significant improvement over earlier versions.

In recent years, PMCs have matured significantly. For many components that are not exposed to elevated temperatures, PMCs provide a degree of design flexibility not readily available in metals. Consequently, PMC materials have begun to supplant Al alloys in the construction of commercial subsonic aircraft. The use of PMCs in the empennage of the Boeing 777 was one of the first examples of Al alloys being displaced. Subsequently, the new Boeing 787 has more structure made from composites than from metallic materials. Once PMCs are introduced into a structure in significant quantities, a constraint related to galvanic incompatibility between the PMC structure and any adjoining Al alloys also is introduced. When a PMC structure is in direct contact with an Al alloy structure, catastrophic corrosion of the Al alloy components can occur. In the Boeing 787, the remedy for this concern is the use of titanium (Ti) alloys in areas where there is direct contact between the metallic and the PMC structures. This is directly analogous to the plastic bushing a plumber puts in the joint between copper and iron piping. Notwithstanding this constraint, the specific strength and stiffness of PMC structures make a compelling argument for their application in high-performance structures, such as launch vehicles.

Composite structures can be manufactured using one of three methods: hand layup of pre-preg, automated tow placement, and resin transfer molding.

- The most rudimentary of these, but also the most flexible, is hand layup of pre-preg. This method uses sheets of material that contain both the fiber and the polymeric matrix (called pre-preg). The polymeric matrix can be either a thermoset (for example, epoxy) or a thermoplastic. Individual plies are cut from the pre-preg typically using a numerically controlled laser or mechanical cutting device and are laid up to form the desired shape. Areas that have heavier loads contain more plies locally, and the plies are cut in an orientation with respect to the fiber direction in the pre-preg to achieve the desired strength relative to the principal load path. These plies are carefully placed according to a drawing (blueprint), making hand layup a labor-intensive process and, therefore, making parts made using this method expensive. During ply placement, it is critical that no ply wrinkles are introduced, as these create severe reductions in the local load-bearing capability of the final component. Once all the plies are in their proper places, the article is placed in a vacuum-tight bag that is evacuated and placed in an autoclave for curing of the epoxy matrix or fusing of the thermoplastic. A disadvantage of a pre-preg whose matrix is a thermoset is limited shelf life. In practice, this is managed to a degree by storing the pre-preg in a freezer to slow the rate of chemical reaction that sets the epoxy. However, this does not completely halt the reaction, causing these materials to have a shelf life beyond which they are not easily manipulated during layup and do not develop full strength after curing in the autoclave. An additional issue is out time—the time the pre-preg can be out of the freezer during layup before the reaction proceeds at an accelerated rate and reaches a point at which the

material is not suitable for the reasons stated earlier. Clearly, the time required for layup places practical limitations on component size.

- In automated tow placement, thin ribbons of a pre-preg are fed off a drum or rolled into a computer numerically controlled machine that places them in the desired position. In principle, this process trades recurring labor cost for up-front capital investment (the tow placement machine) and programming time. If the anticipated volume of identical parts is high enough to amortize the capital investment and, particularly, the programming cost, this can be an attractive means of reducing manufacturing costs. For axisymmetric shapes, such as cylinders, this essentially becomes a winding process and is quite efficient. An example of a finished composite fuselage barrel section for the Boeing 787 is shown in Figure 2. For more irregular three-dimensional shapes, such as a spar or a strut, placing the tows becomes much more difficult and presents a fundamental limitation. Consequently, PMC structures with complex shapes are still for the most part made using the hand layup process. A variant of automated tow placement is compression, whereby a preform, made by automated tow placement, is forced by a press into a preshaped die. This process allows fabrication of more complex shapes, but the rigidity of the fiber and the extreme anisotropy of the tows can lead to wrinkles, which are not acceptable because of the reductions in properties these cause.

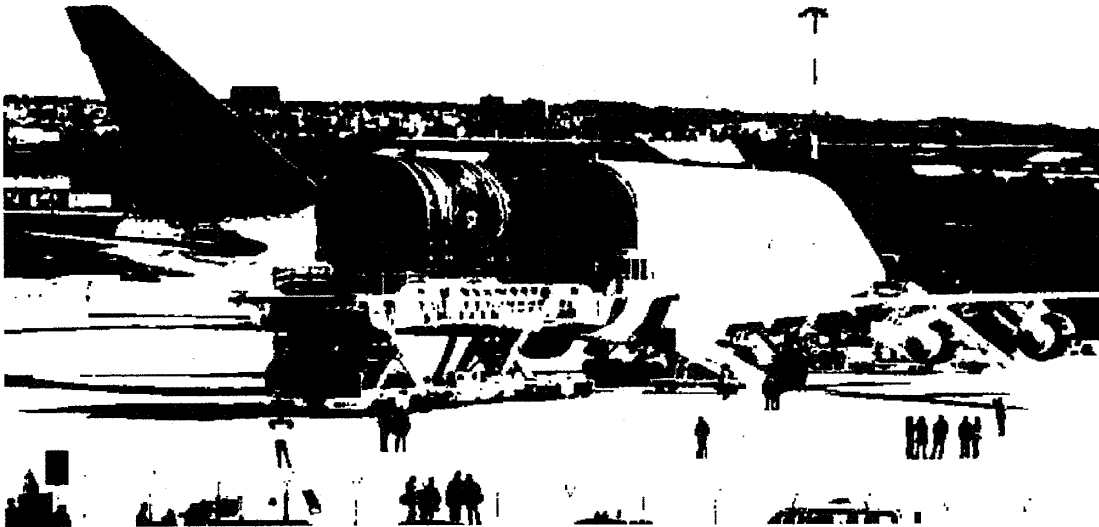


Figure 2. Specially Modified 747 Transporter Unloading a Boeing 787 Composite Fuselage Barrel Section

- The third main composite fabrication method, resin transfer molding (RTM), begins with a woven fiber mat or preform. The polymeric matrix is injected into this mat to create a fully dense composite. The major benefit of RTM is that it permits use of a three-dimensional weave that minimizes the risk of delamination between plies. Note that, with the other two methods, the material is reinforced in only two dimensions (the plane of the pre-preg or tows). RTM's limitations include the viscosity of the resins used. If the resin is too viscous, injecting it will either distort the fiber architecture of the woven preform or not fully penetrate the preform,

leaving voids. This limitation makes it difficult to use many thermoplastic resins that are otherwise attractive because they are recyclable and have much longer shelf lives than thermosets (epoxies). Another, more obvious limitation of RTM is component size. This is in part because weaving of very large fiber preforms is challenging and requires a very large weaving machine. It also requires a large injection machine capable of multiple injection sites to ensure the complete infiltration necessary to avoid formation of voids.

In practice, there are several significant challenges associated with manufacturing large PMC structures today. Among these, perhaps the most significant are manufacturing cost and the difficulty associated with making large, nonaxisymmetric components. Large axisymmetric components that can be produced by winding tows of pre-preg are clearly possible today, as demonstrated by the Boeing 787 fuselage whose section is shown in Figure 2. For other shapes, because the load-bearing capability of PMCs depends on the transfer of externally imposed loads to the strong, stiff fibers, joints that intersect the principal load path become problematic. This is because the fibers and, as a direct consequence, the load path are discontinuous, requiring local section size adjustments to offset this local structural inefficiency. Thus, achieving the most structurally efficient use of PMCs requires monolithic structures with continuous fibers. In large structures, this is at best a challenge. Even in the Boeing 787's PMC fuselage, mechanically fastened joints are used to connect adjacent barrel sections. In the fuselage, as in any cylindrical pressure vessel, the principal stresses are hoop stresses stemming from pressurization during flight. However, the compromise in structural efficiency is minimized by the circumferential orientation of the joints. Although these bolted joints add weight, the overall structural efficiency of the PMC structure is still better, albeit considerably more expensive, than a longitudinally and circumferentially stiffened Al structure. The circumferential joints also create discontinuous longitudinal crack paths that improve the structure's damage tolerance. Some of the added expense of the PMC fuselage stems from the use of Ti alloy fasteners because of the galvanic coupling issues that would accompany Al or steel fasteners.

For other applications, which are limited by different material properties, the PMC system can be tailored to optimize structural performance. This is possible because both the matrix and the fiber can be independently selected. Moreover, the fiber "architecture" (fiber orientation, weave geometry, and fiber volume fraction) can be varied spatially to optimize load-bearing capability under complex stress states. For example, again drawing on recent applications in commercial aircraft, the fan blades of the large, high-bypass-ratio turbofan engine (GE90) produced by General Electric for the Boeing 777 are made from PMCs. The limiting design consideration for these fan blades is resistance to bird strikes. To optimize the PMCs' impact resistance, a medium-modulus, high-tensile-strength carbon fiber was selected in combination with a thermoplastic toughened epoxy matrix. Furthermore, the fiber architecture was set to optimize the bending strength under the impact of a bird. The GE90 fan blades are produced by hand layup and are quite costly to produce. In the 10-plus years that these fan blades have been in service, not a single unscheduled engine removal related to the PMC fan blades has occurred. The competitive fan blade technology for B-777-class engines is hollow Ti, which is used by both Pratt & Whitney and Rolls Royce. By all informal accounts, these blades are cost intensive. This example supports the unwritten rule that the pathways leading to high-performance, high-value structures typically are

not technology dependent but are cost intensive, no matter what technology is employed to meet the requirements.

An additional characteristic of PMC structures—one related to the laminated construction of components made by hand layup or automated tow placement methods—is their susceptibility to formation of delaminations when impacted perpendicular to the plane of the plies. This is due to the mismatch in bending stiffness between adjacent plies that have different unidirectional fiber orientations. This mismatch causes shear stresses to develop that can exceed the shear strength of the interlaminar bonds, causing small, embedded cracks to form. Under subsequent inplane compression loading, the laminates bow because of the Poisson stresses and separate because of the lack of an interlaminar bond to hold them together. In significant compression loads, the laminates buckle, and this leads to structural failure. This phenomenon, called compression after impact, is an insidious failure mode because the delaminations are not externally detectable unless ultrasonic inspection methods are used. Sources of such an impact include dropped tools, foreign objects (for example, meteorites), and, perhaps most commonly, hail storms. Ultrasonic inspection, if required, is expensive and time consuming. The latter concern in turn affects vehicle availability and turnaround time. PMC parts made using RTM typically have reinforcing fibers in the through-thickness direction, so concerns about compression after impact are minimal.

The maximum temperature at which PMCs can be used is limited by PMCs' susceptibility to oxygen degradation of the polymeric matrix. The maximum-use temperature for prolonged exposure is determined by the thermal oxidative stability (TOS) of a particular resin. The TOS, like any chemical reaction, is determined by both time and temperature. The glass transition temperature ( $T_g$ ) of the polymeric matrix also imposes strength and dimensional stability limitations independent of the TOS limits. This is particularly true for thermoplastics. However, the TOS limits usually impose lower temperature limits than  $T_g$  if prolonged thermal exposure is contemplated. Three distinct classes or groups of resins exist, each with a successively higher temperature capability. These are conventional epoxies and most thermal plastics, bismaleimides (BMIs), and linear polyimides. The first class is limited by TOS to about 125° Celsius. BMIs can be used to about 175° Celsius. Linear polyimides, such as the in situ polymerization of monomer reactants (PMR) group of thermosetting formulations, can be used to about 300° Celsius. Many of the PMR resins contain the hazardous compound *methylenedianiline*, which requires special care during use, including protective clothing to limit personnel exposure (for example, during ply cutting and hand layup). This requirement reduces productivity, adds cost, and creates a degree of liability concern for the manufacturer of the PMC components. For RTM, the BMIs and PMR resins typically have higher viscosity and require commensurately higher injection temperatures to reduce the viscosity to manageable levels for reasons discussed earlier. New resins are constantly being developed, including some with attractive properties. However, many of the sources of these resins are startup companies that exist on R&D funding, often in the form of U.S. government SBIR (Small Business Innovative Research) projects. Such companies are good at innovation but often have limited experience transitioning new products from the laboratory to large-scale production. Furthermore, in the current economic climate, access to sufficient capital to set up production-scale capacity can be a formidable problem for a small company. Larger companies (for example, BASF, DuPont, GE Plastics) typically are not interested

in materials with small annual sales volume, so even licensing the new material to one of these companies may not be commercially feasible.

This foregoing discussion highlights a commonly encountered inconsistency between technical innovation and commercial progress. Until a production-scale source exists, pricing of new materials is at best highly uncertain and potentially unstable over time. This is in part due to the uncertainty surrounding demand and the associated volume of material that will be required. Taken together, these factors act as a clear deterrent to the adoption of new materials of literally all classes (polymers, metals, and ceramics).

For heavily loaded structures or structures that will experience temperatures higher than about 200 °Celsius, Ti alloys are the preferred material class. Ti alloys are about half as dense as steel or Ni-base alloys and possess a density-corrected strength and stiffness competitive with that of other metallic materials. Numerous grades of Ti alloys are in use today, and a strong domestic industrial base of suppliers exists for nearly all these grades. Ti alloys for structural applications can be divided into three groups based on their metallurgy: near  $\alpha$  alloys,  $\alpha+\beta$  alloys, and metastable  $\beta$  alloys (commonly called  $\beta$  alloys for short). Both the aircraft and propulsion original equipment manufacturers and several private engineering firms have extensive design experience with Ti alloys. Although most of this experience is with Ti-6Al-4V (Ti-6-4), other alloys also are widely used, particularly in jet engines and liquid-fueled rocket engines. The alloy most likely to be used in a launch vehicle, Ti-6-4, has been available and in use for more than 40 years but is still highly competitive with newer grades in large part because of its versatility. Potential applications of other alloys that have particularly attractive characteristics, such as a higher temperature capability, are discussed in the Reusable Reentry Vehicle and Propulsion Systems sections of this document.

The most commonly used structural grade of Ti alloy today, Ti-6-4, can be readily fusion welded, formed both by forging and as a sheet product, and conventionally machined, although each of these operations requires special precautions. In addition, the feasibility of friction stir welding has been demonstrated. Ti-6-4 also can be superplastically formed and diffusion bonded, enabling synthesis of innovatively shaped components. For launch vehicles, the most likely application for Ti alloys is in the structure that carries the reactions from the propulsion system to the vehicle itself. These applications typically involve heavy sections to accommodate the large loads, and the main property requirements are high strength, fatigue resistance, and fracture toughness. Ti alloys have been used in both military and commercial aircraft. Heavily loaded components in service today include the wing box of the B-1B bomber (Ti-6-4), the landing gear beam in the B-747 (Ti-6-4), and the landing gear truck beam in the B-777 (higher strength Ti-10V-2Fe-3Al [Ti-10-2-3]). The choice of Ti-10-2-3 for the landing gear truck beam reflects the time-based maturation of the newer  $\beta$ -Ti alloys, such as Ti-10-2-3. These alloys have the advantage of being "deep hardenable"—compared with Ti-6-4, they can develop full strength in thicker sections during heat treatment. For example, that the B-777's truck beam is up to 6 inches thick in some locations factored significantly in the choice of Ti-10-2-3. Because Ti alloys are about half as dense as steel, they are very competitive on a density-corrected basis. However, mass is not the only driver for some applications; the volume of a component also must be compatible with the space available for it. This factor also is a consideration in the choice of Ti-10-2-3 for the B-777 truck beam. And it also applies to an application such as landing gear, because it is retracted into the fuselage for aerodynamic reasons.



$\beta$ -Ti alloys would be an attractive option for a launch vehicle with a very heavy payload. These alloys can be processed and heat-treated to ultimate tensile strengths greater than 1,300 mega-Pascals (MPa), making them very efficient structural alloys. However, at these strength levels, the fracture toughness is decreased to about 40 MPa-m<sup>0.5</sup>, making damage tolerance marginal. For example, using a design stress that is two-thirds that of ultimate tensile strength, the critical crack size for an alloy with these properties is about 4 millimeters. Such a small critical crack size poses a challenge to any required field inspections associated with reusability requirements.  $\beta$ -Ti alloys' stiffness also is as much as 10 percent lower than that of  $\alpha$ + $\beta$  alloys. Ten percent lower stiffness generally is not an issue in a tension-loaded structure, but it can be an issue for a compression-loaded structure because of the potential for buckling. Designs with a higher section modulus can eliminate this concern, but the additional shape complexity will almost certainly add cost. In extreme circumstances, Ti alloys can be reinforced with ceramic fibers (typically silicon carbide) to increase their intrinsic stiffness, as will be discussed later.

Ti alloys are reactive when exposed to air at temperatures of 550 °Celsius or above. Consequently, any manufacturing operations that exceed this temperature limit must be performed in a protective atmosphere of argon (Ar) or helium (He) gas. An exception occurs during forging if enough excess material is left on the raw forging to contain the oxygen-contaminated layer so it can be machined away during the final machining of the finished component. How to deal with this reactivity issue is well understood, and it poses no concern other than the additional costs associated with the excess material and additional machining. In other operations, such as welding, use of specially designed fixtures incorporating inert shielding gas also effectively eliminates concerns about oxygen contamination. In hot-forming applications, the as-formed part is typically chemically milled to remove the oxygen-rich surface layer because this layer typically has lower ductility and can cause fatigue cracking in service. The practice of eliminating all oxygen-contaminated material has served the aerospace industry well over the years but is quite conservative and restrictive. This matter is discussed in greater detail in the Reusable Reentry Vehicle section of this document.

In summary, although the choices of materials for launch vehicles are in principle numerous, in practice these choices are reduced by a variety of application-specific considerations that include manufacturing capability for large components and manufacturing cost. The foregoing discussion has attempted to examine the prospects for advanced Al alloys, PMCs, and Ti alloys in light of these perceived practical constraints. On a case-by-case basis, a variety of requirements are imposed by design constraints, which some materials meet more readily than others. In all cases, discussion of available material options was constrained by the assumption that the maximum service temperatures would be relatively low. Consequently, the material classes discussed here are all intended for relatively low-temperature use. The separate case of a reusable single-stage-to-orbit vehicle, where operating temperature requirements are considerably higher, is discussed in a later section of this document. Ultimately, materials are selected to optimize structural performance, and a coordinated approach of materials selection and geometric design is essential to this. Going forward, a design using a synthesis process that treats form, fit, function, and materials capability as equal constraints is needed to achieve true optimum structural efficiency.

## REUSABLE CREW MODULES

The concept of manned orbital crew modules has evolved from the Mercury capsules to the Gemini and Apollo programs to the space shuttle, the first fully reusable crew module. The shuttle also has a combined payload bay used for transporting satellites into orbit and hardware for developing the International Space Station and for repairing and refurbishing the Hubble telescope, among other uses. The reusable nature of the shuttle crew module introduced a number of design and materials selection challenges. Perhaps foremost among these is the requirement for a thermal protection system (TPS) that would protect the crew during reentry and also minimize the intermission refurbishment requirements of the spacecraft itself. During the early days of the shuttle development program, there was much initial interest in a metallic TPS because it appeared to better meet the program's needs. Ultimately, however, ceramic tiles were used on the underbody and carbon-carbon composites (C-CCs) were used on the leading edges of the wings. The shuttle design itself can therefore be characterized as a "cold structure" with an insulating TPS. For example, much of the shuttle load-bearing structure is made of the Al alloy 2219, in part because it is fusion weldable and in part because it retains its strength at moderately elevated temperatures better than other high-strength Al alloys can. The refurbishment needs of the ceramic shuttle tiles after each flight reputedly are considerable and increase with vehicle age. The C-CC wing leading edges are basically not repairable but require scrutiny. Hindsight shows that C-CCs "age" and lose much of their fracture toughness during repeated thermal exposure. (This loss of toughness was a prime factor in the Columbia disaster. Had a metallic heat shield that included the wing leading edges been used, this disaster arguably could have been avoided.) If the discussion of a metallic TPS were held today, the outcome might not be much different. Certainly any serious consideration of a reusable single-stage-to-orbit vehicle today would need to reopen the discussion of a metallic TPS. The challenges and opportunities associated with a metallic TPS are discussed later.

The design efficiency of an integrated TPS and load-bearing structure is extremely attractive. Such a design requires availability of high-temperature alloys that also have good strength at the moderate temperatures to withstand the aerodynamic and vibrational loads encountered during launch and orbital insertion. Any attractive alloy also must have reasonable intrinsic resistance to oxidation at the reentry temperatures and should be capable of being fabricated into sheet gauges at reasonable cost. Meeting these various requirements in combination becomes quite daunting. Earlier programs such as the DynaSoar reusable reentry glider devoted considerable time and resources to examining the use of refractory alloys such as Mo-0.5%Ti (Moly half Ti) and several Columbia-based alloys for the TPS and some hot structure. All the refractory metal alloys are solid solution strengthened and, consequently, have relatively low ambient temperature strengths. They also are quite dense, making the density-corrected strength even less attractive. Refractory metals and their alloys react extensively when exposed to air at elevated temperatures. Therefore, even if the mechanical property limitations could be overcome, any hot structure would require an oxidation-resistant protective coating. In the case of the DynaSoar program, scientists extensively investigated a surface conversion coating of MoSi<sub>2</sub> formed by reacting the Moly half-Ti alloy with Si powder in a high-temperature fluidized bed. With the benefit of hindsight, it is now unclear how a large structure could have been successfully coated in this manner. This is particularly true when the brittle nature of MoSi<sub>2</sub> is

considered in light of the thermal stresses that were certain to develop in a large structure placed in the fluidized bed.

**Reusable Single-Stage-to-Orbit Vehicles**

A reusable single-stage-to-orbit (SSO) vehicle will require metallic materials for the TPS and for much of the other hot structure. This will be challenging from the standpoint of an empty vehicle weight. With the exception of military applications, which are outside the scope of this document, empty vehicle weight is a critical metric because every additional pound of empty weight reduces the payload by the same amount (assuming a fixed propulsion capability). As mentioned earlier, the key to a lightweight vehicle is the use of design methods that integrate the TPS and the load-bearing structure to minimize structural redundancy and single-function structure (for example, a TPS that is not load bearing). Achieving this goal will require new design paradigms that incorporate true synthesis of new structural concepts. In reality, such designs can be completed only if they are based on a detailed set of mission requirements, including the number of missions and expectations for turnaround time between missions. Furthermore, operational parameters such as the value of inserting a pound of payload into orbit are needed to bound the cost of the initial vehicle and the maintenance cost per mission (translated into cost per pound of payload). Absent such specific data, the following discusses possibilities for materials systems that can enable a reusable SSO vehicle. It is perhaps more efficient to discuss these materials according to their principal capability and the anticipated temperature regime in which they can be used most productively. This categorization method is illustrated in Table 1.

**Table 1. Potential Materials by Use Temperature Regime and Property**

<b>Temperature Regime</b>	<b>Specific Strength</b>	<b>Specific Stiffness</b>	<b>Fatigue Resistance</b>	<b>Fracture Toughness</b>	<b>Creep Resistance</b>
Ambient up to 250 °C	PMCs; Advanced Al alloys; AMCs*; Ti alloys; TMCs*	PMCs; AMCs; TMCs	PMCs; AMCs; Ti Alloys; TMCs	PMCs; Ti alloys	Ti alloys; TMCs
250 °C up to 550 °C	Ti alloys; TMCs	TMCs	Ti alloys; TMCs	Ti alloys	Ti alloys; TMCs
Above 550 °C	Ni-base alloys; Ti aluminides; Refractory metal alloys; CMCs*; C-C Cs*	Ti aluminides; CMCs; C-CCs	Ni-base alloys; Refractory metal alloys	Ni-base alloys; CMCs; Refractory metal alloys	Ni-base alloys; Ti aluminides; CMCs; Refractory metal alloys; C-C Cs

AMCs = Al matrix composites; TMCs = titanium matrix composites; CMCs = ceramic matrix composites; C-CCs = carbon-carbon composites

Table 1 shows there are essentially 10 distinct classes of candidate materials for use in a reusable SSO vehicle. Their usefulness for specific applications and components depends on the operating temperature regime and the design-limiting material property. Some background and characteristics of each of these materials are described in this section. Applications of some of these materials have already been addressed, so the discussion here is limited to applications for a reusable SSO vehicle.

### **Advanced Al Alloys**

This class of materials is limited by its temperature capability because, even if used in an embedded structure, the thermal soakback from the hot external structure can lead to softening in real time or overaging during extended exposure (that is, after several missions). Scientists have worked to develop high-temperature powder-metallurgy Al alloys, mainly alloys containing Fe, cobalt (Co) and cesium (Ce) or Mn and Si. These alloys are not routinely produced today owing to a lack of demand stemming in part from their cost and their relative lack of maturity as judged by the high variability in mechanical properties between lots of material. Consequently, the main application for Al alloys is in the crew compartment itself, where temperatures must be maintained at levels that are tolerable for the human occupants. Al alloys have marginal stiffness, even on a density-corrected basis. However, using fabricated panels with Al face sheets and a lightweight core can minimize this limitation. Such panels have a high section modulus, which increases the structural stiffness without adding much weight. Earlier uses of phenolic honeycomb cores experienced only limited success because of the tendency of the core to absorb water from the environment if a breach of the face sheet or the face sheet core bond occurred. Today, Al phenolic honeycomb sandwich construction is unpopular among aircraft and spacecraft designers because of this earlier, unfavorable experience. However, a new possibility for lightweight stiff structures—Al face sheets with a foamed Al alloy core—is worthy of consideration. Considerable progress in making uniform-density Al and other metallic foams has been realized in the past 10 years. This new class of sandwich materials is sufficiently different from the earlier versions to merit a careful evaluation.

### **Polymer Matrix Composites**

As described in the Launch Vehicle section, polymer matrix composites have excellent strength, stiffness, fatigue resistance, and fracture toughness. All polymeric materials are to some degree susceptible to degradation when exposed to ultraviolet (UV) radiation. For an orbiting vehicle, a major limitation is the effects of UV radiation on the polymer matrix. Given their limited time at altitude, this vulnerability is not an issue for launch vehicles; however, it is a concern for structures that remain in orbit for an extended time at altitudes where the UV intensity is much greater. Although there are coatings that protect substrates (PMCs in this case) from UV radiation, the risk of these coatings being breached and the uncertainty about their effectiveness in orbit make UV exposure an ongoing concern. Any consideration of using PMCs for exterior applications would need to include an evaluation of their effectiveness. As discussed for Al alloys, PMCs also could be considered for interior applications where temperatures are within the material capabilities. As discussed earlier, some polyimide resins are usable up to about 300 °Celsius; therefore, the low density and excellent specific stiffness of PMCs make them viable candidates for some components. As also discussed, some polyimides, such as PMR-15, contain *methylenedianiline*, and care must be taken to

ensure that any outgassing that occurs in space would not liberate any of this toxic material—at least not where it could be ingested by the crew.

### **Al Matrix Composites**

Al matrix composites (AMCs) are typically made by mixing short fibers or even particulate silicon carbide (SiC) with Al alloy powder and hot-pressing or mechanically consolidating the mixture by extrusion or forging. AMCs have higher modulus and strength but suffer ductility losses owing to the hard, nondeforming SiC second phase. They also are much better in fatigue because the SiC particles or short fibers mitigate the effects of planar slip in precipitation-hardening alloy matrices. Machining, fusion-welding, or cold-forming AMCs is difficult. Mechanical fastening is possible, but drilling fastener holes is difficult and expensive because the wear caused by the hard, reinforcing phases shortens tool life.

Most of the AMCs produced to date have used relatively simple Al matrix alloys such as 6061 and 5083. This presumably is because of the conventional wisdom that AMCs are not heat treatable and the perception that no benefit is gained by using more complex alloy matrices. This is probably the case for a conventional solution treat-and-age approach. Consequently, there has been little effort to optimize AMC systems. For the right application where AMCs could provide a significant benefit, this could present an opportunity. For example, using the high-temperature Al-Fe-Co-Ce alloy powder as the matrix could prove interesting and might permit use of AMCs at up to 200 °Celsius—a temperature at which Ti alloys do not provide any significant advantage, but one that is too high for conventional Al alloys to be suitable.

In sum, while AMCs are not really a commercial materials system today, sufficient research has been performed to establish proof of concept. If an adequate market for AMCs were to emerge, the time and cost to make them commercially available could prove acceptable.

### **Ti Alloys**

Ti alloys also have been discussed earlier, but mainly in the context of heavy-section, large-load-bearing applications for launch vehicles. Here, the potential of Ti alloys for lighter gauge applications in the warm structure and the TPS is considered. Table 1 shows that at intermediate temperatures, Ti alloys are attractive in all aspects except for specific stiffness. What this table does not capture is Ti alloys' propensity to react with oxygen in the air to form an oxygen-stabilized  $\alpha$  phase layer on the surface known as  $\alpha$  case. An example of  $\alpha$  case is shown in Figure 3.

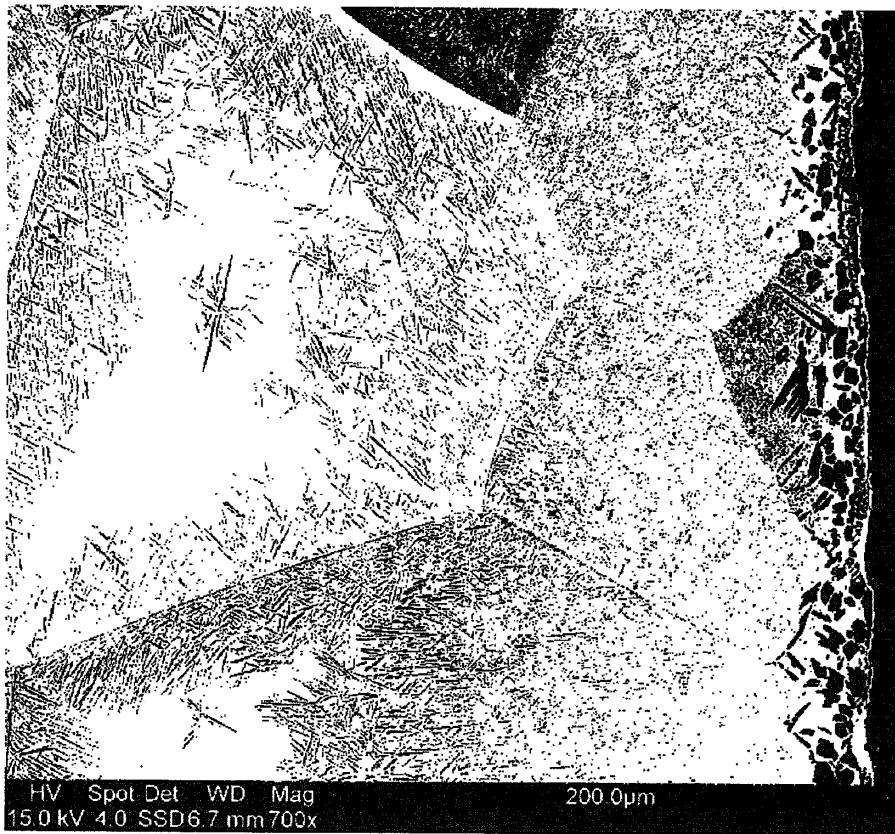


**Figure 3. Micrograph Showing  $\alpha$  Phase Formation at the Surface of a Ti Alloy That has Been Exposed to Air at Elevated Temperature**

The  $\alpha$  case is harder than the matrix because oxygen is a potent  $\alpha$ -phase solid-solution strengthener. As with almost all other strengthening reactions, the increased strength is accompanied by reduced ductility. Again, drawing on conventional wisdom, the presence of  $\alpha$  case in sheet structures has been forbidden by specification, design practice, or whatever means a company uses to manage its hardware. Less clear is how truly detrimental  $\alpha$  case is to properties. Essentially no effort has been made to determine whether it can be tolerated if the affected hardware is allowed to operate at a modestly reduced stress. The industry standard for  $\alpha$  case has essentially been one of zero tolerance. Given the significant potential weight advantage associated with use of Ti alloys in portions of the TPS and warm structure, this conservative approach needs to be revisited. Several key questions related to this are:

- Is  $\alpha$  case truly detrimental to the load-bearing capability of Ti alloy sheet structures?
- If so, is there a limiting amount that can be tolerated without significantly degrading the structural capability?
- Which properties are the most severely degraded?
- Are  $\alpha$  case formation and property degradation alloy dependent?
- If so, which alloys are the most tolerant of  $\alpha$  case formation?

- Once  $\alpha$  case is present, can the structure be repaired (for example, by fusion or friction stir welding)?

The Air Force Materials and Manufacturing Directorate is starting a new project intended to address these questions. The motivation for this program is hypersonic flight vehicles. The results from this U.S. Air Force program should prove highly useful to the design of future reusable SSO vehicles.

Earlier uses of Ti alloys at high temperatures included the skin and much of the load-bearing structure of the SR-71 Blackbird. This airplane flew successfully at peak speeds in excess of mach 3.2 for 34 years (1964-1998). While the maximum skin temperatures are not readily available, they were in excess of 300 °Celsius. There were no known issues involving  $\alpha$  case during the SR-71's service. Notably, the primary alloy used for the SR-71 was one of the original  $\beta$ -Ti alloys, B-120 VCA, the composition of which is Ti-13V-11Cr-3Al. The primary reason for choosing this alloy was that it is much easier than any of the  $\alpha+\beta$  Ti alloys are to roll into sheet gauges. Today there are newer  $\beta$ -Ti sheet alloys featuring a better balance of properties that could be used in the same way as B-120 VCA. The most common of these is Ti-15V-3Cr-3Sn-3Al. However, the successful use of B-120 VCA raises the question of whether  $\beta$ -Ti alloys are more resistant than  $\alpha+\beta$  alloys such as Ti-6-4 are to  $\alpha$  case formation.

The attraction to using Ti alloys, in addition to their structural efficiency, is the extensive industrial base for making the material in a variety of product forms and the extensive knowledge base resulting from the many successful applications of Ti alloys in high-performance products. For example, the ability to superplastically form Ti alloys such as Ti-6-4 creates the opportunity for design of a structure that functions both as load bearing and as thermal protection.

### Ti Matrix Composites

As Table 1 showed, Ti alloys are not especially attractive for their specific stiffness. One way to overcome this limitation is to reinforce a Ti alloy matrix with SiC fibers. In this case, the fibers are "long" fibers—they have sufficient length for the matrix to transfer the maximum possible fraction of the external load to the fiber. The fibers are essentially monofilaments and must be carefully placed so adjacent fibers do not touch one another. Areas of contact between fibers essentially are incipient cracks that degrade the mechanical strength. As Table 2 shows, TMCs have excellent properties.

**Table 2. Example of Properties of Ti Matrix Composites**

Property	Property Value (English / Metric Units)
Ultimate tensile strength	276 ksi / 1902 MPa
Young's modulus	32.8 msi / 226 GPa
Strain to fracture	0.95%
Density	0.16 lb/in <sup>3</sup> / 4.43 g/cm <sup>3</sup>
Fiber Volume fraction	0.39

Figure 4 shows an example of a Ti matrix composite (TMC) cross section.

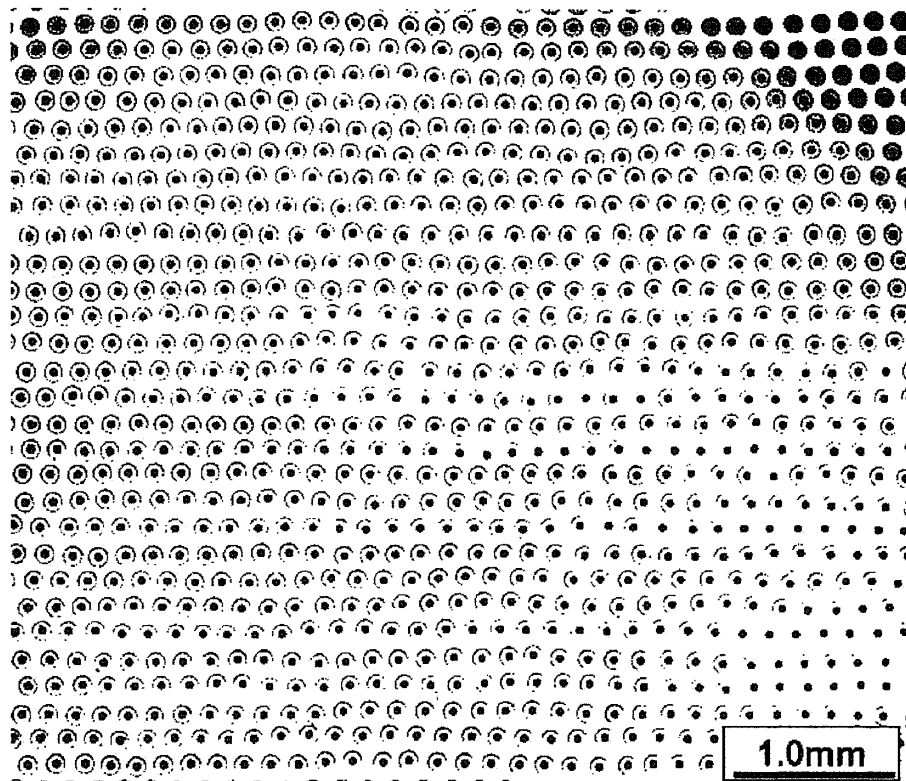


**Figure 4. Cross-Section Micrograph of a Ti Matrix Composite.** Small, dark centers of fibers are C monofilament substrates for deposition of SiC (light micrograph). Material system: Matrix alloy - Ti-6242; Fiber - SiC about 5.6-mil-diameter SCS-6

Table 2 shows that the strength and stiffness properties of TMCs can exceed those of the Ti matrix (or other  $\alpha+\beta$  Ti alloys) by more than a factor of two with no increase in density. So why are TMCs not in widespread use? The foremost reason is cost. Another reason is the availability of SiC fiber for TMCs.

- During the 1990s, when the U.S. government (mainly DoD) was interested in and provided development money for TMC R&D, the most attractive reinforcing fiber was SCS-6™, which was produced exclusively by Textron Specialty Materials (TSM) in Lowell, MA.
- Unfortunately (at least in hindsight), TSM made a business decision not to sell fiber and to instead forward-integrate and sell TMC components or finished TMC mill products. This decision stemmed in part from TSM's negative business experience with development of B-based fiber (Boro-SiC™) for first-generation TMCs.
- Prior to making this business decision, TSM did not develop sufficient TMC-manufacturing expertise to properly position itself as a producer of TMC products with consistent properties.



- A couple of costly and highly visible TMC component test failures using TSM materials called into question the viability of TMCs. In truth, the real issue was one of quality and not the fundamental viability of the TMC material concept.
- These failures led to extreme caution by the government, which promptly imposed stringent quality requirements on TSM. Consequently, TSM became a serious bottleneck for availability of TMCs with acceptable quality. As a result, numerous large, government-funded R&D programs fell behind schedule to the point that some were canceled and others were abandoned.
- Other, less attractive SiC fibers were being developed during this period, including Nicalon in Japan and Sigma in the United Kingdom. Because SiC fiber and TMCs were deemed strategic materials and neither of these alternate fibers was produced in the United States, there was reluctance to experiment with them, and the U.S. government occasionally prohibited their use in federally funded R&D programs.
- The issue of fiber availability became a major distraction from the real business at hand—that is, improving the consistency and reducing the cost of the TMC product.
- In the end, TSM partially relented, but by then such limited interest in TMCs existed that the original opportunity was lost. Furthermore, there still was no concrete evidence that TMCs could be produced with sufficiently consistent properties that they could be considered an engineering material (at any cost).
- In the mid-1990s, a cost study that assumed fiber availability showed that TMCs that meet specification properties could be manufactured for about \$500/lb (in 1995 \$) if the use volume was about 10,000 lb/year. Finding enough low-risk, high-value applications to consume this quantity of TMCs was not deemed possible.
- Consequently, work on TMCs halted after an investment of about \$500 million of U.S. government funds and a (presumably) comparable, but less well known private sector (mostly independent R&D \$) investment.
- One lesson from this is that a credible market and cost study should be undertaken before embarking on a major R&D program to develop revolutionary materials such as TMCs.

The foregoing discussion exemplifies the challenges associated with developing and commercializing a revolutionary new materials system. New material concepts originating from nonproduction sources such as national laboratories or research universities should be approached with caution and never be put on the critical path of product design. Even if a new material is vetted through an established production source, the timing of full commercialization should be carefully examined.

### **Ni-base Alloys**

Ni-base alloys have been considered real engineering materials for at least 40 years. Because of their relatively low rate of strength loss with increasing temperature, Ni-base alloys are also called "superalloys." They are commonly used at temperatures well in excess of half of their melting point ( $T_m$ ), which is the accepted useful limit for most structural metallic materials. There is no other class of structural alloys for which this is true. Ni-base alloys have been used in turbine engines of all types almost since their

inception. In fact, Ni-base alloys are a prime enabler of the modern gas turbine engine. As a result, this class of materials has a well-established industrial base for the production of literally all product forms. There is a second class of Ni-base alloys that has excellent resistance to attack in aggressive environments, such as those encountered in petroleum recovery, but these alloys are not of interest for high-temperature applications. To avoid any confusion, the term Ni-base alloys is used in this document to mean *high-temperature* Ni-base alloys.

Ni-base alloys have a high elevated temperature strength because they typically contain Al and Ti, which enable them to be precipitation strengthened. The alloys with the highest temperature capability are strengthened by precipitates of Ni<sub>3</sub>Al (called  $\gamma'$ ), which have a positive temperature coefficient of strength up to about 1,000 °Celsius. This unusual characteristic accounts for Ni-base alloys' elevated temperature capability. In combination with the ordinary temperature dependence of the matrix strength, the overall temperature dependence is quite low compared with that of any other class of structural alloys. Ni-base alloys also contain alloying additions of refractory elements such as tungsten (W), tantalum (Ta), and niobium (Nb). These additions also improve the elevated temperature strength because they diffuse slowly and strengthen the matrix. Because Ni-base alloys are used at elevated temperatures, they contain Cr additions in significant concentrations to improve their oxidation resistance. The tailoring of the properties of Ni-base alloys has been studied extensively and is quite well understood empirically, albeit less so in a fundamental sense. Current-generation Ni-base alloys contain as many as 10 alloying additions, and interelement interactions make gaining a fundamental understanding of alloying effects a major challenge.

Production of Ni-base alloys has evolved over several decades. Both ingot metallurgy and powder metallurgy methods are used to produce a full range of mill products. New alloys have periodically been introduced in response to specialized needs. Sometimes these alloy development efforts have been so focused on the "specialized need" that retention of other generally accepted Ni-base alloy properties has been overlooked. An example of this is the development of early "low coefficient of thermal expansion" ( $\alpha$ ) alloys (the so-called low- $\alpha$  alloys). An example of an application for which low- $\alpha$  alloys are attractive is structures in which there are two or more concentric rings connected by radial struts. In the presence of a radial temperature gradient, these alloys tend to crack during thermal cycling situations owing to "thermal fatigue." In principle, the availability of an "Invar type" alloy with structural characteristics reduces the thermal strains and improves the thermal fatigue life. Invar is so named because it uses the magnetic characteristics of Ni to offset normal thermal expansion, resulting in much lower  $\alpha$  values. It was recognized that this concept could also be adapted to Ni-base structural alloys. The first-generation low- $\alpha$  alloy, Inco 903, had about half the coefficient of thermal expansion compared with ordinary Ni-base alloys up to the Curie temperature. This remarkable alteration of a physical property was achieved by removing the Cr from the alloy to intensify the magnetic effects of magnetostriction. An unfortunate, unintended consequence of this composition alteration was that the oxidation resistance was seriously degraded. In particular, Inco 903 had a propensity for intergranular cracking in air under stress, rendering it of limited utility as a structural alloy. In fact, the cracking was so severe it was given a name: stress-assisted grain boundary oxidation (SAGBO). A second-generation low- $\alpha$  alloy, Inco 909, contained Si to help improve the oxidation resistance, but this alloy has not gained widespread acceptance, possibly because Inco 903 problems were so severe. Low- $\alpha$

alloys' superior thermal fatigue resistance gives them great potential for use in TPS; thus, it would be appropriate to revisit this class of alloy after addressing its past problems.

Many of the Ni-base alloys are fusion weldable, but the higher strength grades are prone to cracking without special precautions such as preheating the work piece. Most alloys capable of being processed into sheet also can be processed to create a fine-grained structure. The fine-grained material can be superplastically formed, which is potentially of very important benefit to making light-gauge, load-bearing structures and TPS components. Finally, although almost all Ni-base alloys contain Cr and Al, both of which improve oxidation resistance by forming a stable, protective scale, this scale begins to lose its effectiveness above about 1,000 °Celsius. A number of effective environmental coatings have been developed by the gas turbine industry for Ni-base alloys. The only concern or unknown for application in a reusable SSO vehicle is the durability of these coatings under very high mass flow conditions, such as during reentry.

### **Refractory Metal Alloys**

Refractory metal alloys were discussed briefly earlier in connection with the DynaSoar project. Subsequent to this, there has been limited systematic interest in designing aerospace structures that incorporate refractory metal alloys. There has been interest in using these alloys for high-temperature gas-cooled nuclear reactors, where the operating environment is benign and well controlled, but this has limited relevance to the current discussion of space vehicles required to withstand reentry into the earth's atmosphere. The attraction of refractory metals as a class is the high melting temperature of Mo, Nb, and Ta. Although alloys of these metallic elements exhibit "normal" temperature dependence of mechanical strength,  $0.5T_m$  of Nb or Mo is still a higher temperature than Ni-base alloys can withstand. Of the three metals, Nb is by far the most attractive because of its lower density, lower elastic modulus, and better (but not good) oxidation resistance. The clear barrier to use of Nb alloys is their reactivity in air at high temperatures. There are coatings for these alloys, but at 1,250 °Celsius, a breach in the coating will cause immediate, catastrophic failure.

A reasonable design practice for critical structure, such as the TPS, is to disallow use of any coated material if the material fails catastrophically when the coating is breached. If this practice were the norm, then refractory metal alloys would not be usable in the TPS or other critical hot structure in a reusable SSO vehicle.

### **Ceramic Matrix Composites**

Ceramic matrix composites (CMCs) are attractive because they are much tougher than, but retain the high-temperature capability of, monolithic ceramics. CMCs' toughness is derived from the fibers used to reinforce the ceramic matrix. When a CMC is loaded in tension and the stress in the ceramic matrix reaches a critical value, microcracks develop. This stress level is known as the matrix microcrack stress. In a monolithic ceramic such as silicon carbide (SiC) or silicon nitride (Si<sub>3</sub>N<sub>4</sub>), microcracks would propagate rapidly, causing immediate failure. For this reason, monolithic ceramics are not suitable for tension-loaded applications. This characteristic is mitigated in CMCs by reinforcing the ceramic matrix with high-strength ceramic fibers, typically Al<sub>2</sub>O<sub>3</sub> or SiC, whose role is to bridge and arrest the cracks. Under continued loading, the fibers also

will eventually fracture at their weakest points, which, statistically, is often somewhere in the matrix rather than at the mouth of the crack. These fractured fibers then must be pulled out of the matrix during crack extension under continued loading, an action that dissipates additional energy. Therefore, the total energy expended during fracture of a CMC is much greater than it would be in the case of a monolithic specimen of the ceramic matrix. The crack bridging and pullout mechanisms of toughening, with the attendant increase in energy dissipation during fracture, are the conceptual foundation for CMCs. In SiC fiber-reinforced SiC matrix (called SiC-SiC) CMCs, the toughness can be as high as 10 times that of the unreinforced matrix. Clearly, the nature of the fiber-matrix interface determines the resistance to fiber pullout after fracture and controls the toughness. In high-temperature CMCs, the fibers are coated to achieve an intermediate fiber-matrix interfacial bond strength that optimizes pullout toughening. If the interface is too weak, the fibers pull out too easily. If it is too strong, the fibers break without any pullout. Neither of these situations maximizes the toughness. Therefore, the challenge in creating a tough CMC is not only creating this interface but also finding a coating that will remain stable over time during exposure to elevated temperatures. As service temperature increases, this latter requirement becomes more challenging. For extended service, SiC-SiC CMCs currently are limited to about 1,400 °Celsius, but this is higher than the capability of metallic materials.

The matrix microcrack stress is also significant because once the matrix develops microcracks, it allows the environment to gain access to the fiber-matrix interfaces. The role of environment can be to alter the nature of the interface and reduce the extent of pullout toughening. The obvious difficulty with this is that the properties are better initially than after a period of exposure in service. This leads to a nonconservative design that is dangerous. Absent an arbitrary knockdown, there currently exists no means of estimating the reduced toughness as a function of service life.

Nevertheless, CMCs are the material class that holds the greatest promise of defeating the temperature limits of current metals. An important issue at present is the limited industrial base for producing CMCs and the even more restrictive range of suitable ceramic fibers available for use as the reinforcement in CMCs. The cost of CMCs is currently very high but should come down with increased demand, as happened with TMCs. Even so, CMCs will always be expensive, making development of efficient designs that make optimal use of this class of material important.

### **Carbon-Carbon Composites**

Carbon-carbon composites (C-CCs) consist of carbon fibers in a typically amorphous carbon matrix. In principle, this class of materials is very attractive because it has very low density and high strength at elevated temperatures. C-CCs also have good oxidation resistance at very high temperatures (1,200 °Celsius) because they use an Si-rich coating that forms a stable, protective SiO<sub>2</sub> film on the surface. This coating system is "self healing" if breached because, among other things, it is glassy (viscous) and reforms over cracks. The principal vulnerability occurs at intermediate temperatures where the viscosity of the glass is high enough that it may not flow rapidly enough to heal a breach, exposing the reactive C substrate to the damaging oxidizing environment. As with CMCs, there also are some questions concerning long-term changes in the fiber-matrix interfaces that are at least partially responsible for the loss of impact toughness over time, as experienced in the Columbia accident.

Therefore, instabilities that cause time-dependent reductions in toughness must be understood before these materials can be considered candidates for future TPS applications.

### **Titanium Aluminides**

Titanium aluminides are intermetallic compounds that form between Ti and Al. There are three such compounds—Ti<sub>3</sub>Al, TiAl and Al<sub>3</sub>Ti—but the one of principal interest is TiAl, often referred to as gamma titanium aluminide or  $\gamma$ -TiAl. This compound contains about 35 weight % Al, but ternary and quaternary alloys based on TiAl typically contain somewhat less than this amount.  $\gamma$ -TiAl is interesting for intermediate-temperature applications for several reasons. These include a lower density, at least a 125 °Celsius higher temperature capability, and better surface stability (oxidation resistance) compared with conventional Ti alloys. The surface scale that forms during oxidation of  $\gamma$ -TiAl is Al rich and is more protective than the TiO<sub>2</sub> scale that forms on conventional Ti alloys. Like most other intermetallic compounds,  $\gamma$ -TiAl has very limited ductility at temperatures up to about 600 °Celsius but is not brittle in the classical sense; that is, it has the capability to deform plastically before fracturing. The ductility increases as temperatures increase and is quite good at normal service temperatures.

$\gamma$ -TiAl alloys' limited ductility poses manufacturing problems for any wrought products. These issues are manageable but reduce product yields, which in turn impacts cost. Recent work in Austria has demonstrated that some  $\gamma$ -TiAl alloys can be made into sheet. This is particularly relevant to applications such as metallic TPS. Other work has demonstrated that some  $\gamma$ -TiAl alloys can be conventionally forged, albeit with care. Should one or more of the efforts currently under way to produce low-cost, prealloyed Ti powder prove successful, the availability of affordable  $\gamma$ -TiAl alloy powder could be a major cost breakthrough.

The development and maturation of  $\gamma$ -TiAl alloys has taken more than 30 years. This is in part due to the lack of actual production applications because of designer's concerns regarding the limited low-temperature ductility of all the  $\gamma$ -TiAl alloys. Today, finally, there are several applications of alloys based on  $\gamma$ -TiAl, the most significant of which are two stages of low-pressure turbine blades in the engine General Electric is providing for the Boeing 787 and the growth 747 (called the 747-8). These blades are cast to near net shape and will operate at temperatures up to about 750 °Celsius. Another application is a cast  $\gamma$ -TiAl turbocharger rotor Mitsubishi uses in a production auto because it has half the mass of an equivalent Ni-base alloy component.

A potentially ideal, high-volume application of  $\gamma$ -TiAl alloys is exhaust valves for autos. If the low-cost powder mentioned earlier becomes a reality, this factor, coupled with the current pressure to improve fuel consumption in American cars, could make this prospect a reality. The point of this short discussion of non-space-related applications of  $\gamma$ -TiAl alloys is that realization of any or all of these applications will create a stronger production base for this class of alloy, which in turn will make their introduction into future space platforms easier and more cost effective.

## PROPULSION SYSTEMS

Among propulsion systems, only reusable rocket engines are considered here because they hold potential for significant progress that could reduce the cost of placing payloads into orbit.

The basic concept of the space shuttle main engine is still viable, but the durability of the materials used to make the hardware has been a major expense and source of concern for NASA. Much of the concern is related to the effects of hydrogen on the Ni-base alloys used in the turbo pumps. The turbo pumps are the heart of a liquid-fueled hydrogen-oxygen rocket engine because they deliver the fuel and oxidizer to the thrust chamber. The turbo pumps rotate at a very high speed—up to 35,000 rpm. Such speeds create enormous centrifugal stresses in the rotating components, particularly the disks that hold the air foils used to extract work from the hot gas stream. One side of the turbo pump rotor operates in the hot gas stream created by the combustion of the oxygen-hydrogen mixture; the other end is a cryopump that operates at cryogenic temperatures, either in liquid oxygen (90 K) or in liquid hydrogen (20 K). The hot side, a turbine, resembles the turbine rotor in a gas turbine engine and is made of many of the same Ni-base alloys. The cryopump is made of Ti alloys.

The turbine essentially operates in a hydrogen-rich supercritical steam environment at a maximum temperature of about 1,050 °Celsius. The turbine disk is a forged Ni-base alloy, and the air foils are single-crystal investment castings. Neither material is well suited to operate in a hydrogen-rich environment; however, no other material class can withstand the operating temperatures and has better hydrogen tolerance—a situation that still prevails today. The mechanism of hydrogen-induced cracking is much better understood today as the result of extensive research over the past 25 years. Therefore, it would be very useful to use this improved understanding to design a Ni-base alloy that has improved hydrogen tolerance. If successful, a turbine that has improved resistance to hydrogen cracking would greatly reduce the intermission refurbishment time and cost.

Traditionally, the cryopump rotating parts have been made from forgings of the near- $\alpha$ -phase Ti alloy Ti-5Al-2.5Sn (Ti-5-2.5). This alloy has been chosen for its superior notched tensile strength compared with Ti-6-4 when tested at cryogenic temperatures. Hindsight suggests it is unclear that notched tensile strength is the best criterion for selecting a cryogenic rotor material. The use of notched tensile strength originated with steels. Here, the hydrostatic stress state at the notch root could trigger the onset of brittle fracture of the type seen in smooth tensile tests below the ductile brittle transition temperature (DBTT). Ti alloys do not exhibit a DBTT; therefore, true fracture toughness measured at the relevant temperature is a more accurate indication of the fracture resistance of the rotor. An examination of the limited available fracture toughness data for the two alloys shows no clear advantage in using Ti-5-2.5. Because Ti-5-2.5 is more difficult to produce than Ti-6-4, using Ti-5-2.5 adds cost to the cryopump. Other, newer, higher strength Ti alloys—for example, several of the newer  $\beta$ -Ti alloys—may be even better suited than Ti-6-4 is for this application. The critical question of how much toughness is really required cannot be answered at present because the notched tensile ratio has been the deciding criterion. Therefore, a new

design of a cryopump potentially can benefit from these new materials and from abandoning the use of notched strength as a design paradigm.

The combustion chamber of a rocket engine is made from a copper alloy and is cooled by passing liquid hydrogen through channels in the outer wall. The space shuttle main engine combustion chamber is made of NARloy-Z, a Cu-3%Ag-0.5%Zr alloy that has excellent thermal conductivity and better strength than the commercially available Cu-0.15%Zr alloy known as AMZIRC. While a lighter combustion chamber would be welcome, developing hydrogen-resistant turbine materials would be a much better use of available rocket engine alloy development resources.

## **SUMMARY AND RECOMMENDATIONS**

This document has attempted to review a range of materials that may have promise for all aspects of aerospace platforms. Because of the breadth of this topic, discussion has focused on opportunities and associated risks, but with little technical detail. Practical issues such as manufacturing capabilities and costs and the availability of materials also have been addressed where appropriate. Another recurring issue is the ability to achieve better design efficiency through a design synthesis process that concurrently treats form, fit and function, manufacturing capability, and materials capability as equally important design constraints. Although this approach has yet to be successfully used for a major high-performance structure project, engineering is nearing a state of development where it may now be feasible.

If the space shuttle is used as a benchmark, it is clear that numerous opportunities will exist to improve structural efficiency. This possibility reflects the progress made since the shuttle and its engine were designed. Improved durability and reduced operating cost also are possible. The issue of long lead time holding back these improved design methods is most often one of timely availability of new, attractive materials that are mature enough to be used in a system without increasing the risk of failure. The materials community is actively developing and using computational models and simulation methods to address this concern. Despite some progress, further advances are required to bring computational materials engineering to the desired level of maturity.

1. Hatch, J. ed. Aluminum, Properties and Physical Metallurgy. American Society for Metals, 1984.
2. Chawla K. Composite Materials, Science and Engineering 2<sup>nd</sup> edition. Springer, 1998.
3. Baker, A., Dutton, S. and Kelly, D. Composite Materials for Aircraft Structures 2<sup>nd</sup> edition. AIAA, 2002.
4. Lütjering, G and Williams, J. Titanium, 2<sup>nd</sup> edition. Springer, 2007.
5. Sims, C. and Hagel, W. The Superalloys. Wiley, 1972.
6. Mishra, R. and Ma, Z. Friction Stir Welding and Processing, Materials Science and Engineering. v.50, pp. 1-78, 2005.

~~UNCLASSIFIED//FOR OFFICIAL USE ONLY~~



# Defense Intelligence Reference Document

*Acquisition Threat Support*

23 March 2010

ICOD: 1 December 2009

DIA-08-1003-011

## Metallic Spintronics

~~UNCLASSIFIED//FOR OFFICIAL USE ONLY~~



## **Metallic Spintronics**

**Prepared by:**

(b)(3);10 USC 424

**Defense Intelligence Agency**

**Author:**

(b)(6)

**Administrative Note**

COPYRIGHT WARNING: Further dissemination of the photographs in this publication is not authorized.

This product is one in a series of advanced technology reports produced in FY 2009 under the Defense Intelligence Agency, (b)(3);10 USC 424 Advanced Aerospace Weapon System Applications (AAWSA) Program. Comments or questions pertaining to this document should be addressed to (b)(3);10 USC 424;(b)(6), AAWSA Program Manager, Defense Intelligence Agency, ATTN: (b)(3);10 USC 42 Bldg 6000, Washington, DC 20340-5100.

## Contents

1. Introduction .....	iv
2. Giant Magnetoresistance .....	1
2.1 GMR Basics .....	1
2.2 GMR Applications .....	3
3. Spin-Transfer-Torque .....	4
3.1 STT Basics .....	4
3.2 STT Experiments .....	7
3.3 STT Applications .....	10
3.4 STT-Driven Motion of Magnetic Domain Walls .....	12
4. Antiferromagnetic Metal Spintronics .....	12
4.1 Antiferromagnetic GMR .....	13
4.2 Antiferromagnetic STT .....	14
5. Summary and Conclusions .....	16
6. References .....	18

## Figures

Figure 1. In a Magnetic Multilayer, Several Atomic Layers of Magnetic Material Alternate With Layers of Nonmagnetic Material .....	1
Figure 2. Resistance of a Magnetic Multilayer R Versus Magnetic Field .....	2
Figure 3. Differential Resistance $dV/dI$ of a Mechanical Point Contact as a Function of Current for a Series of Magnetic Fields .....	4
Figure 4. Device Schematics for STT Experiments .....	5
Figure 5. Qualitative Picture of STT .....	6
Figure 6. Torques on a Magnetic Moment in a Magnetic Field and Subject to an Electrical Current .....	7
Figure 7. Spin-Torque-Driven Magnetic Switching .....	8
Figure 8. Oscillatory Voltage .....	9
Figure 9. Scanning Transmission X-ray Microscopy Images .....	10
Figure 10. Conventional MRAM Cell .....	11
Figure 11. Racetrack Memory Concept .....	12
Figure 12. Schematic of Point Contact to Sample Geometry .....	15

## **Metallic Spintronics**

### **1. Introduction**

The rapid pace of progress in the computer industry over the past 40 years has been based on the miniaturization of chips and other computer components. Further miniaturization, however, faces serious challenges—for example, increasingly high power dissipation. To continue on pace, the industry must go beyond incremental improvements and embrace radically new technologies. A promising nanoscale technology known as spintronics (a neologism for “spin-based electronics”) has emerged. Spintronics refers to the role an electron spin plays in solid-state physics. Spintronics researchers aim to develop a revolutionary new class of electronic devices based on the spin of electrons in addition to the charge. In spintronic devices, information is carried not by the electron's charge, as in conventional microchips, but by the electron's intrinsic spin. Changing the spin of an electron is faster and requires less power than moving it. Therefore, if a reliable way could be found to control and manipulate spins, spintronic devices could offer higher data processing speeds, lower electricity consumption, and many other advantages over conventional chips, perhaps including the ability to carry out radically new quantum computations.

Spintronics in ferromagnetic systems is built on a complementary set of phenomena in which the magnetic configuration of the system influences its transport properties and vice versa. Giant magnetoresistance (GMR) (Reference 1, 2) and spin-transfer-torque (STT) (Reference 3-5) phenomena exemplify such interconnections in multilayers composed of ferromagnetic (F) and nonmagnetic (N) layers. The physics and applications of metallic spintronics are discussed in this report from the perspective of these two phenomena. GMR, research on which was awarded the Nobel Prize in Physics in 2007, refers to a large change in resistance of magnetic multilayers when the relative orientation of magnetic moments in their constituent ferromagnetic layers is altered by an applied magnetic field. The inverse effect, STT, in which a large electrical current density  $j$  can perturb the magnetic state of a multilayer, has also been predicted (Reference 3, 4) and observed in experiments on current-induced reversal and precession of magnetization (Reference 5-9) and magnetic domain wall motion (Reference 10, 11).

Spintronics is a broad research field with (currently) three major subfields: (1) materials research that is attempting to create new materials that are both magnetic and semiconductors, (2) research on novel magnetotransport effects in ferromagnetic metals, and (3) research on techniques that can be used to manipulate individual electron spins. The first subfield is targeting magnetic semiconductors because devices based on such materials would be the easiest to integrate with the present semiconductor device technology and processing capabilities. However, despite extensive research, most semiconductor spintronic devices are still theoretical concepts awaiting experimental demonstrations. This report focuses on spintronics research in metallic systems within the scope of the second and third subfields. The second subfield has experienced an unprecedented period of new discovery over the past 20 years, including the discovery of GMR, and has already spawned major technological change in the information storage industry with the use of GMR sensors and read heads. The third subfield is vital for spintronic devices, as virtually any processing of information in such devices is associated with transport and manipulation of spins.

New and efficient methods for manipulating spins that stimulate active research programs in spintronics at a large number of academic institutions and a half-dozen industrial research labs around the world are highly desirable. The prize to be gained is active control and manipulation of spin distributions (magnetic moments) for new and improved functionality in electronic/spintronic devices. The confluence of intense basic science and industry interest in ferromagnetic metal spintronics has not occurred on this scale in physics in a long time.

The report is arranged as follows: Section 2 is dedicated to magnetotransport effects in magnetic systems where magnetic configuration can influence the system's transport properties. It discusses GMR in magnetic multilayers and related phenomena, highlights basic physical principles responsible for GMR, and describes technological applications of the effect. Section 3 focuses on the reverse connection between the system's magnetic configuration and its transport properties—the so-called STT effect. The physical origin and potential applications are discussed. Section 4 discusses other new directions in metallic spintronics, with a particular focus on spintronics with antiferromagnetic materials. Section 5 summarizes, with an eye to the future, the development of spintronic technologies and their aerospace applications.

## 2. Giant Magnetoresistance

### 2.1 GMR BASICS

This section discusses the phenomenon of giant magnetoresistance (GMR). Excellent reviews of GMR are available elsewhere (Reference 12-22). The focus on physical concepts important for the sections to follow are discussed.

GMR in magnetic multilayers refers to a dramatic reduction in the resistance of the multilayers when subjected to an external magnetic field. GMR's size is usually defined as the resistance change in magnetic field relative to its peak value. The effect can be distinguished from the ordinary magnetoresistance (MR) coming from the direct action of the magnetic field on the electron trajectories via the Lorentz force (Reference 23), and from the anisotropic MR, which comes from dependence of the resistivity on the relative orientation of magnetic moment to the current (Reference 24).

To prepare the magnetic multilayers, where several atomic layers of one (ferromagnetic) material alternate by layers of another (nonmagnetic) material (see Figure 1), a wide variety of deposition methods have been used, such as electrochemical deposition techniques (Reference 25, 26) and various vacuum deposition techniques (Reference 27, 28). The latter shares mainly between two methods using either sputter deposition or molecular beam epitaxy (MBE) systems. Sputter deposition involves knocking off the atoms of the material of interest from a target by particle bombardment, followed by the deposition of high-energetic atoms ( $\sim 2\text{-}30$  electronvolts [eV]) onto the substrate. A principal advantage of sputter deposition is the ease with which many different materials can be deposited at relatively high deposition rates. In contrast, deposition rates in MBE systems are usually much lower than for sputtering systems, but much lower energies ( $\sim 0.1$  eV) of the evaporated material make this technique favorable for growth of highly oriented single-crystalline films.

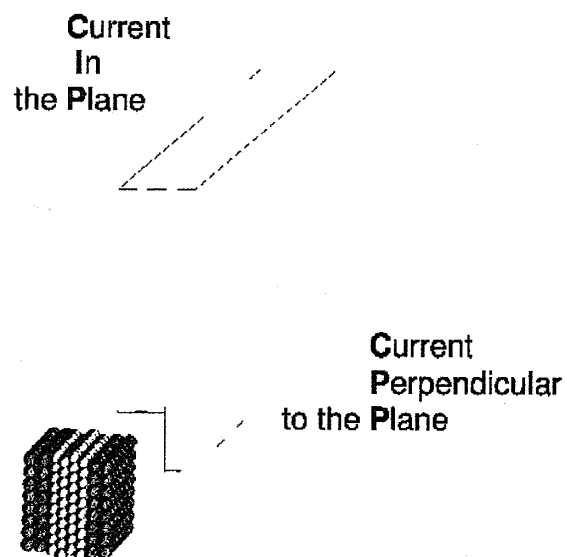


**Figure 1. In a Magnetic Multilayer, Several Atomic Layers of Magnetic Material (shown in grey) Alternate With Layers of Nonmagnetic Material (shown in white). GMR occurs in one of two different geometries: (1) when the current flows in the plane (CIP geometry) of the layers or (2) when the current flows perpendicular (CPP geometry) to the layers.**

The original observation of GMR (Reference 1) was made on MBE grown iron-chromium (Fe/Cr) multilayers with nearly perfect crystallinity. Subsequently, by using sputtered samples that are grown much more rapidly than MBE samples, it was possible not only to reproduce these results but also to observe oscillations in the magnetoresistance as the thickness of the nonmagnetic spacer layers was varied (Reference 29). Subsequent

studies (Reference 30) on sputtered cobalt-copper (Co/Cu) multilayers revealed magnetoresistances at room temperatures 3 to 4 times larger than those for iron-chromium and 13 times greater than those for the permalloy films that were used as magnetoresistive sensors in magnetic reading heads at that time. The much higher numbers observed in magnetic multilayers predetermined the fate of GMR in magnetic recording technology.

The current understanding is that GMR observed in magnetic multilayers arises from the dependence of the resistivity on their internal magnetic configuration and the role of the external magnetic field to change this configuration. Figure 2b illustrates GMR in the simple limit where the electron mean-free-path is much longer than the layer thicknesses. The electrical transport properties of the system are described in terms of the so-called two-current model (Reference 31), based on the suggestion by Mott (Reference 32) that, at temperatures lower than the Curie temperature, the spin-up and spin-down electrons will be almost independent and carry current in parallel. Electrons are much more strongly scattered by a magnetic layer if they and the local magnetization spin in opposite rather than the same direction ( $R > r$ ). For simplicity, the figure is drawn with scattering only at interfaces; however, there is also scattering within the layers. At zero magnetic field, where the magnetizations of adjacent magnetic layers are aligned antiparallel—for example, because of exchange coupling between the layers (Reference 29)—the spin-down electrons are weakly scattered in layer F1 but strongly scattered in F2. In contrast, the spin-up electrons are weakly scattered in layer F2 but strongly scattered in F1. As a result, two channels are equivalent, leading to a total resistance in this “antiferromagnetic” configuration  $R_{AF} = (R+r)/2$  (see the corresponding resistance circuit in Figure 2c).

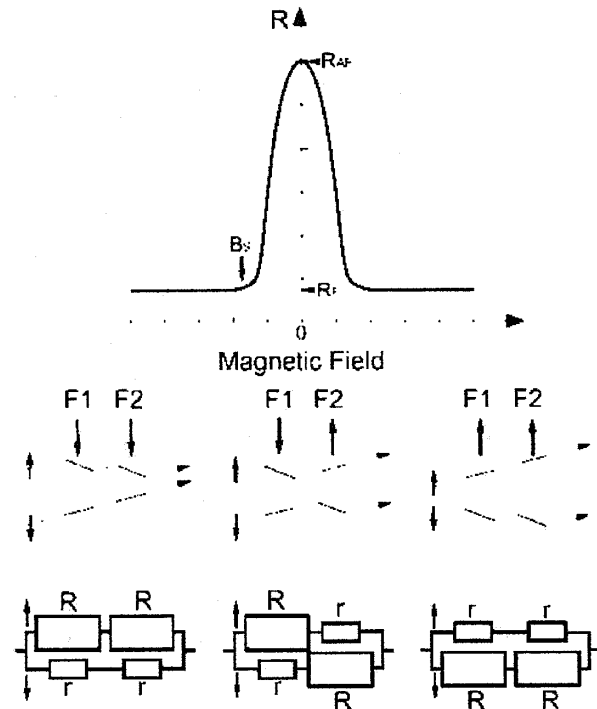


Figure 2. (a) Resistance of a magnetic multilayer  $R$  versus magnetic field. (b) Origin of GMR in terms of spin-dependent electron scattering: F1 and F2 are ferromagnetic layers with a nonmagnetic layer in between. At zero magnetic field, the magnetizations in F1 and F2 are aligned antiparallel (center panel) and can be switched to parallel orientation by an applied field. (c) The equivalent resistance circuits corresponding to the three magnetic configurations shown in (b). See text for details.

When the magnetizations of the two F layers are set into parallel configuration by an applied magnetic field, the spin-up electrons are weakly scattered in both layers and form a low-resistivity channel, whereas the spin-down electrons are strongly scattered in all the layers and form a high-resistivity channel. The reversal of magnetic field just interchanges the roles of spin-up and spin-down channels. The current's shunting by the low-resistivity channel produces a low total resistance  $R_F = 2Rr/(R+r)$  in this “ferromagnetic” configuration. The size of the GMR is defined as  $(R_{AF}-R_F)/R_{AF} = (R-$

$r^2/(R+r)^2 \leq 1$ . The other definition  $\Delta R/R = (R_{AF}-R_F)/R_F = (R-r)^2/4Rr$  (unbounded from above) is also in use. Figure 2a shows a magnetoresistance curve typical for magnetic multilayers. The resistance is constant at a minimum value  $R_F$  above a saturation field  $B_S$  (parallel  $F_S$ ) and rises to a maximum value  $R_{AF}$  as the applied magnetic field  $B$  approaches zero (antiparallel  $F_S$ ).

GMR occurs in two different geometries (see Figure 1): namely when the current flows in the plane of the layers, or CIP geometry, or when current flows perpendicular to the layers, or CPP geometry. Most of experiments on GMR are carried out in the CIP geometry because measuring the fairly large resistance of a thin film is quite easy (film length is typically orders of magnitude larger than its thickness). Experiments in the CPP geometry are more difficult (Reference 33) and require special techniques for precision measurements of very small resistances  $\sim 10^{-7}$ - $10^{-8}$   $\Omega$  resulting from the "short and wide" geometry of a 1-mm<sup>2</sup> "wide" and 1- $\mu$ m "long" sample. In order to increase the resistances to easily observable values, microfabrication techniques can be used to reduce the sample's cross-sectional area (Reference 34-36). Finally, a simple and inexpensive point-contact technique (Reference 37) may also be suitable for this purpose. The samples with a reduced cross-sectional area will be of interest for spin-transfer-torque experiments presented in Section 3.

## **2.2 GMR APPLICATIONS**

GMR is currently used in magnetic field sensors, including those in read heads for computer hard drives, in galvanic isolators, and in nonvolatile random access memory devices. Reading information stored on magnetic hard disk drives in computers was the first large-scale commercial application of GMR. The information is stored by magnetizing small regions (magnetic domains) of a magnetic recording disk in different directions. The stray magnetic fields from these domains are detected by a GMR sensing element called spin valve. The simplest type of spin valve consists of two ferromagnetic layers separated by a thin, nonmagnetic spacer. The spin-valve resistance is smallest when the magnetizations of the two ferromagnetic layers are parallel and largest when the magnetizations are antiparallel. The antiparallel alignment is achieved by making the two layers respond differently to an external magnetic field; an antiferromagnet in contact with one of the layers is used to effectively "pin" the magnetization in this layer through an effect called "exchange bias." The exceptional responsiveness of spin valves to magnetic fields has enabled very high areal packing densities in hard drives.

Other sensor applications using GMR elements include monitoring of a ferrous gear rotation in machinery operation (Reference 38) via detection of a changing magnetic flux when a gear tooth passes near the sensor, monitoring of electrical current via detection of the current-induced Oersted magnetic field, and transferring high-frequency signals between isolated circuits (Reference 39) via magnetic fields generated by a high-frequency inductor in one circuit and replicated in another circuit by a GMR sensor.

### 3. Spin-Transfer-Torque

This section focuses on the spin-transfer-torque (STT) phenomenon, which refers to a novel method to control and manipulate magnetic moments in nanostructures by spin currents—one of the forefront and most exciting areas in magnetism research today.

#### 3.1 STT BASICS

The previous section showed that the magnetic state of a ferromagnet can affect its electrical transport properties; for instance, the relative orientation of the magnetic moments in magnetic multilayers underlies the phenomenon of GMR (Reference 1, 2). The inverse effect, in which a large electrical current density can perturb the magnetic state of a multilayer, has also been predicted (Reference 3, 4). Here the current transfers vector spin between the magnetic layers and induces precession and/or reversal of the layer magnetizations. Altering the magnetic state with spin currents is based on quantum mechanical exchange interaction and represents a novel method of magnetization control on the nanometer length scale and the picosecond time scale.

The first observation of such a spin-transfer phenomenon in magnetic multilayers was recorded by Tsoi et al. (Reference 5) (see Figure 3). In this experiment, the spin-transfer-induced excitations were produced by injecting high-density electrical currents into a Co/Cu magnetic multilayer through a mechanical point contact. Point contacts smaller than 10 nanometers (nm) are formed when a sharpened Cu metal wire (tip) is carefully brought into contact with the multilayer. The extremely small cross-sectional area of such a contact makes it possible to achieve current densities in excess of  $10^{12}$  A/m<sup>2</sup>. Because of its extremely small size (<10 nm), point contact is a very efficient probe of electrical transport properties in extremely small sample volumes inaccessible with other techniques (for example, electron-beam-lithography patterning). The latter qualifies point contact as the smallest probe of STT today.

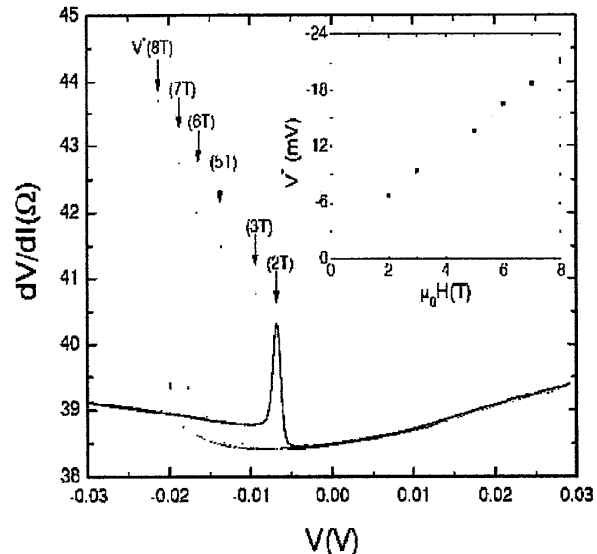


**Figure 3. Differential Resistance  $dV/dI$  of a Mechanical Point Contact as a Function of Current for a Series of Magnetic Fields.** The peak in  $dV/dI$  indicates the onset of SST excitations. The inset shows that the threshold current at the peak in  $dV/dI$  increases linearly with the applied field. (Reference 5)

The STT phenomenon currently attracts considerable attention because it combines poorly understood fundamental science questions with the promise of applications in a broad range of technologies. In high-speed, high-density magnetic recording technology, for instance, SST could replace the Oersted field currently used for writing magnetic bits in storage media (for example, in magnetic random access memory [MRAM]). This may lead to a smaller and faster magnetic memory. Another possible application is based on the spin-transfer-induced precession of magnetization, which



converts a direct current (dc) voltage input into an alternating current (ac) voltage output. The frequency of such a precession can be tuned from a few gigahertz (GHz) to > 100 GHz by changing the applied magnetic field and/or dc current, effectively resulting in a current-controlled oscillator for use in practical microwave circuits.

Since its prediction in 1996, the STT effect has been observed in a number of experiments, including those with mechanical (Reference 5, 9, 40) and lithographic point contacts (Reference 6, 41), manganite junctions (Reference 7), electrochemically grown nanowires (Reference 8), lithographically defined nanopillars (Reference 42, 43), tunnel junctions (Reference 44), and semiconductor structures (Reference 45). These different methods all share one characteristic feature: they make it possible to attain extremely high current densities ( $>10^{12}$  A/m<sup>2</sup> for metallic structures) needed to produce sufficiently large spin-transfer torques (Reference 3, 4). This is achieved by forcing the electrical current to flow through a very small constriction. The latter can be a mechanical point contact, a lithographically defined point contact or nanopillar, or a nanowire, as illustrated in Figure 4. In all cases, the maximum current density  $j_{\max} = I/A$  is defined by the current  $I$  flowing through the device and the minimum cross-sectional area  $A$  of the current path. For typical mechanical point contacts,  $I \sim 1$  mA and  $A \sim 100$  nm<sup>2</sup> gives  $j_{\max} \sim 10^{13}$  A/m<sup>2</sup>. In lithographically defined structures, both  $I$  and  $A$  are typically larger,  $I \sim 10$  mA and  $A \sim 10000$  nm<sup>2</sup>, that gives  $j_{\max} \sim 10^{12}$  A/m<sup>2</sup>.

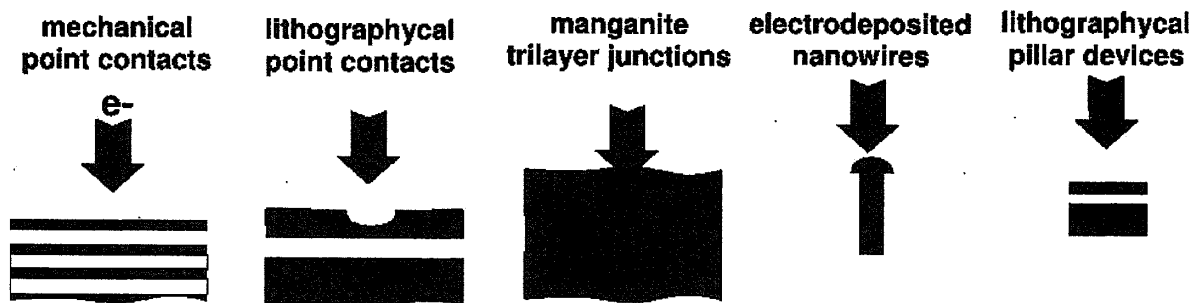


**Figure 4. Device Schematics for STT Experiments.** All experiments share one common feature: a small constriction for electrical current—that is, point contact, junction, nanowire, or nanopillar. Black (grey) indicates insulator; dark blue indicates magnetic material.

The basic physical mechanism underlying STT relies on conservation of angular momentum. Consider a pedagogically simple case where a conduction electron crosses an interface between a nonmagnetic metal (N) and a ferromagnet (F). We assume the initial state of the electron's spin  $S$  in N is noncollinear to the F's magnetization  $M$ . Once into F,  $S$  is subject to an exchange torque caused by  $M$  that tends to reorient  $S$ . Therewith, according to Newton's Third Law, there should also exist a reaction torque that acts on  $M$  – STT torque. Deep into F,  $S$  is aligned with  $M$ , and the change in angular momentum that occurs from its reorientation has been transferred to  $M$ . Hence the phenomenon's name: spin-transfer torque. Of course, the torque applied to  $M$  by a single-spin  $S$  is negligibly small owing to  $S$  being negligibly small compared with  $M$ . For high current density crossing the N/F interface, however, the number of such spins can be very large and the resulting effective  $S$  might become comparable to  $M$ . This highlights the need for high current densities to observe the STT phenomenon.

A typical experiment on current-driven excitation of a ferromagnet usually involves two single-domain thin-film magnets separated by a nonmagnetic spacer. Here one magnet

( $F_a$ ) is "hard" and used to polarize the current, while the spacer (N) is thin enough for the polarized current to get through and excite the second "free" magnet ( $F_b$ ). This  $F_a/N/F_b$  trilayer structure is similar to a GMR spin valve. The GMR effect can thus be used to monitor the orientation of  $F_b$  relative to  $F_a$  – GMR varies linearly with  $\cos\theta$ , where  $\theta$  is angle between magnetic moments of  $F_a$  and  $F_b$ , and a phenomenological description (Reference 46) gives the trilayer resistance  $R(\theta) = R_F + (R_{AF} - R_F) (1 - \cos\theta)/2$ . When current flows across  $F_a/N/F_b$ , the current-induced torques act on both  $F_a$  and  $F_b$  layers (Reference 3, 47). This is schematically illustrated in Figure 5. This qualitative picture of STT assumes both  $F_a$  and  $F_b$  layers are perfect spin filters, so that electron spins aligned with the magnetic moment of, for example,  $F_a$  layer are completely transmitted through the layer, while spins aligned antiparallel to the layer moment are completely reflected. When electron current crosses the  $F_b/N/F_a$  trilayer from right to left (Figure 5a), electrons transmitted through  $F_a$  will be polarized along  $F_a$ . If spin-diffusion length in N is long enough, this spin-polarized current will reach  $F_b$  and exert a torque on  $F_b$  in a direction so as to align  $F_b$  with  $F_a$ . Repeating the argument for  $F_b$ , we find that electrons reflected from  $F_b$  will be polarized antiparallel to  $F_b$  and, hence, in turn exert a torque on  $F_a$  trying to align  $F_a$  antiparallel with  $F_b$ . The net result is a pinwheel-type motion with both  $F_a$  and  $F_b$  rotating in the same direction (clockwise in Figure 5a), as described previously by Slonczewski (Reference 3). When the current crosses the trilayer from left to right, the directions of the torques are reversed (Figure 5b)—the torque on  $F_a$  is trying to align  $F_a$  parallel with  $F_b$ , while the torque on  $F_b$  is trying to align  $F_b$  antiparallel with  $F_a$ .

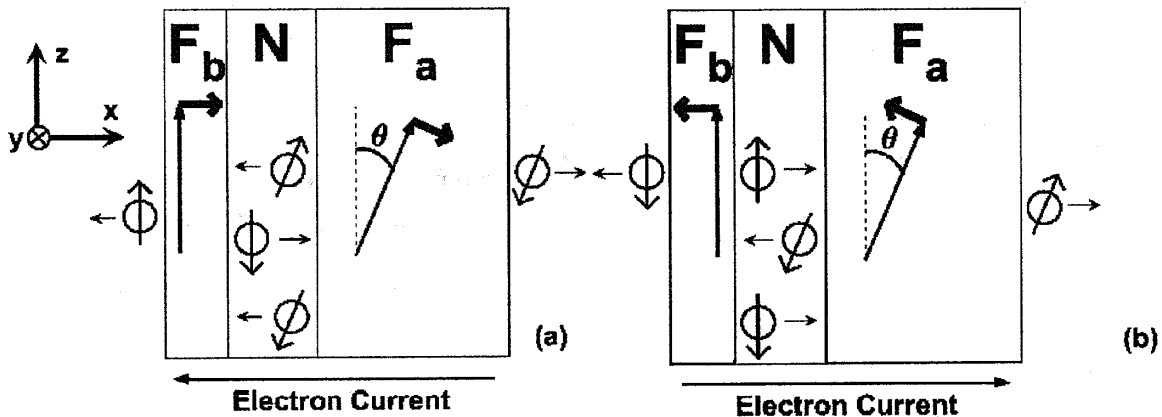


**Figure 5. Qualitative Picture of STT.** (a) For left-going electrons magnetic moments (thin arrows) of both  $F_a$  and  $F_b$  are rotated clockwise. (b) For right-going electrons the directions of the torques (thick arrows) on  $F_a$  and  $F_b$  are reversed. (Reference 47)

The above discussion implies the asymmetry of STT with respect to current direction as follows. Let's fix the orientation of the polarizer  $F_a$ ; in experiments this is usually accomplished by making  $F_a$  very thick (compared with  $F_b$ ) or by pinning its orientation with an adjacent antiferromagnetic layer via the phenomenon of exchange bias. If initially  $F_b$  is almost parallel with  $F_a$ , the left-going electrons will stabilize this parallel alignment, and no STT excitation is present. When current bias is reversed, the torque on  $F_b$  will try to rotate  $F_b$  away from  $F_a$  and will result in STT excitation of the system. This asymmetry with respect to current polarity is one of the main features of STT in experiments; see, for instance, Figure 5, where STT excitations are present only at negative bias.

### 3.2 STT EXPERIMENTS

Section 3.1 introduced the physics of STT in magnetic nanosystems. We have seen that a high-density electrical current can result in torques on magnetic elements of the system. These torques may be used to control and manipulate the system's magnetic state. However, the resulting behavior of the system can differ significantly from case to case, depending on particular conditions of observation. For instance, in modest external magnetic fields, magnetization of a small element can be repeatedly reversed between two stable configurations, while at higher fields, where the reversal is energetically unfavorable, the moment can be set into precession at a very high frequency. To understand details of what happens with a magnetic moment  $\vec{S}$  in a particular situation, one can use Newton's Second Law.

For  $\vec{S}$  this would be the Landau-Lifshitz-Gilbert equation, where the rate of change of  $\vec{S}$  is set equal to the net torque acting on  $\vec{S}$ :

Equation 1: 
$$\frac{d\vec{S}}{dt} = \gamma \vec{S} \times \vec{B}_{eff} - \frac{\alpha}{|\vec{S}|} \vec{S} \times \frac{d\vec{S}}{dt} + \eta I \frac{\mu_B}{e} \vec{s} \times (\vec{s}^* \times \vec{s})$$

Here the first term on the right is the torque on a magnetic moment  $\vec{S}$  in an effective magnetic field  $\vec{B}_{eff}$ , (including applied, demagnetizing, anisotropy, and other fields), with  $\gamma$  the gyromagnetic ratio; the second term is a phenomenological damping term introduced by Gilbert, with  $\alpha$  the Gilbert damping parameter; the third term is the SST where small  $\vec{s}$  and  $\vec{s}^*$  are unit vectors along  $\vec{S}$  and the polarizer  $\vec{S}^*$ ,  $I$  is the current,  $\mu_B$  is the Bohr magneton,  $e$  is the electron charge, and  $\eta$  is the spin-polarization factor.

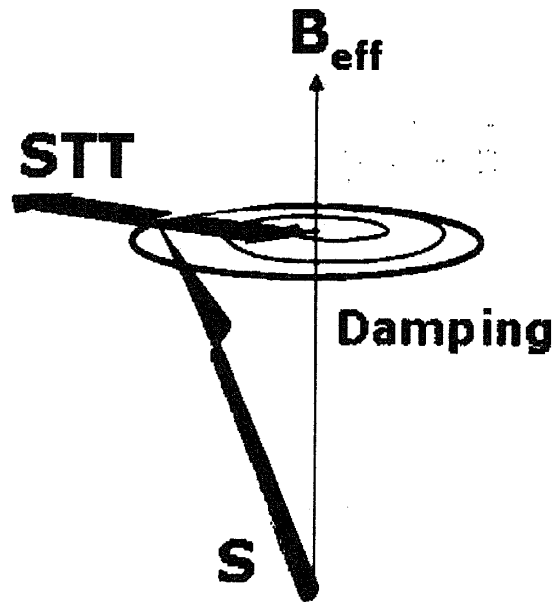


**Figure 6. Torques on a Magnetic Moment in a Magnetic Field and Subject to an Electrical Current**

The diagram in Figure 6 shows the directions of the three torques from Equation 1. Note that, depending on the polarity of applied current, the STT torque can be either in the same or opposite direction as the damping torque. In the former case, STT will effectively result in an increased damping for any magnitude of the applied current and suppress any possible excitations of  $\vec{S}$  from its equilibrium state along  $\vec{B}_{eff}$ . If, however, the STT torque is opposite to the damping, we can distinguish two situations. For currents below a critical current, where STT is small compared with damping,  $\vec{S}$  spirals toward  $\vec{B}_{eff}$  (red trajectory in Figure 6). For

currents larger than the critical current, STT exceeds the damping torque and causes  $\vec{S}$  to spiral away from  $\vec{B}_{eff}$ , with a steadily increasing precession angle. The ultimate result can be either stable steady-state precession of  $\vec{S}$  around  $\vec{B}_{eff}$  (black trajectory in Figure 6) or magnetic reversal of  $\vec{S}$  into a state antiparallel to  $\vec{B}_{eff}$ , depending on the angular dependence of STT and damping torques.

Almost all experimental observations of STT rely on the GMR phenomenon to detect the current-induced reorientation of magnetic moments in nanodevices. Typical measurements include (1) measuring static device resistance  $R=V/I$  as a function of applied dc bias current  $I$  in an applied magnetic field  $\vec{B}$  and (2) measuring  $R$  versus  $\vec{B}$  at a constant  $I$ . Figure 3 shows how the differential resistance  $dV/dI$  of a Cu point contact to Co/Cu magnetic multilayer varies with the bias voltage  $V$  (equivalent to  $I$ ) applied across the contact. Here the multilayer magnetic moments are saturated out of the plane of the layers by a sufficiently large external magnetic field ( $B \geq 2T$ ). The onset of STT-driven magnetic precession is revealed by a peak in differential resistance of the contact. The peak in  $dV/dI$  indicates the transition into precession is a reversible process, and in a small range of currents, one can continuously increase or decrease the angle of precession. However, other scenarios are also possible—for example, fast transitions between static and steady-state precession states with current-dependent dwell time.

If the applied magnetic field is small, the magnetic system can have more than one low-energy state. In the simple case of a magnetic element with uniaxial anisotropy, STT can trigger a transition between two static states that are energetically favorable. An example of such behavior is shown in Figure 7. Here the current is driven across a trilayer Py20nm/Cu12nm/Py4.5nm spin-valve structure patterned by electron beam lithography into a nanopillar with a  $40 \times 120 \text{ nm}^2$  cross-sectional area (Reference 48). The differential resistance of the nanopillar exhibits a hysteresis as a function of an applied bias current as the magnetization of the thin (free) permalloy (Py) layer is aligned parallel and antiparallel to the thick (hard) Py layer by the current.

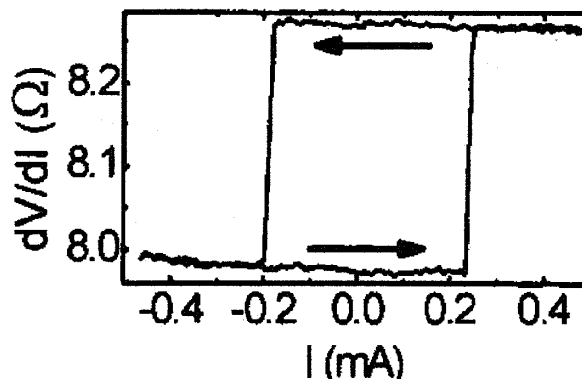


Figure 7. Spin-torque-driven magnetic switching for a Py20nm/Cu12nm/Py4.5nm spin valve with a  $40 \times 120\text{-nm}^2$  cross-sectional area, as the magnetization of the thin (free) magnetic layer is aligned parallel and antiparallel to the thicker magnetic layer by an applied current. (Reference 48)

The two examples presented above (Figures 3 and 7) demonstrate how simple dc resistance measurements can be used for STT observation. Here the measured resistance of a device provides indirect information about the relative orientation of magnetic elements in the device. However, measured critical currents highlighted by sharp variations in the resistance remain the only experimental information that can be used to quantitatively compare theory and experiment. Moreover, the dc measurements in Figure 3 provide no information about fast evolution of magnetization in the device

associated with high-frequency precession of magnetic moments. High-frequency techniques must be employed to provide such capabilities, as discussed next.

The first experiment providing unequivocal evidence that a dc electrical current can result in high-frequency (tens of GHz) precession of magnetic moments was reported by Tsoi et al. in (Reference 9). Here an STT device—point contact—was placed in a microwave cavity of a high-frequency, high-field electron spin resonance (ESR) spectrometer. This arrangement allowed performing dc transport experiments, such as those described above, while the contact was irradiated with high-frequency microwaves. When the frequency of external microwaves matched the precession frequency excited by the dc current, an additional (rectified) voltage was detected across the contact. By detecting this voltage while varying the external frequency, field, and applied current, Tsoi et al. (Reference 9) were able to map the frequency excited by dc current as a function of applied field and current. In a more recent experiment, Rippard et al. (Reference 49) fed microwaves to a point contact via electrical leads and reported observation of a similar dc response.

Finally, the high-frequency dynamics of the free-layer magnetization can be measured directly by detecting high-frequency oscillations in voltage across a spin valve under dc current. Here the hard magnetic layer is fixed, while the free layer exhibits a high-frequency precession relative to the hard layer. GMR results in a high-frequency modulation of the spin-valve resistance, which in turn leads to a high-frequency component of the voltage across the spin valve traversed by a dc current. This voltage can be directly probed with a high-frequency spectrum analyzer, as was recently done by Kiselev et al. (Reference 50) and by Rippard et al. (Reference 41). Moreover the voltage oscillations owing to spin-torque-driven magnetic precession can be directly measured in time domain using a sampling oscilloscope (Reference 51), as illustrated in Figure 8.

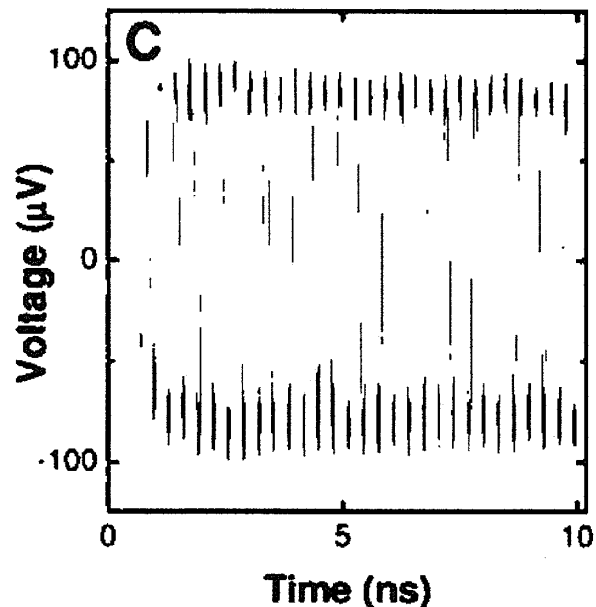


**Figure 8. Oscillatory Voltage Generated by Precessional Motion of the Free Magnet in IrMn8nm/NiFe4nm/Cu8nm/NiFe4nm Nanopillar, in Response to a 335-mV dc Voltage Step Applied to the Device at  $B = 630$  Oersteds (Reference 51)**

The above examples illustrate how broadband instrumentation for measuring voltage in GMR devices may provide important and often unique information about high-frequency magnetic dynamics driven by spin-transfer torques. However, the detailed understanding of STT is still the subject of debate and requires new experimental techniques capable of probing magnetization dynamics on nanometer length scales and sub-nanosecond time scales. In principle, this can be accomplished by the use of synchrotron x-rays that were recently shown (Reference 52) to probe interfacial phenomena and directly image the time-resolved response of magnetic nanostructures to sub-nanosecond magnetic field pulses (Oersted switching) and spin-polarized current

pulses (STT switching). Figure 9 shows scanning transmission x-ray microscopy (Reference 53) images of in-plane components of magnetization  $M$  –  $M_x$  in panel (a) and  $M_y$  in panel (b)—in the free CoFe layer (indicated by blue ellipse) of a  $100 \times 150$ -nm<sup>2</sup> magnetic nanopillar. The images were obtained by scanning a focused (diameter  $\sim 30$  nm) circularly polarized x-ray beam across the CoFe layer, with the photon energy tuned to the characteristic Co L3 resonance to provide magnetic contrast through the x-ray magnetic circular dichroism effect (Reference 54), and by monitoring transmission of the x-rays as a function of the position  $x, y$  with a fast avalanche detector. The  $M$ -vector field of the free layer can be reconstructed from the measured  $M_x$  and  $M_y$  components as illustrated in Figure 9c, and the ultrafast x-ray microscopy technique provided a means to monitor this field as a function of time with  $\sim 100$ -picosecond resolution. The spatial resolution of the technique is set by the spot size of the x-ray beam ( $\sim 30$  nm) and currently limits its application to spintronic devices  $> 100$  nm in size (Reference 52). Potentially, however, technical development of the ultrafast x-ray microscopy may lead to an ultimate technique for STT studies that can probe the  $M$ -vector field on the nanometer length scale with picosecond time resolution.

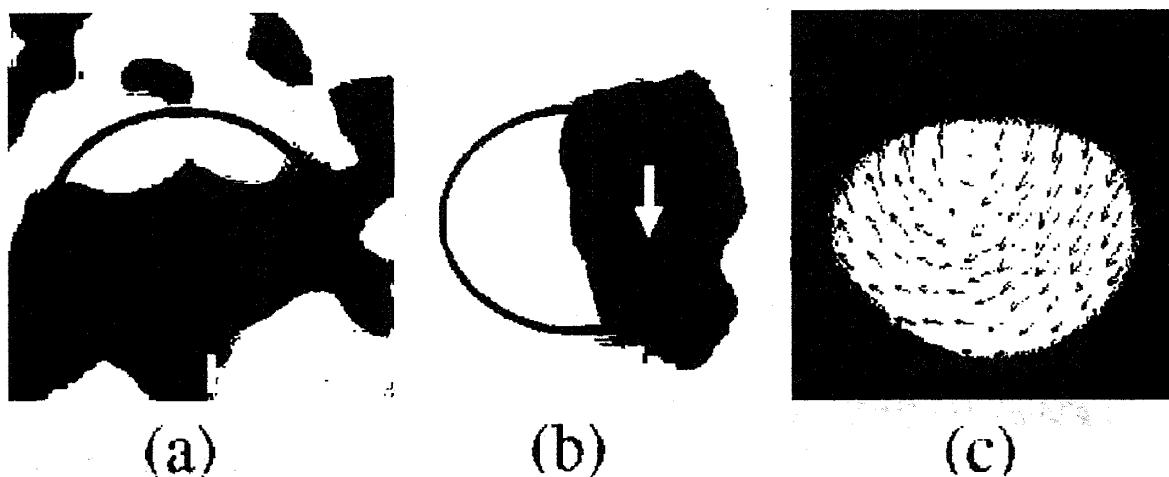


**Figure 9. Scanning transmission x-ray microscopy images of  $M_x$  (a) and  $M_y$  (b) components of magnetization  $M$  combine into the vector field (c), which represents the direction of  $M$  in the plane of the CoFe free layer. (Reference 52)**

### 3.3 STT APPLICATIONS

The STT method to manipulate magnetic moments by an electrical current offers unprecedented spatial and temporal control of spin distributions and attracts considerable attention because of its potential application in a broad range of technologies. The perspective of STT for GHz communication applications and in magnetic recording technology is discussed.

The STT application in high-frequency technologies is based on the spin-transfer-induced precession of spins. The previous section discussed how precession of magnetization in GMR devices can convert a dc current input into an ac voltage output. The frequency of this output can be tuned from a few GHz to  $> 100$  GHz by changing the applied magnetic field and/or the dc current, effectively resulting in a current-controlled oscillator for use in practical microwave circuits. Hence, the STT effect in

GMR structures provides a means to engineer a nanoscale high-frequency oscillator powered and tuned by dc current. Such an oscillator could have frequency characteristics spanning more than 100 GHz and perhaps into terahertz range. Linewidths as narrow as 2 megahertz were demonstrated (Reference 55), leading to quality factors over 18,000. Potential applications for such high-frequency sources include integrated transceivers for wireless and wired applications, as well as wireless and wired chip-to-chip and on-chip communications. For the latter, logic circuits with a spin wave bus were proposed (Reference 56, 57) as an interface between electronic circuits and integrated spintronics circuits. Here spin waves are used for information transmission and processing, and the STT effect can provide a means for efficient spin-wave generation on the nanoscale.

In high-speed, high-density magnetic recording technology, STT could replace the Oersted field currently used for writing magnetic bits in storage media (for example, magnetic random access memory [MRAM]), thus leading to smaller and faster magnetic memory. Figure 10a schematically shows a bit cell of a conventional MRAM. The bit state is programmed to a "1" or "0" by switching between the parallel and antiparallel states of a GMR-like storage element. The first-generation MRAM utilizes magnetic tunnel junctions (MTJ) as storage elements because of their higher magnetoresistance ratios and impedance-matching constraints. However in scaling MRAM to small dimensions, the same constraints are expected to drive a transition from MTJs to fully metallic spin-valve storage elements. The switching between "1" and "0" states (writing) relies on magnetic reversal of the MTJ's free layer, achieved by passing electrical currents down the "bit" and "write" lines, that generates a sufficiently strong magnetic field at their intersection (that is, for a given MTJ). However, as the spatial decay of this Oersted field is rather slow ( $\sim 1/r^2$ ), it may affect neighboring cells. This makes scaling of MRAM to small dimensions questionable.

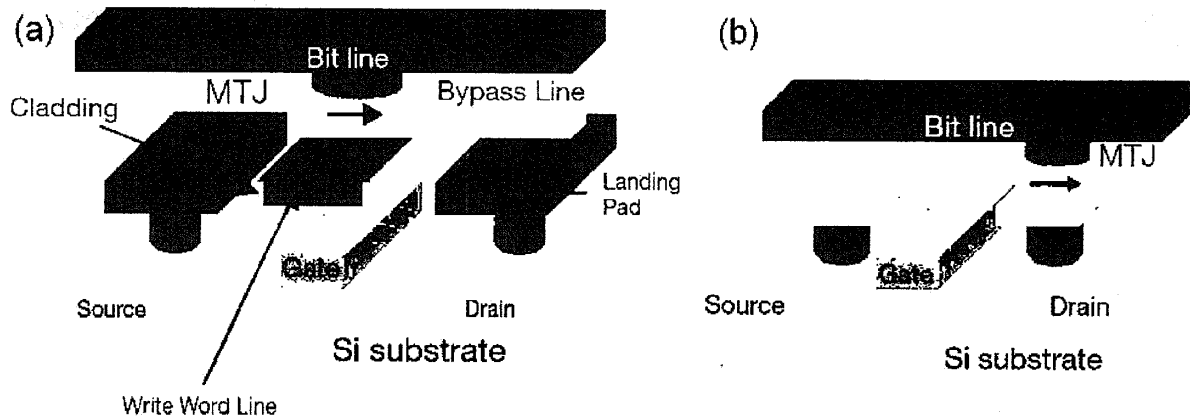


Figure 10. Conventional MRAM Cell (a) Versus STT MRAM Cell (b) (Reference 58)

STT MRAM (see Figure 10b) removes the constraints on scalability. Here the switching of the free layer magnetic moment is achieved by STT switching when a high-density electrical current is driven directly through the storage element (MTJ or spin valve). This writing is thus performed at high current levels, while the reading (measuring the resistance of the element) is done at low currents. Since STT MRAM eliminates the need for "write" and "bypass" lines, a more compact memory can be realized.

### 3.4 STT-DRIVEN MOTION OF MAGNETIC DOMAIN WALLS

Yet another manifestation of STT in metallic ferromagnets is a motion of magnetic domain walls traversed by an electrical current. The original prediction of the effect dates back to 1978, when Luc Berger predicted that a spin-polarized current should apply a torque to a magnetic domain wall (Reference 59). In a series of remarkable but only recently appreciated works, Berger set the theoretical (Reference 59-62) and experimental (Reference 63-65) groundwork for current-induced domain wall motion (CIDWM), which is now documented in materials ranging from magnetic semiconductors (Reference 66) to perpendicular-anisotropy superlattices (Reference 67). But the most widely studied materials by far have been metallic ferromagnets (Reference 10, 11, 68-82), including Py ( $\text{Ni}_{81}\text{Fe}_{19}$ ), CoFe, and Co, because of their decades-long ubiquity in magnetic storage technology.

The CIDWM effect can be qualitatively understood on the basis of the following arguments. Consider an electrical current flowing between two magnetic domains (A and B) with opposite magnetizations and, thus, traversing a 180-degree magnetic domain wall. The situation is similar to that of a single N/F interface discussed in Section 3.1. While in domain A, spins of conduction electrons are preferentially aligned with the magnetic moment of A. Once into domain B, the spins reverse to align with the moment of B. In reversing the electron spins, magnetic moments in the domain wall experience a torque associated with the change in angular momentum that occurs from the rotation of electrons spins. This spin-transfer torque can move the domain wall in the direction of the electron flow.

Moving magnetic domain walls with current was proposed as the basis for a new type of magnetic memory called "racetrack" (Reference 83). In contrast to today's hard disk drives (HDD), which rely on spinning motion of a disk to move their magnetic regions where the data is stored past a read head, the racetrack memory exploits the idea of moving magnetically stored data electronically. Figure 11 illustrates the concept of the racetrack. The racetrack is a ferromagnetic nanowire, with data encoded as a pattern of magnetic domains along the wire. Current pulses can move the entire pattern along the wire. The two cartoons of Figure 11a

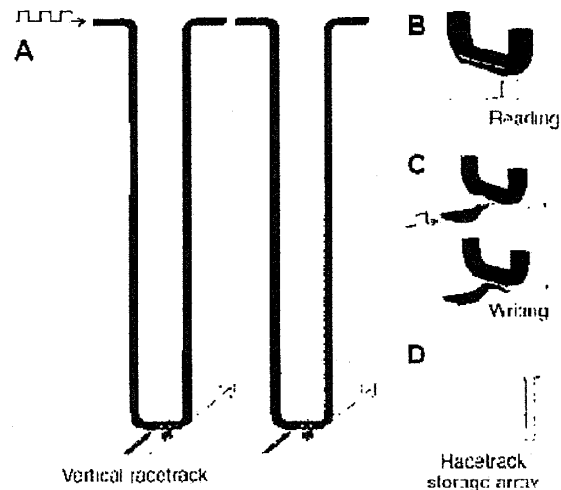


Figure 11. Racetrack Memory Concept. (Reference 83)

show the domain wall patterns in the racetrack before and after they have moved past read and write elements. Reading is achieved by measuring the resistance of a tunnel junction element connected to the racetrack (Figure 11b); writing (Figure 11c), by applying local magnetic fields—for example, the fringing fields of a domain wall moved in another nanowire. If U-shaped nanowires are placed normal to the plane of a chip and arranged into high-density arrays of racetracks (Figure 11d), the resulting storage density can be higher than that in solid-state memory devices like flash RAM and



similar to conventional HDDs; but the racetrack memory would have much higher read/write performance than HDD.

#### 4. Antiferromagnetic Metal Spintronics

Recently, MacDonald and coworkers (Reference 84) predicted that effects similar to GMR and STT observed with ferromagnets ought to occur in multilayer systems where the ferromagnetic (F) components are replaced by antiferromagnets (AFM). First, they predicted that the resistance of an AFM spin valve—where two AFM layers are separated by an N spacer—could depend on the relative orientations of the magnetic moments in the two AFM layers (antiferromagnetic GMR = AGMR). Second, they predicted that injecting a sufficiently strong current density into an AFM should affect its magnetic state via current-induced spin torque. These new AFM effects could lead to new all-AFM spintronics where AFMs are used in place of Fs.

Replacing F metals with AFM metals in a spintronic device has several advantages. While AGMR of an AFM spin valve was predicted (Reference 84) to be similar in magnitude to GMR in standard F spin valves, the critical current needed to alter the magnetic order in AFMs can be smaller than for Fs, partly because spin torques can act through the entire AFM volume. The estimate of the necessary current density  $j \sim 10^9$  A/m<sup>2</sup> (Reference 84) was less than the typical  $j \sim 10^{11}$  A/m<sup>2</sup> needed to reverse the magnetic order in F/N/F multilayers (Reference 5-9, 40-43, 48-51). Finally, using AFM metals in spintronic devices in place of F metals would eliminate unwanted effects of shape anisotropy on the magnetic stability of small elements, thus potentially offering better control of the magnetic state in nanoscale systems and easing fabrication requirements.

Following the original predictions of MacDonald and coworkers (Reference 84), Xu et al. (Reference 85) calculated the AGMR for a simple AFM/N/AFM/N = FeMn/Cu/FeMn/Cu multilayer, and Gomonay and Loktev (Reference 86) provided additional theoretical evidence that polarized current can destabilize the equilibrium state of an AFM. Note, however, that all calculations to date are for perfect samples and depend on quantum coherence. It is known that disorder can reduce the predicted effects. Experiments are thus crucial to see if any such effects are visible in real samples.

##### 4.1 ANTIFERROMAGNETIC GMR

To the author's knowledge, the only experimental study searching for AGMR was performed by Wei et al. (Reference 87). They have measured current-in-plane (CIP) and current-perpendicular-to-plane (CPP) magnetoresistances (MR) of magnetic multilayers containing two antiferromagnetic layers separated by a nonmagnetic layer. Such an antiferromagnetic spin valve, AFM/N/AFM, was predicted (Reference 84) to exhibit AGMR similar to GMR seen in ferromagnetic spin valves, F/N/F, containing two ferromagnetic layers separated by a nonmagnetic layer. Note, however, that calculations (Reference 84) assumed ballistic transport in samples with perfect layers and interfaces where AGMR is a consequence of quantum interference effects. Thus, any disorder that produces diffusive scattering and weakens quantum interference will weaken any such AGMR.

In F/N/F trilayers, the relative orientation of the magnetizations of the two Fs is controlled by an externally applied magnetic field B. To achieve well-defined antiparallel and parallel states of the two F layers, the moment of one F is often "pinned," via exchange coupling (exchange bias) to an adjacent AFM layer (Reference 88, 89), leaving the moment of the other free to reverse in much smaller B. In a simple AFM/N/AFM sample, just applying a field B is not expected to be efficient because of the weak effect of external fields on magnetic moments in AFMs. To achieve better control of the AFMs, AFM/N/AFM spin valves can be sandwiched between two F layers to give F/AFM/N/AFM/F, with the two AFM layers differently exchange-coupled to their respective F neighbors. Applying a magnetic field to change the magnetic order of the F layers should then also affect the order of the AFM layers. In addition to AFM/N/AFM and F/AFM/N/AFM/F multilayers, Wei et al. (Reference 87) have studied a variety of structures—F/AFM/N/AFM, AFM/F/N/AFM, F/AFM, and single F and AFM layers—to isolate the MR observations of interest from potential spurious effects.

For small applied currents, neither standard current-in-plane (CIP) MR measurements on extended multilayer films nor CPP MR measurements with point contacts showed any MRs for samples of all types. For larger applied currents, small positive CPP MRs (resistance is highest at saturation) were sometimes observed in samples with at least one F layer, while no MR was seen in samples with no Fs. These observations suggest sputtered AFM/N/AFM multilayers do not show AGMR, possibly owing to mostly diffusive transport in such imperfect films. Small MRs observed at higher currents in films with F layers may be associated with the suppression at high currents of spin accumulation induced within and around Fs (Reference 90). Further studies on high-quality films are still needed to verify any possible existence of AGMR in such structures.

#### **4.2 ANTIFERROMAGNETIC STT**

Stimulated by the theoretical studies in (Reference 84-86), four experimental searches for effects of STT on AFMs have been published so far (Reference 91-94), all working with exchange-biased spin-valves (EBSVs) of the form AFM/F1/N/F2. Here the AFM lies outside the "active" GMR region of the two F layers and serves mainly to "pin" the magnetization of the adjacent F2 layer to a higher reversing (switching) field than that of the "free" F1 layer, leaving the F1 layer free to rotate at a lower field. The pinning is produced either by heating the sample to above the blocking temperature of the AFM, applying a magnetic field, and then cooling to room temperature with the field on or by applying a magnetic field during sample growth. Wei et al. (Reference 91) used a point contact to inject a high dc current density  $j \sim 10^{12}$  A/m<sup>2</sup> approximately CPP into an EBSV film. Urazhdin and Anthony (Reference 92) sent a dc CPP current density  $j \sim 5 \times 10^{11}$  A/m<sup>2</sup> into electron-beam-lithography-fabricated nanopillar EBSVs. Tang et al. (Reference 93) sent a dc current-in-plane (CIP) current density  $\sim 10^{10}$  A/m<sup>2</sup> into an EBSV film with a metallic AFM. Dai et al. (Reference 94) sent an ac CIP current density  $j \sim 10^9$  A/m<sup>2</sup> into an EBSV film with an insulating AFM. In all of the studies (Reference 91-94), it was found that a sufficiently high bias current can influence the magnetic reversal of the "pinned" F1 layer. As the pinning (exchange bias) is known to be associated with interfacial AFM moments (Reference 88, 89), this observation can be taken as evidence of effects of the current on the AFM predicted in (Reference 84-86), given that other spurious effects (for example, Joule heating) can be ruled out.

The original observation of the effect was reported by Wei et al. (Reference 91), who measured magnetoresistance of a point contact to EBSV film at room temperature ( $\sim 295\text{K}$ ) with negative current flowing from the contact tip into the film. The sample geometry is shown in Figure 12a. A point contact is used to inject a dc current into a sputtered N/F1/N/F2/AFM/N = Cu(50 or 100nm)/CoFe(3 or 10nm)/Cu(10nm)/CoFe(3 or 10nm)/FeMn (3 or 8nm)/Au(5nm) multilayer (or inverted versions thereof—that is, Cu/FeMn/CoFe/Cu/CoFe/Au). The sample is heated to  $\sim 450\text{K}$  (above the blocking temperature of FeMn) and then cooled in a magnetic field of 180 Oersted to exchange-bias the "pinned" layer F2 to a higher magnetic field than needed to reverse the "free" layer F2. The top layer is covered by a 5-nm-thick layer of Au to protect it from atmospheric contamination. The magnetic field  $H$  is applied in the plane of the layers and along the direction of exchange bias. Magnetic coupling between the two F layers should be negligible, because the N layer is thick enough (10 nm) to eliminate exchange coupling, and the two F layers are wide enough ( $\sim \text{mm}$ ) to minimize dipolar coupling. The bottom N layer is Cu, made thick enough (50 or 100 nm) to approximate an equipotential, thereby generating an approximately CPP current flow through the F1/N/F2/AFM EBSV.

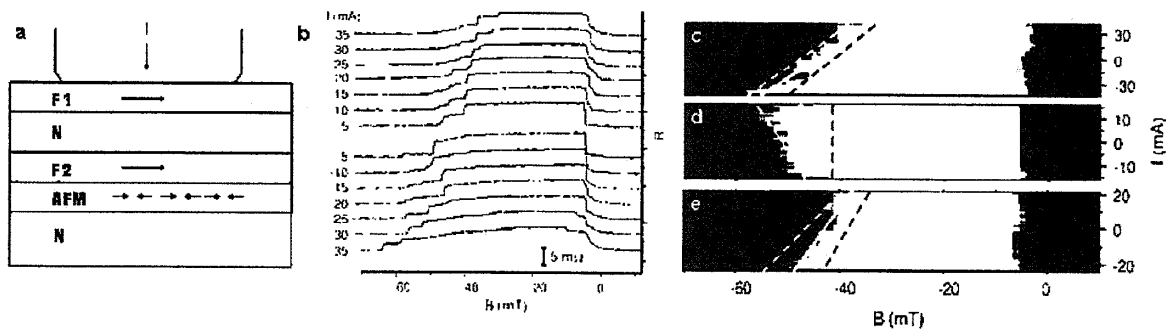


**Figure 12. (a) Schematic of point contact to sample geometry. Omitted is a 5-nm-thick protective Au capping layer between the point contact and the multilayer. The bottom N layer is also much thicker than shown to help produce a nearly CPP current. (b)  $R$  (vertical scale) versus applied magnetic field  $B$  for a series of currents  $I$ . The solid black curves are hysteresis curves starting from large positive  $B$  and finishing at large negative  $B$ . The grey curves start at large negative  $B$  and finish at positive  $B$ . In the dark curves, the "free" layer, F1, switches at  $\sim -5$  mT and the pinned layer, F2, switches at fields ranging from below  $-40$  mT (large positive  $I$ ) to about  $-60$  mT (large negative  $I$ ). (c-e) Grey-scale plots of  $R$  versus  $B$  for different values of  $I$ . White is maximum  $R$  (antiparallel state) and black is minimum  $R$  (parallel state). Lines are linear fits to the data at 30 percent (dashed white), 50 percent (solid white) and 70 percent (dashed black) of maximum  $R$ . Sample (c) is the sample of (b), with the AFM layer on the bottom (furthest from the point contact). Sample (d) is similar to (c), except inverted, so that the AFM layer is on top (closest to the point contact). Sample (e) differs from (b) only in that it has two equally thick (8-nm) F layers. (Reference 91)**

Figure 12b shows magnetoresistance curves for a series of currents  $I$  applied to a point contact with resistance  $R = 0.92 \Omega$ . The dark curves show sweeps from positive to negative field, and the lighter curves show sweeps back down from negative to positive field. For this contact,  $I = 30$  mA corresponds to  $j \sim 2 \times 10^8$  A/cm<sup>2</sup>. For dark curves, a large positive field  $+B$  along the pinning direction causes the moments of both the "free" and "pinned" F layers to point along  $+B$ , producing the minimum resistance  $R_P$  in this parallel orientation of the two Fs. Reducing the magnitude of  $B$ , the "free" F2 layer reverses at a small-magnitude negative  $B$ , giving the maximum resistance  $R_{AP}$  in antiparallel configuration. Finally, a larger magnitude negative  $B$  breaks the exchange-bias pinning of the "pinned" F1 layer, and its moment rotates to along  $-B$ , returning the

sample to  $R_P$ . For lighter curves of back-sweeps (Figure 12b), the measured resistance follows these changes in reverse order.

Focusing on the dark curves, we see that the switching field of the free layer F1 is essentially independent of the magnitude of  $I$  and shows little broadening. In contrast, the switching field of the pinned layer F2 broadens significantly as the magnitude of  $I$  increases, and the midpoint of the switching also shifts with  $I$ , increasing for  $-I$  and decreasing for  $+I$ . Similar behaviors are seen also in the lighter curves. Opposite shifts for  $+I$  and  $-I$  indicate these shifts cannot be due to Joule heating, which should cause shifts in the same direction for both directions of  $I$ . But Joule heating might contribute to the broadening of the switching transitions. The shifts of the dark curves are specified more clearly in Figure 12c, which shows grey-scale plots of the heights of the curves in Figure 12b, with white representing the antiparallel state of maximum resistance, and black the parallel state of minimum resistance. Data for three representative contacts (out of 29) on three different samples show that the behavior of interest is not limited to a single sample or contact, and that similar results are generally obtained for straight line fits to 30 percent (white dashed lines), 50 percent (solid white lines), and 70 percent (solid black lines) of the maximum change in  $R$ . The sample in Figure 12d is a contact with  $R = 1.6 \Omega$  to an inverted version of the sample in Figures 12b and c, so that the "directions" of currents are reversed. The sample in Figure 12e has equal thickness  $F1 = F2 = 3\text{-nm}$  layers. All three samples show the same features—that is, electrons passing through F2 into the AFM layer enhance pinning, and electrons passing through the AFM layer into F2 reduce it. Similar to the case of AFM=CoFe, a negative current density  $\sim 10^{12} \text{ A/m}^2$  injected through the F=CoFe into an AFM=IrMn/CoFe interface (Reference 95, 96) was found to increase the exchange bias, while a positive current decreased it.

Wei et al. (Reference 91) proposed the following qualitative explanation for these asymmetric changes in switching (exchange bias) field with current. Near the switching field, the metastability of F2's opposite to field orientation is due almost entirely to exchange interactions with uncompensated moments in the surface layer of the antiferromagnet. Some of these spins are pinned, thereby inducing an energy barrier for ferromagnetic layer spin reversal (Reference 88, 89). Electrons flowing from F2 into AFM induce torques on moments in the AFM matrix, altering its magnetic configuration (Reference 84). These STT torques tend to favor parallel alignment of moments at the F2/AFM interface and will therefore tend to increase the exchange bias field. Electrons flowing in the opposite direction will tend to have the opposite effect. The observed variations in exchange bias mediated by an electrical current thus can be taken as good evidence of the STT effect in AFM. However, such transport measurements do not distinguish between effects of the current on the bulk AFM and those on interfacial AFM moments, and more elaborate techniques are needed to obtain a detailed understanding of the phenomenon.

## 5. Summary and Conclusions

The semiconductor industry has distinguished itself by a long-term trend known as Moore's law (Reference 97) that foresees an exponential increase in transistor density on a chip, doubling approximately every 2 years. Continuing at this pace, the transistor density will reach  $\sim 10^{13} \text{ cm}^{-2}$  by 2035, which at clock speeds of  $\sim 10 \text{ GHz}$  would result in  $\sim 40 \text{ MW/cm}^2$  of power dissipated on a chip. Unless the energy dissipation from

transistor switching can be reduced dramatically, the thermal load associated with 40 MW/cm<sup>2</sup> will exceed that in a rocket nozzle. The failure of thermal management on a chip might end the continued progress of the semiconductor industry well before 2035. The International Technology Roadmap for Semiconductors (<http://www.itrs.net>) has termed this imminent collapse the "Red Brick Wall," where "Red" indicates no "known manufacturable solutions" (of reasonable confidence) exist for continued scaling in some aspect of the semiconductor technology.

The scenario above motivates the search for signal-processing devices that dissipate very little energy when they switch. The emerging spintronic technology might offer such devices where information is carried by spin—in contrast to CMOS transistors, where it is carried by charge—since spin has an inherent advantage over charge when it comes to energy dissipation. Therefore, if a reliable way can be found to control and manipulate spins, spintronic devices could offer higher data processing speeds, lower electricity consumption, and many other advantages over conventional chips, perhaps including the ability to carry out radically new quantum computations.

A spintronic device calls for efficient methods to generate, conduct, process, and detect spin-encoded signals. We have reviewed the physics and emerging applications of two principal spintronic phenomena—giant magnetoresistance and spin-transfer-torque—that provide means to detect (GMR) and manipulate (STT) the spin signals. GMR has already spawned major technological change in the information storage industry with the usage of GMR sensors and read heads and, along with tunneling magnetoresistance (TMR), is expected to continue to dominate the detection of spin-encoded signals. STT is a more recent development in spintronics that provides an efficient means of controlling and manipulating spin distributions on the nanometer length scale and the picosecond-time scale, thus positioning STT as the method of choice for fast processing of spin signals in nanodevices.

What is the future of spintronic applications? A number of new spintronic devices based on GMR and STT have been proposed. These include high-frequency (GHz) oscillators, sources, and detectors, as well as magnetic field sensors—for example, in nonvolatile memories such as racetrack and STT magnetic random access memory (STT-MRAM). However, much fundamental work remains to be done before we see commercial applications of these devices. For the memory industry, development of these spintronic applications may lead to a universal memory that would combine cost benefits of DRAM, speed of SRAM, and nonvolatility of flash RAM. Potentially all logic operations on a chip could be carried out by manipulating spins in metallic systems instead of manipulating charges in semiconductor transistors, as in conventional microchips. Moreover, such operations could be combined on a chip with a universal memory. This would result in a new scalable and radiation-resistant electronics, computers, and so forth. The radiation resistance would be of particular interest for aerospace applications because the radiation in space is known to severely damage conventional electronics by building up a destructive charge in transistors. Long space trips that would expose onboard electronics to years of radiation would benefit from the radiation resistance and reduced power consumption (for example, like a nonvolatile memory that can retain the stored information even when not powered) of metallic spintronic devices. More generally, the impact of reduced power consumption in electronic devices is hard to overestimate, as we rely on such devices in almost every aspect of our everyday lives.

Finally, metallic spintronics and its applications discussed in this report are all based on already well-established physical phenomena such as GMR and STT. As the spintronics field is still in a relative state of infancy, new and more exciting phenomena are likely to be uncovered in the future.

## **6. References**

- (1) Baibich, M. N., et al., Phys. Rev. Lett. 61, 2472 (1988).
- (2) Binasch, G., et al., Phys. Rev. B 39, 4828 (1989).
- (3) Slonczewski, J. C., J. Magn. Magn. Mater. 159, L1 (1996).
- (4) Berger, L., J. Appl. Phys. 81, 4880 (1997).
- (5) Tsoi, M., et al., Phys. Rev. Lett. 80, 4281 (1998).
- (6) Myers, E. B., et al., Science 285, 867 (1999).
- (7) Sun, J. Z., J. Magn. Magn. Mater. 202, 157 (1999).
- (8) Wegrowe, J.-E., et al., Europhys. Lett. 45, 626 (1999).
- (9) Tsoi, M., et al., Nature 406, 46 (2000).
- (10) Beach, G. S. D., et al., Phys. Rev. Lett. 97, 057203 (2006).
- (11) Beach, G. S. D., et al., Phys. Rev. Lett. 102, 067201 (2009).
- (12) Fert, A., Bruno, P., in Ultrathin Magnetic structures II: An Introduction to the Electronic, Magnetic and Structural Properties, ed. by J.A.C. Bland and B. Heinrich (Berlin: Springer, 1994), p.82.
- (13) Levy, P. M., in Solid State Physics, ed. by H. Ehrenreich and D. Turnbull, vol. 47 (Boston, London: Acad. Press, 1994), p.367.
- (14) Dieny, B., J. Magn. Mag. Mat. 136, 335 (1994).
- (15) Gijs, M. A.M., Bauer, G. E. W., Adv. Phys. 46, 285 (1997).
- (16) Ansermet, J.-Ph., J. Phys.: Cond. Mat. 10, 6027 (1998).
- (17) Bass, J., Pratt, W. P., Jr., J. Magn. Magn. Mat. 200, 274 (1999).
- (18) Fert, A., Piraux, L., J. Magn. Magn. Mat. 200, 338 (1999).
- (19) Gijs, M. A.M., in Magnetic Multilayers and Giant Magnetoresistance: Fundamentals and Industrial Applications, ed. by U. Hartmann (Berlin: Springer, 2000), p.130.

- (20) Coehoorn, P., in *Magnetic Multilayers and Giant Magnetoresistance: Fundamentals and Industrial Applications*, ed. by U. Hartmann (Berlin: Springer, 2000), p.65.
- (21) Barthelemy, A., Fert, A., and Petroff, F., in *Handbook of Magnetic Materials*, edited by K. H. J. Buschow (Amsterdam: Elsevier, 1999), p.1.
- (22) Tsymbal, E.Y., Pettifor, D.G., in *Solid State Physics*, ed. by H. Ehrenreich and F. Spaepen, Vol. 56 (Academic Press, 2001) pp.113-237.
- (23) Ashcroft, W., Mermin, D., *Solid State Physics* (Saunders College Publishing, Forth Worth, 1976).
- (24) Ciureanu, P., in *Thin Film Resistance Sensors*, ed. by P. Ciureanu, S. Middelhoek (Institute of Physics Publishing, Bristol, 1992), p. 253.
- (25) *Electrocrystallization*, ed. by R. Weil, R. G. Barradas (The Electrochemical Society, Pennington, 1981).
- (26) Lashmore, D. S., Dariel, M. P., *J. Electrochem. Soc.* 135, 1218 (1988).
- (27) Ohring, M., *The Materials Science of Thin Films* (Academic, Boston, 1992).
- (28) Slaughter, J. M., Pratt, W. P., Jr., and Schroeder, P. A., *Rev. Sci. Instrum.* 60, 127 (1989).
- (29) Parkin, S. S. P., More, N., and Roche, K. P., *Phys. Rev. Lett.* 64, 2304 (1990).
- (30) Parkin, S. S. P., Bhadra, R., and Roche, K. P., *Phys. Rev. Lett.* 66, 2152 (1991).
- (31) Fert, A., Campbell, I. A., *J. de Physique* 32, C1-46 (1971).
- (32) Mott, N. F., *Proc. Roy. Soc. London, Ser. A* 153, 699 (1936), and 156, 368 (1936), and *Adv. Phys.* 13, 325 (1964).
- (33) Pratt, W. P., Jr., et al., *Phys. Rev. Lett.* 66, 3060 (1991).
- (34) Dieny, B., et al. *J. Appl. Phys.* 69, 4774 (1991).
- (35) Piraux, L., et al., *Appl. Phys. Lett.* 65, 2484 (1994).
- (36) Blondel, A., Meier, J. P., Doudin, B., Ansermet, J.-Ph., *Appl. Phys. Lett.* 65, 3019 (1994).
- (37) Tsoi, M., Jansen, A. G. M., Bass, J., *J. Appl. Phys.* 81, 5530 (1997).
- (38) Smith, C., *Proc. UK Conf. for Sensors, Test and Measurement Technology*, Birmingham, England, Jan. 22-23, 1997.
- (39) Daughton, J. M., et al., *IEEE Trans. Magn.* 30, 4608 (1994).

- (40) Ji, Y., Chien, C. L., Stiles, M. D., Phys. Rev. Lett. 90, 106601 (2003).
- (41) Rippard, W. H., Pufall, M. R., Kaka, S., Russek, S. E., Silva, T. J., Phys. Rev. Lett. 92, 27201 (2004).
- (42) Katine, J. A., Albert, F. J., Buhrman, R. A., Myers, E. B., Ralph, D. C., Phys. Rev. Lett. 84, 3149 (2000).
- (43) Grollier, J., et al., Appl. Phys. Lett. 78, 3663 (2001).
- (44) Liu, Y., Zhang, Z., Wang, J., Freitas, P. P., Martins, J. L., J. Appl. Phys. 93, 8385 (2003)
- (45) Moriya, R., Hamaya, K., Oiwa, A., Munekata, H., Jpn. J. Appl. Phys. Part 2 - Lett. Express Lett. 43, L825 (2004).
- (46) Dieny, B., et al., Phys.Rev.B 43, 1297 (1991).
- (47) Waintal, X., Myers, E. B., Brouwer, P. W., Ralph, D. C., Phys. Rev. B 62, 12317-12327 (2000)
- (48) Braganca, P.M., et al., Appl. Phys. Lett. 87, 112507 (2005).
- (49) Rippard, W. H., et al., Phys. Rev. Lett. 95, 067203 (2005).
- (50) Kiselev, S. I., et al., Nature 425, 380 (2003).
- (51) Krivorotov, I. N., et al., Science 307, 228-231 (2005).
- (52) Acremann, Y., et al., Phys. Rev. Lett. 96, 217202 (2006).
- (53) Kilcoyne, A. L. D., et al., J. Synchrotron Radiat. 10, 125 (2003).
- (54) Stöhr, J., et al., Science 259, 658 (1993).
- (55) Rippard, W. H., Pufall, M. R., Kaka, S., Silva, T. J., Russek, S. E., Phys. Rev. B 70, 100406 (2004).
- (56) Khitun, A., Nikonov, D. E., Bao, M., Galatsis, K., Wang, K. L., Nanotechnology 18, 465202 (2007).
- (57) Schneider, T., et al., Appl. Phys. Lett. 92, 022505 (2008).
- (58) Driskill-Smith, A. A. G., Huai, Y., Future Fab Intl. 23, 28 (2007).
- (59) Berger, L., J. Appl. Phys. 49, 2156 (1978).
- (60) Berger, L., J. Appl. Phys. 55, 1954 (1984).
- (61) Berger, L., Phys. Rev. B 33, 1572 (1986).



- (62) Berger, L., J. Appl. Phys. 63, 1663 (1988).
- (63) Freitas, P. P., Berger, L., J. Appl. Phys. 57, 1266 (1985).
- (64) Hung, C.-Y., Berger, L., J. Appl. Phys. 63, 4276 (1988).
- (65) Hung, C.-Y., Berger, L., Shih, C.Y., J. Appl. Phys. 67, 5941 (1990).
- (66) Yamanouchi, M., Chiba, D., Matsukura, F., Ohno, H., Nature 428, 539 (2004).
- (67) Ravelosona, D., et al., Phys. Rev. Lett. 95, 117203 (2005).
- (68) Tsoi, M., Fontana, R. E., Parkin, S. S. P., Appl. Phys. Lett. 83, 2617 (2003).
- (69) Grollier, J., et al., Appl. Phys. Lett. 83, 509 (2003).
- (70) Beach, G. S. D., Nistor, C., Knutson, C., Tsoi, M., Erskine, J. L., Nat. Mater. 4, 741 (2005).
- (71) Beach, G. S. D., Knutson, C., Tsoi, M., Erskine, J. L., J. Magn. Magn. Mater. 310, 2038 (2007).
- (72) Hayashi, M., et al., Phys. Rev. Lett. 96, 207205 (2006).
- (73) Hayashi, M., et al., Nat. Phys. 3, 21 (2007).
- (74) Klaui, M., et al., Appl. Phys. Lett. 83, 105 (2003).
- (75) Kimura, T., Otani, Y., Yagi, I., Tsukagoshi, K., Aoyagi, Y., J. Appl. Phys. 94, 7226 (2003).
- (76) Vernier, N., Allwood, D. A., Atkinson, D., Cooke, M. D., Cowburn, R. P., Europhys. Lett. 65, 526 (2004).
- (77) Laufenberg, M., et al., Phys. Rev. Lett. 97, 046602 (2006).
- (78) Thomas, L., et al., Nature 443, 197 (2006).
- (79) Yamaguchi, A., et al., Phys. Rev. Lett. 92, 077205 (2004).
- (80) Yamaguchi, A., et al., Phys. Rev. Lett. 96, 179904 (2006).
- (81) Klaui, M., et al., Phys. Rev. Lett. 95, 026601 (2005).
- (82) Meier, G., et al., Phys. Rev. Lett. 98, 187202 (2007).
- (83) Parkin, S. S. P., Hayashi, M., Thomas, L., Science 320, 190 (2008).
- (84) Núñez, A. S., et al., Phys. Rev. B 73, 214426 (2006).

- (85) Xu, Y., Wang, S., Xia, K., Phys. Rev. Lett. 100, 226602 (2008).
- (86) Gomonay, H., Loktev, V., Low Temp. Phys. 34, 198 (2008).
- (87) Wei, Z., Sharma, A., Bass, J., Tsoi, M., J. Appl. Phys. 105, 07D113 (2009).
- (88) Meiklejohn, W. H., Bean, C. P., Phys. Rev. 102, 1413 (1956).
- (89) Stöhr, J., Siegmann, H. C., Magnetism: from fundamentals to nanoscale dynamics (Springer Series in Solid-State Sciences, Vol. 152, Springer, 2006).
- (90) Urazhdin, S., Chien, C. L., Guslienko, K. Y., Novozhilova, L., Phys. Rev. B 73, 054416 (2006).
- (91) Wei, Z., et al., Phys. Rev. Lett. 98, 116603 (2007).
- (92) Urazhdin, S., Anthony, N., Phys. Rev. Lett. 99, 046602 (2007).
- (93) Tang, X.-L., Zhang, H.-W., Su, H., Zhong, Z.-Y., Jing, Y.-L., Appl. Phys. Lett. 91, 122504 (2007).
- (94) Dai, N. V., et al., Phys. Rev. B 77, 132406 (2008).
- (95) Basset, J., Sharma, A., Wei, Z., Bass, J., Tsoi, M., Proc. SPIE 7036, 703605 (2008).
- (96) Wei, Z., Basset, J., Sharma, A., Bass, J., Tsoi, M., J. Appl. Phys. 105, 07D108 (2009).
- (97) Moore, G. E., Electronics Magazine (McGraw Hill, New York, 1965).

~~UNCLASSIFIED//FOR OFFICIAL USE ONLY~~



# Defense Intelligence Reference Document

*Acquisition Threat Support*

6 April 2010

ICOD: 1 December 2009

DIA-08-1004-006

## Metamaterials for Aerospace Applications

~~UNCLASSIFIED//FOR OFFICIAL USE ONLY~~

## Metamaterials for Aerospace Applications

**Prepared by:**

(b)(3):10 USC 424

**Defense Intelligence Agency**

**Author:**

(b)(6)

**Administrative Note**

COPYRIGHT WARNING: Further dissemination of the photographs in this publication is not authorized.

This product is one in a series of advanced technology reports produced in FY 2009 under the Defense Intelligence Agency, (b)(3):10 USC 424 Advanced Aerospace Weapon System Applications (AAWSA) Program. Comments or questions pertaining to this document should be addressed to (b)(3):10 USC 424;(b)(6), AAWSA Program Manager, Defense Intelligence Agency, ATTN: (b)(3):10 USC 424 Bldg 6000, Washington, DC 20340-5100.

## Contents

Definition of Metamaterials .....	1
Applications to Sub-Diffraction Imaging: Super-Lens and Hyper-Lens .....	6
Applications to Circuits and Waveguide Miniaturization: Slowing Down and Manipulating Electromagnetic Pulses (EMP) Using Advanced Metamaterials .....	16
Metamaterials for Energy Harvesting .....	20
Nonlinear Non-Reciprocal Chiral Metamaterials: For Developing Novel Optical Isolators and "One-Way" Microwave Mirrors .....	27
Tunable Switchable Metamaterials .....	30
Summary and Conclusions .....	31
References .....	31

## Figures

Figure 1. Example of a Metamaterial Component: The Magnetic Split Ring Resonator (SRR) Design .....	2
Figure 2. Example of Another Metamaterial Component: Electric Ring Resonator (ERR).....	2
Figure 3. Geometry of Original Planar Metamaterial Unit Cells (OE1-OE6) and Their Complements (CE1-CE6) .....	3
Figure 4. Recent Optical Metamaterials for Telecommunication Wavelength and Mid-Infrared Indefinite Permittivity Material .....	5
Figure 5. Schematic of The Super-lens With $n=-1$ Refractive Index Corresponding to ( Surrounded by Vacuum.....	7
Figure 6. Schematic of the SiC-based Super-lens Which is Imaging Sub-wavelength Holes Buried Under the SiO <sub>2</sub> Layer.....	8
Figure 7. Theoretical Concepts (left panel) and Experimental Implementation (right panel) of an Optical Hyperlens Capable of Magnifying Sub- Diffraction Objects to Observable (larger than Size.....	9
Figure 8. Hyperlens Based on a Converging Array of Metal Wires .....	10
Figure 9. Far-Field Super-lens (FSL) Based on an Indefinite Permittivity Metamaterial Placed Between the Object and the Image-Releasing Grating .....	12
Figure 10. Tomographic Multi-Beam Multi-Detector Holography of Sub-Wavelength Objects Using Indefinite Permittivity Medium (IPM) .....	12
Figure 11. First Experimental Demonstration of Propagating Sub-Diffraction Waves in the Indefinite Permittivity Medium (IPM) .....	13
Figure 12. Schematic for 2-Beams/2-Detectors Interferometric Measurement and Numerical Simulation. ....	14
Figure 13. Experimental Setup for 2-Beams/2-Detectors Interferometric Measurement in the Lab and Preliminary Experimental Results .....	15

**Figure 14. Schematic of Pulse Compression in Magnetized Plasma ..... 16**  
**Figure 15. Trapped Rainbow: A Waveguide With Negative Index Core Can Stop Light..... 17**  
**Figure 16. "Plasmonic Molecule" Exhibiting EIT ..... 18**  
**Figure 17. True Multi-Layer Metamaterial With a Unit Cell Shown in Figure16: Radiative Antenna (Single Metal Strip) Coupled to a Dark Antenna (Two Perpendicular Metal Bars) ..... 19**  
**Figure 18. "Perfect" Narrow-Band Microwave Absorber..... 20**  
**Figure 19. Wide-Angle Plasmonic Absorber Based on Negative Index Metamaterial ..... 21**  
**Figure 20. Specific Design of a Wide-Angle Plasmonic Absorber Based on Negative Index Metamaterial Operating at  $\lambda=1550\text{ nm}$  ..... 22**  
**Figure 21. Experimental Reflectivity vs. Wavelength and Theoretical Plot of Reflectivity Contours ..... 23**  
**Figure 22. Preliminary Attempts to Design a Better Absorber Using Complementary MetaMaterials (U-shaped C-MM) ..... 25**  
**Figure 23. Engineering the Complex Reflectivity Coefficient Using the Concept of a MetaMirror. .... 26**  
**Figure 24. Example of a Generic Chiral Metamaterial ..... 28**  
**Figure 25. Example of Time-Irreversibility of Light Propagation Inside the Twisted Fiber Core..... 29**  
**Figure 26. THz Properties of an Electric Split Ring Resonator ..... 31**

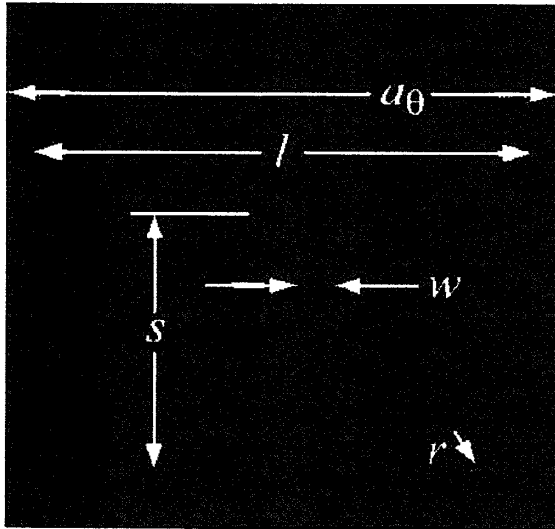
## Definition of Metamaterials

A metamaterial is defined as an artificial medium whose properties (mechanical, optical, magnetic, or other) cannot be found in naturally-occurring materials. The emphasis of this study will be on electromagnetic and optical metamaterials. Such metamaterials can exhibit rather extreme properties, such as negative refractive index, which implies that both electric permittivity and magnetic permeability must be negative ( $\epsilon < 0$ ,  $\mu < 0$ ) (Reference 1). Such metamaterials used to be called "left-handed" because of the unusual phase relationship between the electric and magnetic fields. Specifically, in most (positive index, including vacuum) media one uses the right-hand rule to define the relationship between electric field ( $\vec{E}$ ), magnetic field ( $\vec{H}$ ), and the propagation wavenumber ( $\vec{k}$ ). The physical basis of the right-hand rule is that the direction of energy propagation defined by the Poynting vector  $\vec{S} = c\vec{E} \times \vec{H} / 4\pi$  and the direction of the phase velocity (defined by the wavenumber  $\vec{k}$ ) must coincide. That does not hold true for negative index metamaterials where the two directions are opposite, therefore, the left-handed relationship must hold for the three vectors. Nevertheless, the "left-handed" designation did not withstand the test of time because it was causing confusion and creating irrelevant allusions to helical (a.k.a. chiral) structures. Although chiral structures can indeed exhibit negative index behavior (Reference 2), chirality is not necessary.

A typical metamaterial consists of resonant elements such as Split Ring Resonators (SRR). An example of an SRR is shown in Figure 1. The main function of the SRR is to enable strong magnetic response of the structure. A simple empirical formula exists for the magnetic permeability of a metamaterial comprised of the SRRs:

$$\mu = 1 - \frac{F\omega_M^2}{\omega^2 - \omega_M^2} < 0, \quad (1)$$

where  $\omega_M$  is the resonant frequency of the SRR, and  $F$  is proportional to the volume filling factor of SRRs. It is noteworthy that SRRs are designed in such a way that it has a large capacitance. As the result, the resonant frequency of an SRR is small, (that is, the SRR-containing cell is very sub-wavelength). In the example shown in Figure 1 (taken from Reference 6), the unit cell operated at  $\omega/2\pi = 10$  GHz is  $\lambda/10$ . In fact, the sub-wavelength size of the metamaterial is what distinguishes them from their close cousins: photonic crystals. By properly designing magnetic SRRs, it is possible to achieve any value of  $\mu$  for any given frequency. Special challenges exist for optical structures, though, as will be explained below.



cyl.	$r$	$s$	$\mu_r$
1	0.260	1.654	0.003
2	0.254	1.677	0.023
3	0.245	1.718	0.052
4	0.230	1.771	0.085
5	0.208	1.825	0.120
6	0.190	1.886	0.154
7	0.173	1.951	0.188
8	0.148	2.027	0.220
9	0.129	2.110	0.250
10	0.116	2.199	0.279

**Figure 1. Example of a Metamaterial Component: The magnetic split ring resonator (SRR) design.** The in-plane lattice parameters are  $a_y = a_z = 10/3$  mm. The ring is square, with edge length  $l = 3$  mm and tracewidth  $w = 0.2$  mm. The substrate is 381  $\mu\text{m}$ -thick Duroid 5870 ( $\epsilon = 2.33$ ,  $t_d = 0.0012$  at 10 GHz, where  $t_d$  is the loss tangent). The Cu film, from which the SRRs are patterned, is 17  $\mu\text{m}$  thick. The parameters  $r$  and  $s$  are given in the table together with the associated value of  $\mu_r$ . (Reference 6)

Electric properties of metamaterials can be similarly controlled. An example of a planar electrically-active metamaterial is shown in Figure 2.

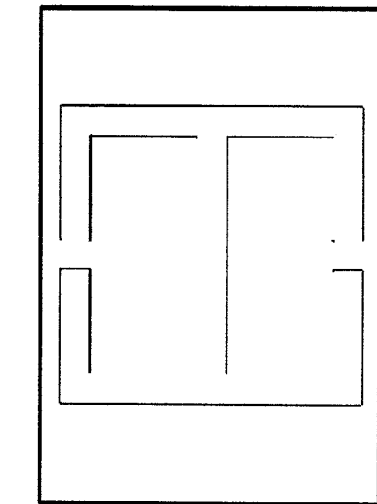
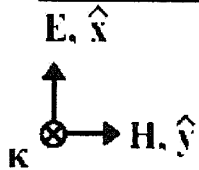


**Figure 2. Example of Another Metamaterial Component: Electric Ring Resonator (ERR).** This component provides tunable resonant electric response to the incident electromagnetic field, and can be utilized for engineering the frequency-dependent dielectric permittivity  $\epsilon(\omega)$ . Possible application: THz and microwave absorbers. (Reference 7)





The electric response of such (or similar) metamaterial is given by

$$\epsilon(\omega) = 1 - \frac{\omega_p^2}{\omega^2 - \omega_r^2 + i\omega\gamma} \quad (2)$$

where  $\omega_r$  is the resonant frequency and  $\gamma$  is the loss coefficient.

Negative index metamaterials are by no means the only potentially useful metamedia. Several new concepts such as Indefinite Permittivity Metamaterials (IPM) (References 3, 4) and Epsilon-Near-Zero (ENZ) metamaterials (Reference 5) have recently emerged and found some exciting applications that will be reviewed below. IPMs can be used as ultra-compact spatial filters (both high-pass and low-pass) whereas ENR metamaterials can be used for making sub-wavelength waveguides capable of coupling close to 100 percent of the incident radiation (Reference 8), as well as directing it around tight bends with negligible bending losses. Yet another class of planar metamaterials, complementary metamaterials (CMMs), has recently emerged (Reference 7). Instead of using metallic structures deposited on a substrate (left panel of Figure 3), CMMs consist of slits in the continuous metal screen (right panel of Figure 3). The shape of the slits coincides with that of the materials themselves. Such complementary metamaterials have been recently used for making epsilon-near zero waveguides (Reference 8).

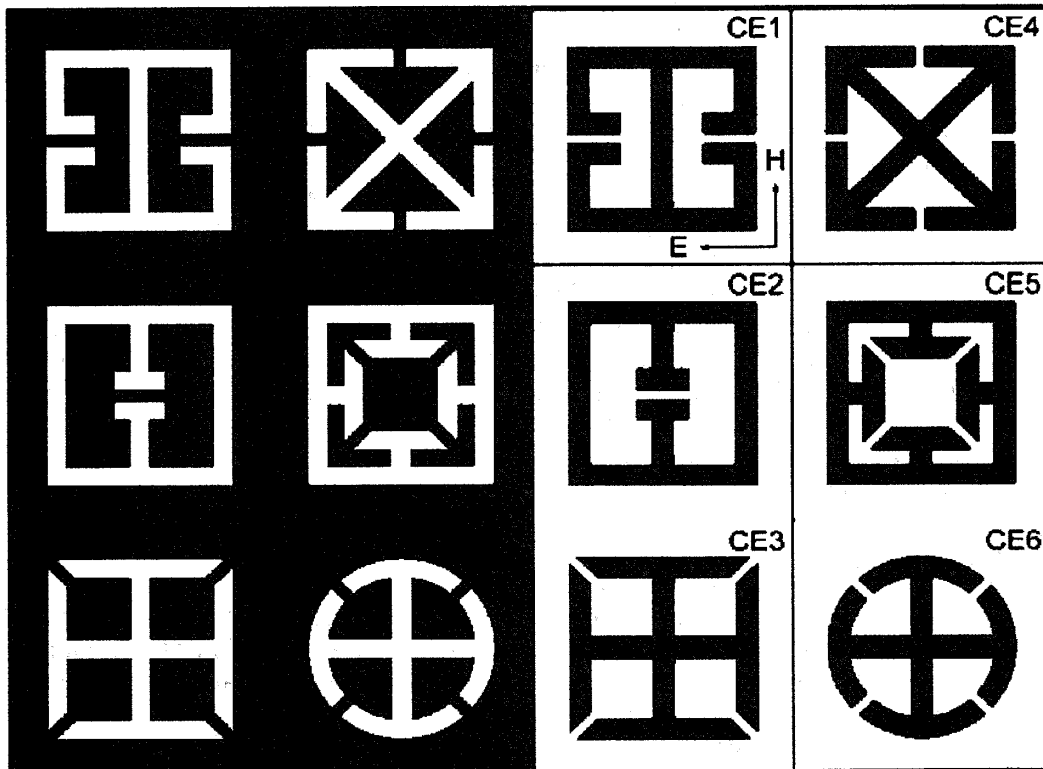


**Figure 3. Geometry of Original Planar Metamaterial Unit Cells (OE1-OE6) and Their Complements (CE1-CE6).** The polarization of normally incident electromagnetic radiation is configured as shown in OE1 and CE1 for the original and complementary metamaterials, respectively. (Reference 9)

In general, metamaterials offer a new way of designing electromagnetic structures with arbitrary values of permittivity/permeability tensors, as well as other parameters (such as bi-anisotropy coefficient). In many instances, metamaterials enable us to considerably minimize sizes of resonators, transmission lines, and so forth. Such miniaturization is possible due to the resonant nature of the individual unit cells. Specifically, the structures shown in Figure 3 have high capacitance; therefore, their individual sizes are very sub-wavelength. That enables arrangement within sub-wavelength units that can be densely packed and result in strongly miniaturized components. It is this miniaturization that makes metamaterials interesting for aerospace application where small weight and size are essential.

While the most spectacular progress in the field of electromagnetic metamaterials has so far occurred in the microwave range, it is the optical (visible, infrared, mid-infrared) spectral regions that hold most promise for revolutionary applications. Electromagnetic metamaterials have a tremendous potential for revolutionizing propagation, storage, and conversion of electromagnetic waves across the entire Electromagnetic Spectrum. In our opinion, the most exciting applications that are relevant for aerospace applications include energy harvesting, developing novel optical devices with unusual yet practically important capabilities (for example, non-reciprocal devices), enhancing the efficiency of nonlinear optical devices, developing novel imaging modalities capable of breaking the diffraction limit (for example, super-lenses, hyper-lenses, far field super-lenses), and developing novel lithographic techniques.

Optical metamaterials are still a very new area. Just a handful of experimental demonstrations of multi-layer (truly bulk) optical metamaterials exist at the moment. Among the most recent ones are (a) demonstration of the negative index optical metamaterial at the telecommunications wavelength (Reference 10) that used the so-called fishnet structure shaped as a prism for demonstrating Snell's Law, and (b) demonstration of the Indefinite Permittivity Material (IPM) and *negative refraction* (which, in the context of anisotropic metamaterials, is not the same as *negative refractive index*) in the mid-infrared part of the spectrum (Reference 11). These structures have the distinction of being multi-layer (or bulk). Most previous examples of optical metamaterials have dealt with single or double-layer substances which cannot be, strictly speaking, characterized as metamaterials. The difficulty in obtaining strong magnetic activity in optical metamaterials has been explained in several recent reviews (References 12, 13). In a nutshell, the issue is that the magnetic moment of most structures (including atomic systems) is very small, much smaller than the electric moment. Therefore, it is difficult to observe any optical effects that can be clearly assigned to magnetic activity. This is especially true for the structures that are much smaller than one wavelength. Exceptions, such as artificially constructed split rings, are possible. However, such structures cannot be operated at very high frequency because of the excitation of electrostatic resonances (Reference 12). In other words, when the resonant frequency is too high (or the dielectric permittivity of a metal is not sufficiently large), electrostatic resonances disrupt magnetic activity. More specifically, the energy inside and in the vicinity of a metamaterial element (for example, Split Ring Resonator) becomes predominantly electrostatic, (that is, in the form of the kinetic energy of oscillating electrons). The recently described multi-layer fishnet (Reference 10) is not an exception: its unit cell (that is, the lateral period) is only one-half of the operating wavelength.

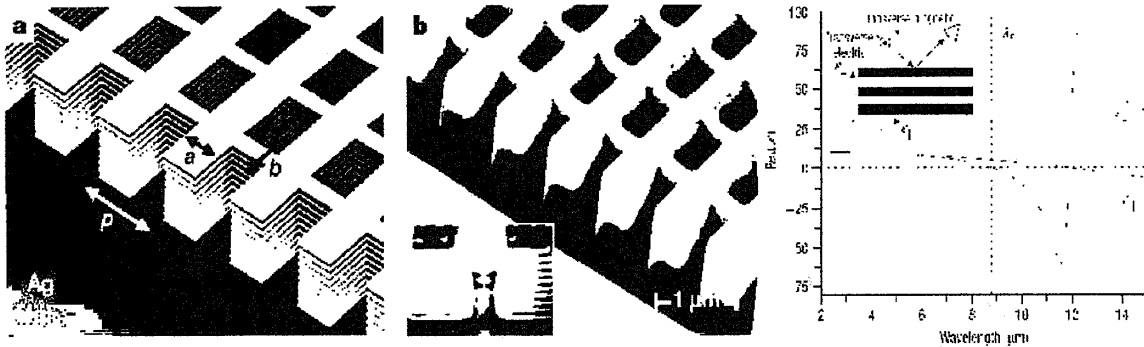


**Figure 4. Recent Optical Metamaterials for Telecommunication Wavelength  $\lambda = 1.5 \mu\text{m}$  (Left and Middle) and Mid-Infrared IPM.** The multi-layer fishnet is made of silver films separated by a dielectric spacer. A focused ion beam was used to produce the prism-shaped fishnet. The IPM was obtained by depositing interleaved 80 nm layers of  $\text{In}_{0.53}\text{Ga}_{0.47}\text{As}$  and  $\text{Al}_{0.48}\text{In}_{0.52}\text{As}$ . The layers, approximately  $8.1 \mu\text{m}$  thick, grown by molecular beam epitaxy on lattice-matched InP substrates. The InGaAs layers were uniformly doped to create different values of permittivity in alternating layers. (Reference 10 and 11)

That is not to say that there is not ongoing theoretical and experimental work on designing optical metamaterials for practical applications. The author's research group at UT- Austin, has designed the first Plasmonic Negative Index Metamaterials (P-NIM) super-lens (Reference 14), developed novel techniques for analyzing optical properties of plasmonic nanostructures, (including band-structure calculations of periodic nanostructures) (Reference 15) and quasi-static calculations of plasmonic resonances (Reference 16). The UT-Austin group has also designed a number of unique sub-wavelength P-NIMs in the optical part of the spectrum (References 14, 17, 18), and has recently published a review of optical P-NIMs (Reference 12). The group has also contributed to developing and experimentally implementing the concept of the "perfect lens" (Reference 19) based on plasmonic/polaritonic materials. A perfect lens enables imaging of sub-wavelength objects in the infrared part of the spectrum, including objects buried under the surface. Also developed is a Wide-Angle "Perfect" Absorber of Mid-Infrared Radiation (WAPAMIR) (Reference 20) based on the negative index metamaterial whose impedance is perfectly matched to vacuum.

Below is a concise summary of various topics/applications that are especially suitable for the aerospace industry. This study concentrates on the facility of metamaterials to miniaturize various optical and microwave components. Metamaterials can also be used for imaging very small (sub-wavelength) objects without resorting to costly and space-consuming near-field scanning optical microscopy. Also described are the ongoing efforts in the field to make extremely compact metamaterials-based lasers. Smaller lasers mean smaller weight and more room for other diagnostic devices and useful payload within the confines of a space vehicle. Applications of metamaterials to photon harvesting is especially fitting for advanced aerospace platforms because of the necessity to collect electromagnetic energy for battery recharging, diagnostic spectroscopy, and other vital functions of a space vehicle.

- **Complementary Metamaterials for Energy Harvesting.** Development of ultra-thin photovoltaic and thermo-photovoltaic cells is hampered by weak photon absorption in semiconductors. Metamaterials can modify absorption making it wavelength-selective (tunable), highly efficient, and, if desired, wide-angle. Recently a way has been found for creating quarter-wavelength resonators backed by leaky mirrors made out of CMMS.

- **Far Field Super-Lens Based on the Interferometry of Sub-Diffraction Waves.** Sub-diffraction imaging has long been considered to be possible only using near-field microscopes. Those are fairly complex, slow-scanning, and large devices that are not appropriate for advanced aerospace platforms. Metamaterials enable new imaging modalities: super-lenses, hyper-lenses, and far-field super-lenses. In addition to a survey of the existing scientific literature, novel ideas on developing a new interferometric Far-field Super-Lens (FSL) based on the multi-beam multi-detector technique utilizing materials with Indefinite Permittivity Tensor are presented. Fabrication of such Indefinite Permittivity Materials (IPMs) for the mid-infrared part of the spectrum is achieved and demonstrates the capabilities of transmitting electromagnetic waves with the spatial period much smaller than the vacuum wavelength of light. Interference between sub-diffraction waves enables disentangling multiple diffractive orders and extracting their amplitudes.
- **Nonlinear Non-Reciprocal Chiral Metamaterials: Developing Novel Optical Isolators and "One-Way" Microwave Mirrors.** These developments are motivated by the need to construct one-way "light diodes" for compact optical isolators. Presently there are two approaches to optical isolation: the most common using magnetic fields, and the less developed based on using nonlinearities. A different approach relies on the phenomenon of adiabatic mode conversion in nonlinear chiral metamaterials. Preliminary theoretical results for a simple chiral fiber with a variable twist period (pitch) that enables full transmission of a tightly confined core mode in the forward direction and full mode-conversion of the core mode into a cladding mode for the backwards propagation is obtained.
- **Slowing Down Light and Miniaturizing Optical Components Using the Phenomenon of Electromagnetically Induced Transparency in Metamaterials.** The speed of light places a natural limit on the size of optical/microwave components. Metamaterials offer an exciting opportunity to slow down light. This has two major implications: (a) light can be stored/manipulated in smaller volumes, and (b) nonlinear effects are strongly enhanced by the resulting energy compression.

## **Applications to Sub-Diffraction Imaging: Super-Lens and Hyper-Lens**

The super-lens is one of the earliest applications of metamaterials (Reference 21), and its principle is shown in Figure 5. Without the super-lens, all information about sub-diffraction (or sub-wavelengths, which is equivalent) features of the periodic object would have been lost. The reason for the information loss is evanescent decay of the large spatial wavenumbers. The only method of accessing/measuring these features would be to scan the object using a near field scanning optical microscope. By inserting a super-lens between the object and the imaging plane, evanescent waves may be amplified and the image transferred forward. Unfortunately, this approach by itself does not remove the need for a near-field scanning device; the image that is recreated in the imaging plane is still sub-wavelength, and needs to be read out.

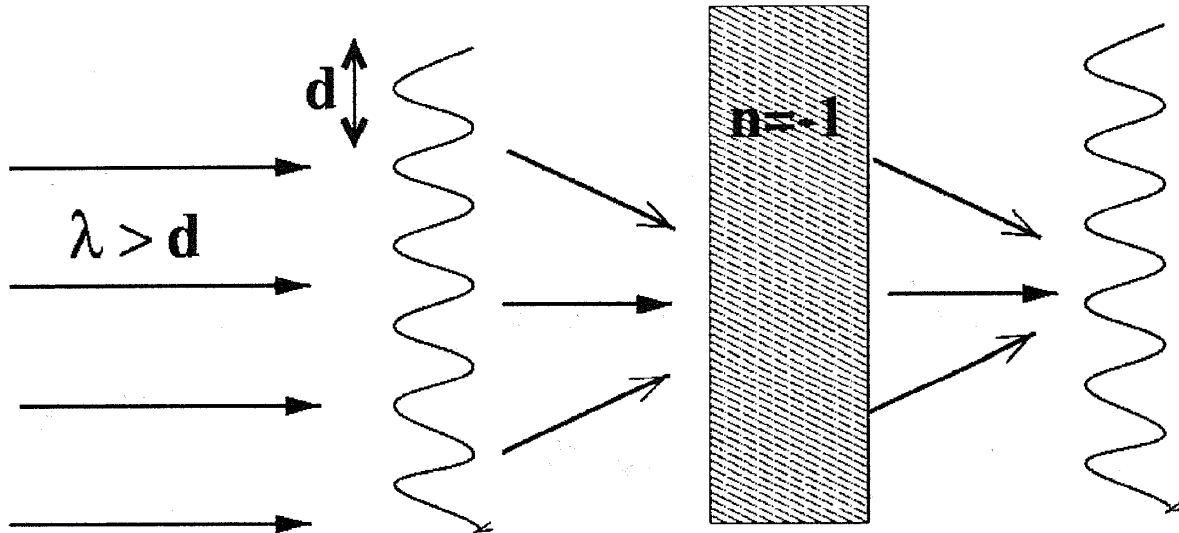


**Figure 5. Schematic of the Super-Lens with  $n=-1$  Refractive Index Corresponding to  $(\epsilon = -1, \mu = -1)$  Surrounded By Vacuum.** Super-lens' presence enables imaging sub-diffraction objects such as the periodic grating shown here.

There are, however, interesting circumstances when it is very important to transport the image towards the scanning device. One such special circumstance is spatially-resolved spectroscopy of small (for example, cellular) structures. One can envision space expeditions to other planets that could, potentially, result in finding some evidence of primitive cellular-level life. It would then be highly desirable to examine the structure of the living cell in its natural environment. In all likelihood, that environment would be liquid. Therefore, it would be very desirable to examine the cell without actually touching it with a tip of a near-field optical microscope. Thus, the sub-surface imaging of a small object which is buried underneath a liquid layer would be necessary. No such experiments have so far been conducted. However, several years ago there was an experiment demonstrating imaging of sub-diffraction objects buried under the layer of silicon dioxide.

The schematic and experimental results from the experiment (Reference 19) are shown in Figure 6. In this experiment the sub-wavelength objects were simple holes that were milled in the metal using an FIB. They were buried underneath the super-lens consisting of SiC (negative epsilon material for mid-infrared frequencies) and silicon dioxide (positive epsilon material). Note that this configuration (materials with  $\epsilon_1 > 0$  and  $\epsilon_2 \approx -\epsilon_1 < 0$  joined together: sandwiched or positioned next to each other) is typical for a near-field super-lens. The difference between the near-field super-lens shown in Figure 6 and the "ideal" super-lens shown in Figure 5 is that the ideal also requires a material with a negative value of magnetic permeability.

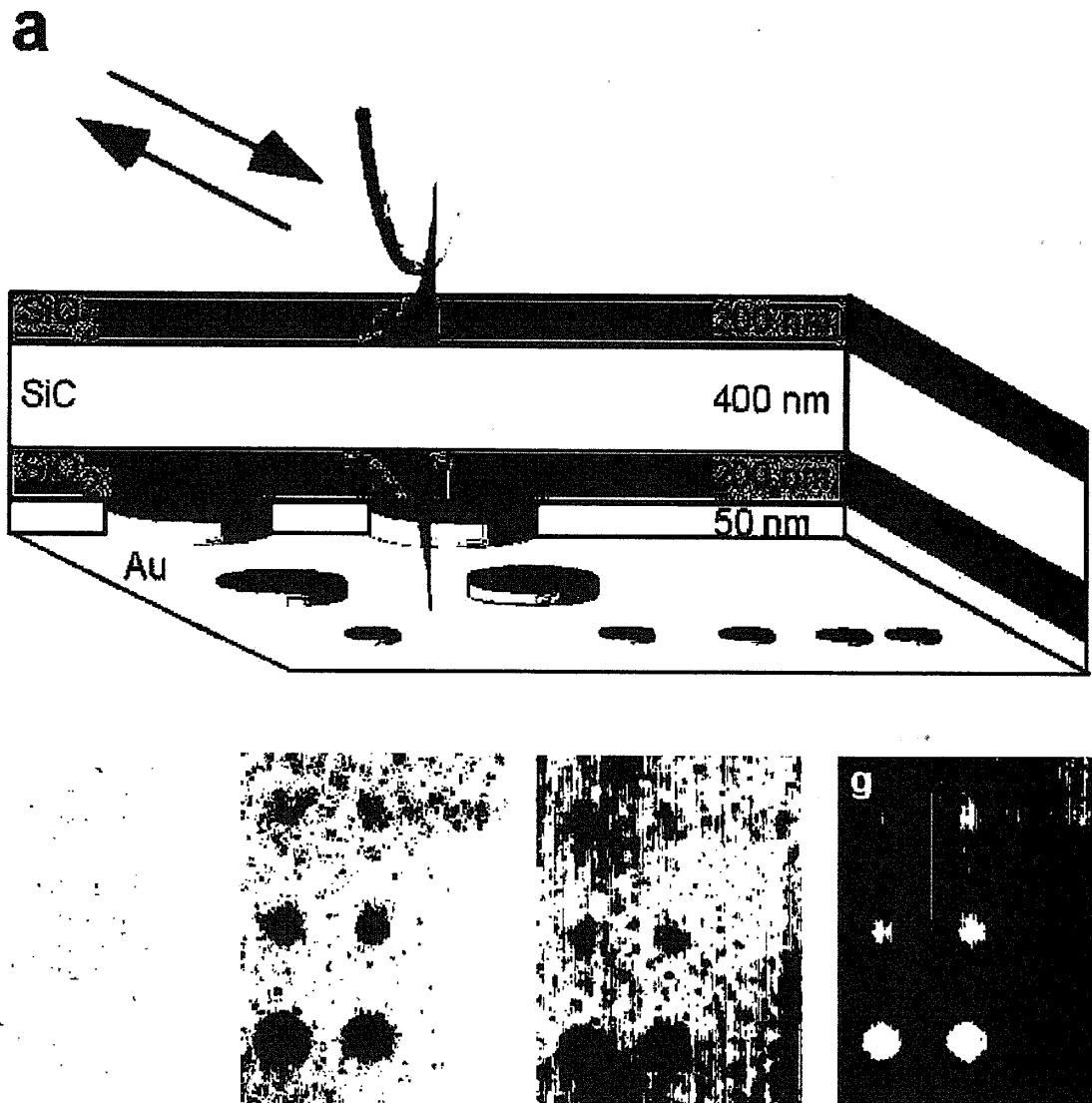


**Figure 6. Schematic of the SiC-Based Super-Lens Which is Imaging Sub-Wavelength Holes Buried Under the SiO<sub>2</sub> Layer.** The imaged objects are  $\lambda/20$  holes milled in gold using FIB. The scattered signal is picked up by the tip of an NSOM and directed towards the IR detector. Depending on the imaging wavelength, either amplitude (e) or the phase (f,g) of the signal are prominent.

As the laser beam scatters off the sub-wavelength holes, its electric field is picked up by the tip of a Near-Field Scattering Optical Microscope (NSOM) and re-scattered into the far-field. There it is interfered with the reference pulse and picked up by an infrared detector. Note that this interferometric technique enables one to extract both the phase and amplitude of the field, as shown in Figure 6. This significantly broadens the spectral range over which the super-lens yields meaningful information. For example, the amplitude contrast is highest at  $\lambda = 10.85 \mu\text{m}$  shown in panel (e) while the phase contrasts are the highest at  $\lambda = 11.03 \mu\text{m}$  and  $\lambda = 10.65 \mu\text{m}$ .

Despite the convenience of the near-field super-lens, (that is, its ability to transport the image) it still requires an NSOM to read out the image. Within the confines of an advanced aerospace platform such device (with its necessary auxiliaries) may not fit. Therefore, one has to consider alternative metamaterials-based ideas for sub-diffraction imaging. One such idea, the hyper-lens, has been proposed recently by two groups (References 22-24), and already experimentally tested by another group (Reference 25). The principle of the hyper-lens is very simple: to use an indefinite permittivity medium (sometimes referred to as the hyperbolic medium because the relationship between the propagation wavenumbers and the frequency, also known as the constant frequency contour, has a hyperbolic nature) in a tapered format. Several conceptual implementations such as the spoke-like structure and the cylindrical multi-layer structure (see Figure 7, left panel) have been suggested. The hyper-lens works on two principles: (a) indefinite permittivity materials (of which the super-lens is one example) are capable of propagating sub-diffraction waves, and (b) the expanding nature of the hyper-lens can magnify images to the  $\lambda/2$  size, at which point they become observable in a conventional microscope. One recent experimental implementation of the hyper-lens in UV is shown in the right panel of Figure 7. The hyper-lens is made of 16 layers of Ag/Al<sub>2</sub>O<sub>3</sub>. This specific hyper-lens was used for imaging a line pair object with line width of 35 nm and spacing of 150 nm and was operated at  $\lambda = 400$  nm. The magnified image (350 nm spacing) can be clearly resolved with an optical microscope [numerical aperture (NA) = 1.4], thus demonstrating magnification and projection of a sub-diffraction-limited image into the far field.

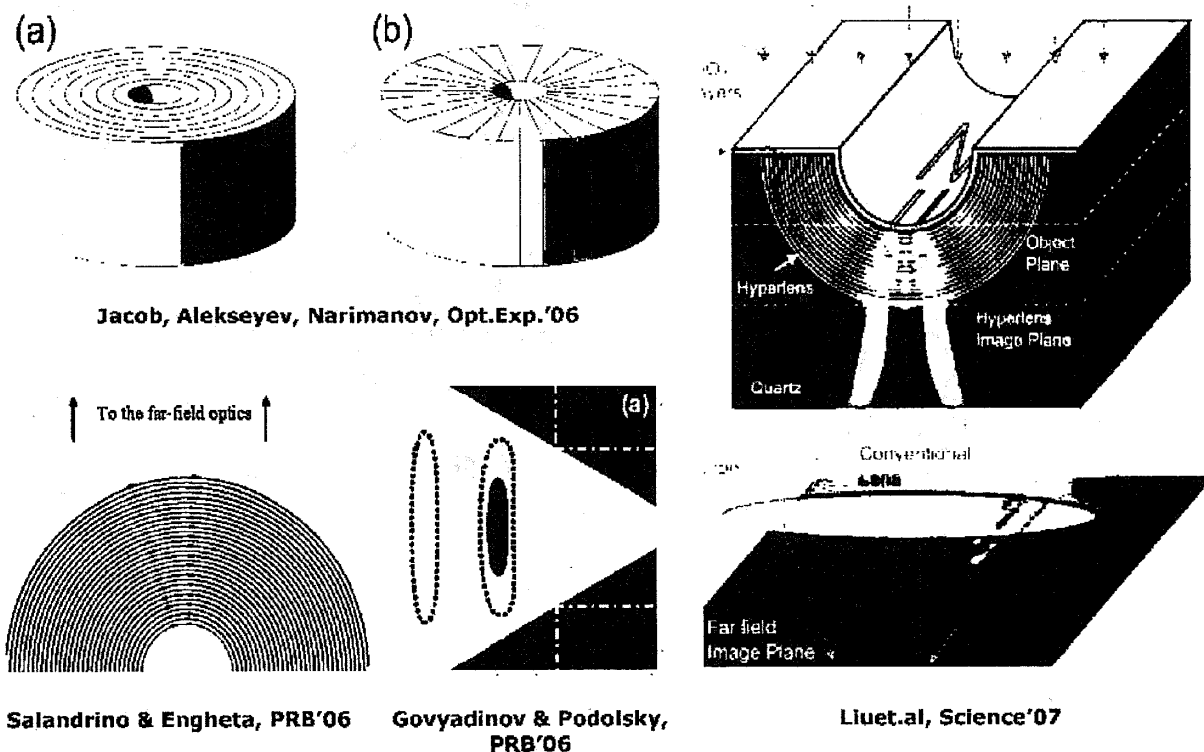


**Figure 7. Theoretical Concepts (left panel) and Experimental Implementation (right panel) of an Optical Hyper-lens Capable of Magnifying Sub-Diffraction Objects to Observable (larger than  $\lambda/2$ ) Size**

Note that the hyper-lens concept does not require employing a bulky near-field scanning optical microscope. However, the practical implementation of the hyper-lens is by no means simple. The original implementation required depositing the sample on the curved surface of the hyper-lens. A more practical implementation of the super-lens has been theoretically proposed by another group (Reference 26). The concept is shown in Figure 8. The hyper-lens involves an array of thin metallic wires converging towards the tip. As is demonstrated, a dense array of metal wires separated by much less than the wavelength constitutes a metamaterial with the indefinite permittivity tensor. Specifically, the tensor component along the wires is given by:

$$\epsilon_{zz} = 1 - \omega_p^2 / (\omega^2 - k_z^2 c^2) \text{ and } \epsilon_{xx} = \epsilon_{yy} = 1, \tag{3}$$

where the z component is along the wires and perpendicular direction is normal to the wires. Because the only propagating waves are the TEM waves satisfying the  $\omega^2 = k_z^2 c^2$  dispersion relation, this meta-medium is strongly anisotropic and supports sub-wavelength waves which perform imaging. The spatial resolution is given by the spacing between wires. Figure 8 (right panel) shows the magnified image of a small ( $\lambda/25$ ) object placed at the tip of the hyper-lens. The magnification factor is 5x.

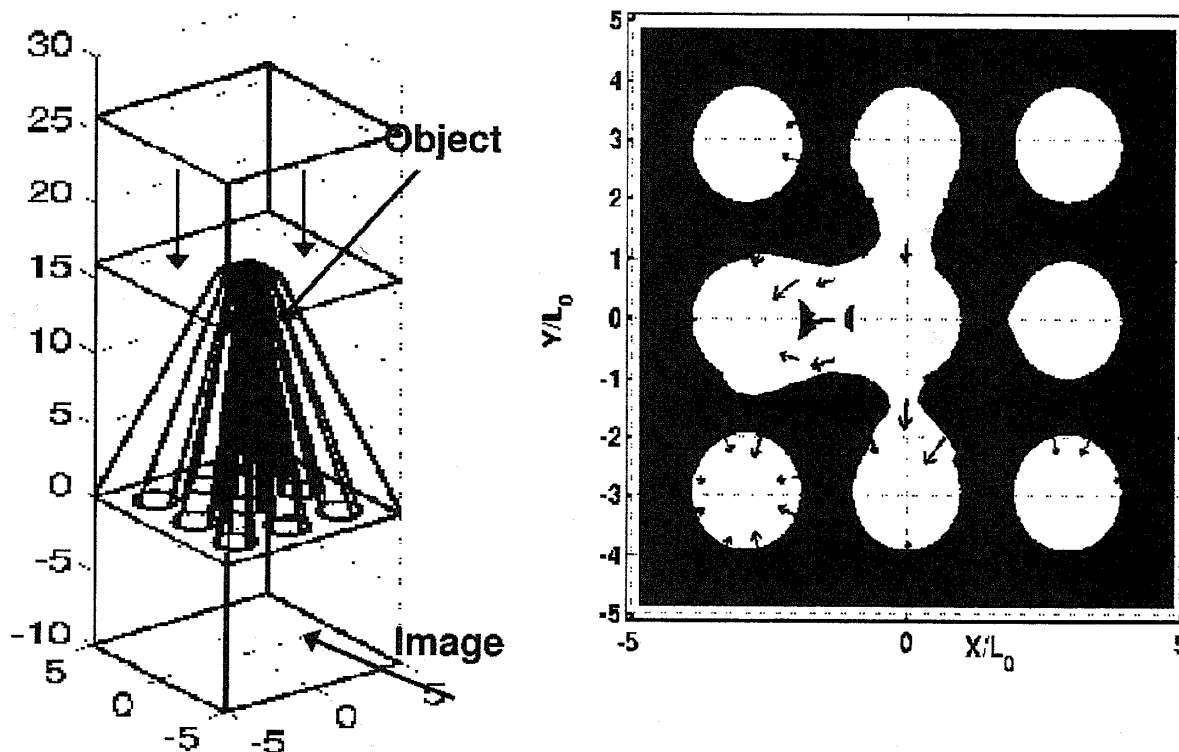


**Figure 8. Hyper-Lens Based on a Converging Array of Metal Wires.** A small object can be placed at the tip, illuminated from the top, and magnified by the expanding array of wires. Left panel: schematic. Right panel:  $\lambda/25$  object magnified by a factor 5x by the expanding hyper-lens. This hyper-lens can operate at mid-IR frequencies. (Reference 26)

Another concept for sub-wavelength imaging employing metamaterials is the so-called Far-Field Super-Lens (FSL). The concept is pioneered in Reference 27. The idea is



described in Figure 9. A sub-wavelength object (for example, two slits) is located at the bottom of a multi-layer super-lens. Another sub-wavelength grating is deposited on top of the super-lens. Because the super-lens (and for that matter, any indefinite permittivity material) is capable of propagating sub-diffraction waves, the electromagnetic perturbations created by the object are propagated through the super-lens upwards, until they encounter the sub-wavelength grating. At that point these sub-wavelength perturbations are diffracted on the image-releasing grating and converted into the far-field electromagnetic waves. Those far-field waves are collected by the objective of a microscope and observed through the eyepiece. The schematic is shown in Figure 9(a). Note that, again, there is no need for NSOM. The actual implementation of the FSL used the following object: a nanowire pair with 50 nm wide slit and 70 nm gap inscribed by focused ion beam on a 40 nm thick Cr film on the quartz substrate. Diffraction-limited image from a conventional optical microscope cannot resolve the two nanowires ( $NA = 1.4$ ,  $\lambda_0 = 377$  nm) as can be seen in Figure 9(c), but the FSL-equipped microscope can as shown in Figure 9(d).

Despite the success of this demonstration, there are serious issues involved in imaging sub-wavelength objects. Specifically it is pointed out in Reference 27 that multiple diffractive orders can become entangled, (that is, launched in the same direction into the far field). Disentangling these diffraction orders is very important. The payoff would be imaging of fully 2-D (flat) objects with a resolution smaller than the period of the image-releasing grating. More precisely, this ambiguity is illustrated by the right panel in Figure 10. If the sub-wavelength object is represented by the continuous spectrum (blue line), then the spectrum can be sampled within the discrete set of "zones" which are defined by the diffractive orders of the image-releasing grating. The width of each zone is  $2\omega/c$ , and they are labeled as 1<sup>st</sup> order, 2<sup>nd</sup> order, and so forth. Wave numbers belonging to the different zones can be diffracted onto the same far-field detector as explained in Figure 10. In order to disentangle the 1<sup>st</sup> and the 2<sup>nd</sup> zones, a single detector cannot provide sufficient information. It turns out that using two detectors (A and B) and two laser beams (Beam A and Beam B) provides additional information that is sufficient to disentangle the two zones. This additional information is obtained by comparing the intensity on the two detectors A and B. Another advantage of this imaging technique is that it is interferometric in nature. Therefore, even if the contribution of some of these spectral zones' orders is very weak, it can still be detected because of the high sensitivity of the interferometric techniques. What makes this interference special is that it involves sub-diffractive waves propagating through the indefinite permittivity metamaterial. Below some of the experiments conducted in the laboratory that demonstrate such interference are discussed.

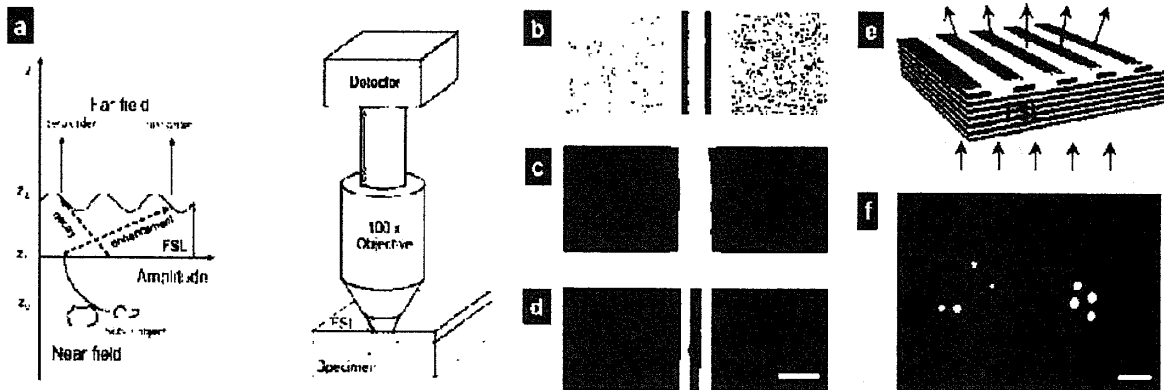


**Figure 9. FSL Based on an Indefinite Permittivity Metamaterial Placed Between the Object and the Image-Releasing Grating.** The grating releases into the far field sub-diffraction waves produced by light scattering off the object. The role of the metamaterial is to propagate sub-diffraction waves from object to grating. (Reference 27)

Ever since Merlin's invention (Reference 28) of the sub-diffraction near-field plate, it has become clear that the interference between sub-diffraction electromagnetic fields can result in the formation of a deeply sub-wavelength image. The near-field plate, however, is not an imaging device; its purpose is to create a well-defined image using an elaborate pre-fabricated sub-wavelength structure on the plate's surface. The goal for this study is to observe an a priori unknown sub-wavelength image using a near-field structure. In the past, successes (Reference 19) in retrieving images of sub-wavelength objects (such as  $\lambda/20$  holes) using an NSOM for radiation detection are achieved. An NSOM is a near-field instrument, therefore, a much more desirable detection method would involve far-field detection. To advance this goal, and to develop a tool sometimes referred to as the FSL, we've initiated research on multi-beam multi-detector sub-wavelength holography illustrated in Figure 10.

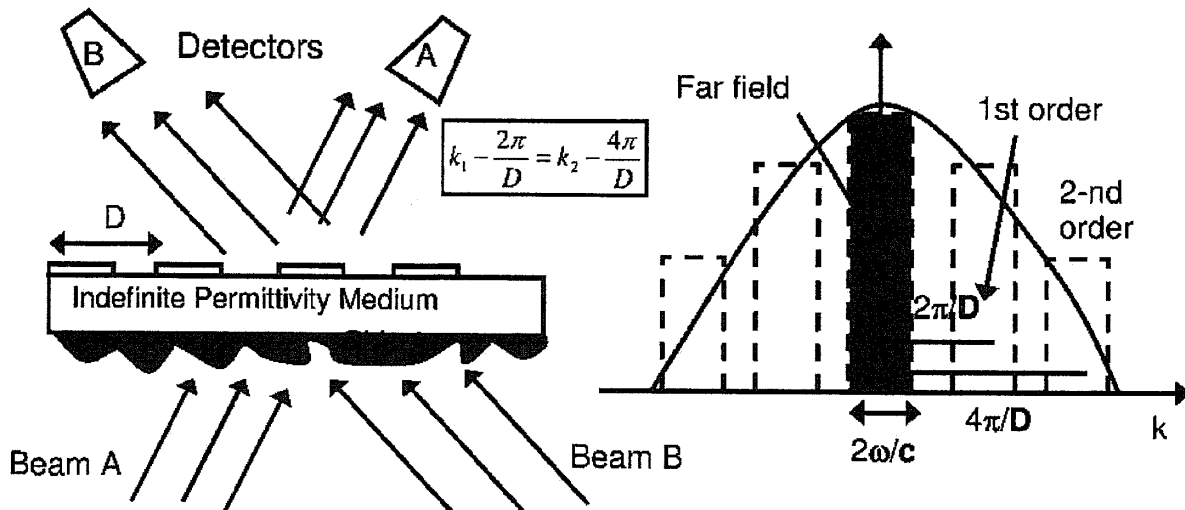


**Figure 10. Tomographic Multi-Beam Multi-Detector Holography of Sub-Wavelength Objects Using Indefinite Permittivity Medium (IPM).** Incident beam(s) scatter off the sub- $\lambda$  object, propagate through the IPM, and then get re-scattered into the far field by the grating with the period  $D$ . The purpose of the multi-detector arrangement is to disentangle the  $k_x$  and  $k_y$  spatial wave numbers in the object's spectrum (shown in the left panel). Beams A and B are phase-shifted with respect to each other.

Our implementation of the FSL utilizes an IPM whose dielectric permittivity tensor is anisotropic and contains positive and negative components:  $\epsilon_{\perp} > 0, \epsilon_{\parallel} < 0$ , where parallel refers to the IPM/object interface. We have already fabricated such IPMs using SiO<sub>2</sub>-SiC-SiO<sub>2</sub> multi-layer, and are investigating other approaches involving selectively-doped semiconductor multi-layers similar to the ones used by Gmachl's group at Princeton. SiO<sub>2</sub>-SiC-SiO<sub>2</sub> multi-layers are produced in-house (with SiC films shipped by Professor Ferro from University of Lyons, France). The main function of the IPM is to propagate sub-diffraction waves ( $k_{\parallel} > \omega/c$ ) with as little decay as possible. That happens because these sub-diffraction waves are no longer evanescent:  $k_{\perp}^2 \approx -k_{\parallel}^2 \epsilon_{\parallel} / \epsilon_{\perp} > 0$ . It is demonstrated experimentally that there exists a frequency range for which sub-diffraction waves propagate through the IPM with less attenuation than the radiation-zone waves ( $k_{\parallel} < \omega/c$ ), see Figure 11.

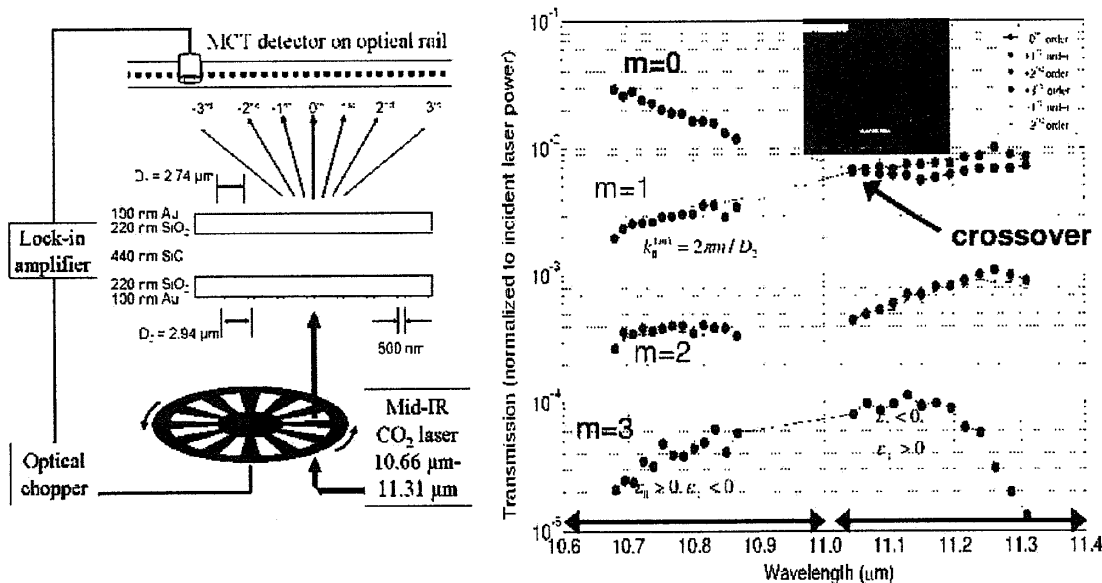


**Figure 11. First Experimental Demonstration of Propagating Sub-Diffraction Waves in the IPM.** (Left): Experimental setup demonstrating how sub-diffraction waves are launched into the IPM using FIB-fabricated sub-wavelength grating. Because the periods of the bottom (“launching”) and top (“transforming”) gratings are different, far-field observation of different harmonics of the bottom grating is enabled. (Right): Experimental results: the first sub-diffraction harmonic of the grating (green line) becomes stronger than the zeroth radiation-zone harmonic of the grating (blue line) in the region where  $\epsilon_{\perp} > 0, \epsilon_{\parallel} < 0$ .

Once sub-diffraction waves propagate through the IPM, they can diffract on the image-releasing grating (see Figure 10) and be radiated out into the far field. A detector array can be used to collect the signal and reconstruct the image. Unfortunately, different wave numbers  $k_{\parallel}$  of the object are directed into the same detector and produce an ambiguity in extracting their respective amplitudes  $A(k_{\parallel})$ . This ambiguity is illustrated by Figure 10: wave numbers  $k_1 = \Delta k + 2\pi / D$  and  $k_2 = \Delta k + 4\pi / D$  are directed to the same far-field detector. Simply put, a single number (intensity of light with the wave number  $\Delta k < \omega/c$  incident on the detector) is insufficient for determining two scattering

amplitudes ( $A(k_1)$  and  $A(k_2)$ ). Therefore, a new concept has to be developed, and the multi-detector technique is such a concept.

The concept requires two detectors and two coherent laser beams. The two beams are formed using a beam-splitter and a variable delay line imparting a phase shift to the two beams (see the actual experimental photograph in Figure 13 where the beam-splitter BS and the Delay Line are shown). We have theoretically demonstrated that the intensity dependences of the two detector intensities  $I_1(\psi)$  and  $I_2(\psi)$  as a function of the phase delay  $\psi$  provides enough information to recover both  $A(k_1)$  and  $A(k_2)$ .

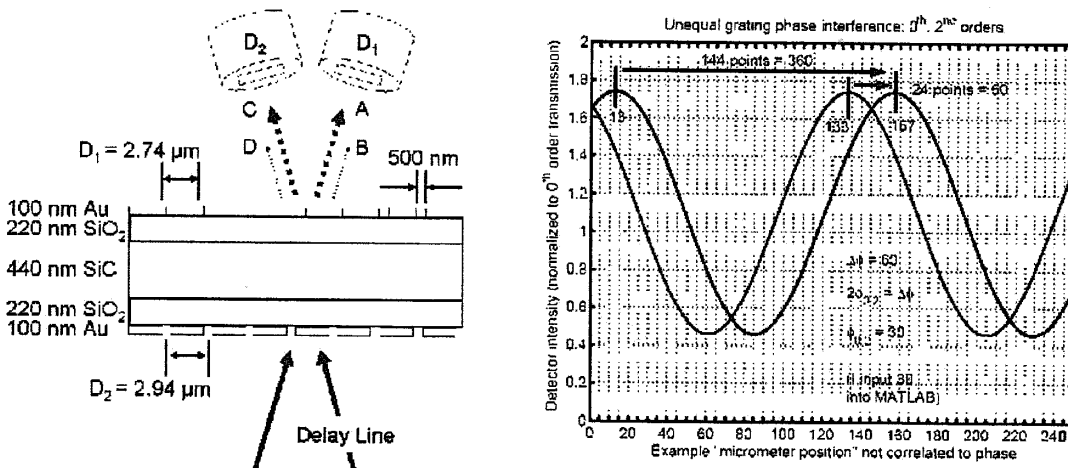


**Figure 12. (Left): Schematic for 2-Beams/2-Detectors Interferometric Measurement. (Right): Numerical Simulation:** intensity on the two detectors as a function of the phase delay between beams A and B produced by the interference between the zeroth and first diffractive orders of the bottom diffractive grating (numerical simulation). The second detector provides the necessary second data point which is necessary for separating the contributions of different diffractive orders.

Two sets of experiments demonstrating the feasibility of the concept are conducted. None of these experiments constitutes imaging per se. However, without demonstrating the two key milestones described below, proper imaging experiments cannot be attempted.

The first milestone involves demonstrating that IPM indeed supports propagating (non-evanescent) sub-diffraction waves. Figure 11 shows the experimental schematic (left panel) and experimental results. The bottom grating "imprints" its Fourier components (zeroth, first, second, third, and so forth) onto the incident laser pulse thereby generating electromagnetic waves that are launched into the SiC-based IPM. The zeroth harmonic is inside the radiation zone (that is, it is not sub-diffraction), while the first, second, and so forth sub-diffraction. These EM waves scatter off the top grating having a slightly different period and are released into the far field. Because the direction in which waves are released depend on the Fourier harmonic's number, we can experimentally separate and measure them. Clearly, the relative magnitudes of these diffractive orders dramatically vary as a function of the laser wavelength. For example, the zeroth diffraction order clearly dominates in the  $\epsilon_{\perp} < 0, \epsilon_{\parallel} > 0$  frequency range.

However, in the  $\epsilon_{\perp} > 0, \epsilon_{\parallel} < 0$  frequency range the first diffractive order becomes larger

than the zeroth one. This confirms the recently predicted effect that for IPMs one can indeed observe a very counterintuitive effect: sub-diffraction waves can indeed propagate with less loss than the diffraction-limited ones.

The second milestone involves demonstrating the possibility of observing the interference of sub-diffraction electromagnetic waves inside the IPM using the two-beam/two-detector technique. Figure 10 demonstrates this interference pattern which reveals the phase advance of the sub-diffraction waves inside the IPM. While we have so far demonstrated the interference between the first Fourier component of the grating (sub-diffraction) and the zeroth Fourier component, we see the possibility of interfering even more sub-diffraction waves (2<sup>nd</sup> and 3<sup>rd</sup>).

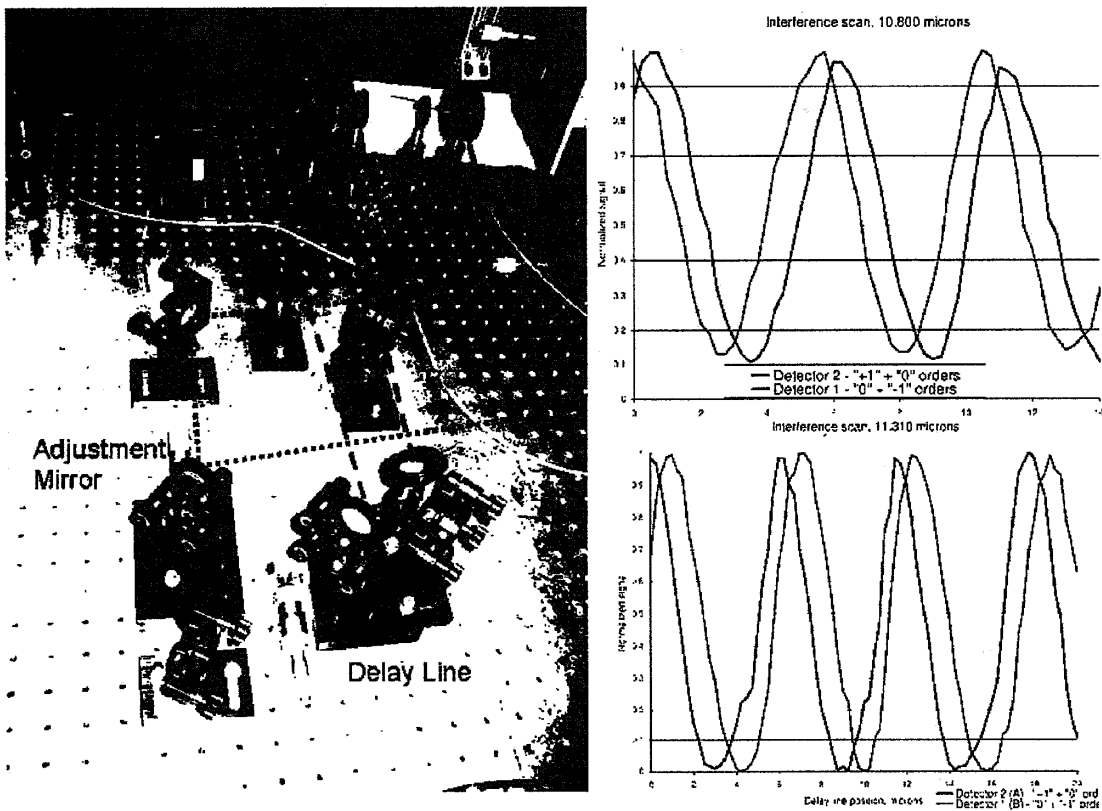


**Figure 13. (Left): Experimental Setup for 2-Beams/2-Detectors Interferometric Measurement in Our Lab. (Right): Preliminary Experimental Results:** infrared intensity on two detectors (red and black lines) are (i) different from each other; (ii) have a sinusoidal dependence on the delay line position (in microns), which is equivalent to the phase delay between the two beams; (iii) are shifted in phase by the amount equal to twice the phase difference between the 1<sup>st</sup> order (sub-diffraction) and 0<sup>th</sup> order (radiation zone) Fourier components of the bottom grating. Measurements taken at  $\lambda = 10.8 \mu\text{m}$  and  $\lambda = 11.3 \mu\text{m}$ .

With these two milestones established, it is now possible to conduct true sub-wavelength imaging experiments using two (or more) far-field detectors and jointly processing their inputs.

## Applications to Circuits and Waveguide Miniaturization: Slowing Down and Manipulating Electromagnetic Pulses (EMP) Using Advanced Metamaterials

Given the space constraints of an advanced aerospace platform and the amount of the useful payload that has to be carried, it is very important that every optical and microwave component be as small as possible. Because of the very large speed of light, there is a natural limit to how small such components can be made. Any structure capable of processing EMPs (be those optical, THz, or microwave) of temporal duration  $\tau$  must be at least  $L = c\tau$  long. For example, a 1 ns microwave pulse can be manipulated inside a device that is at least 1 ft long. Pulse manipulation can be understood very broadly by pulse compression, frequency shifting, harmonics generation, or other. For aerospace communications systems, it may be very desirable to have the ability to manipulate the format of EMPs, (that is, to change their frequency, duration, and repetition rate). Slowing down or even stopping the EMP can circumvent the length requirement if the group velocity is reduced to  $v_g \ll c$ , and thus the required length is  $L = v_g \tau$ .

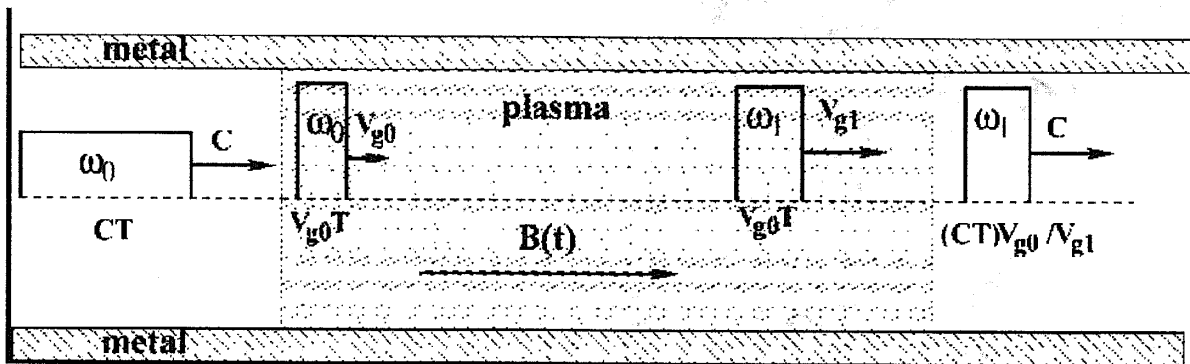


**Figure 14. Schematic of Pulse Compression in Magnetized Plasma.** A radiation pulse with initial frequency  $\omega_0$  and duration  $T$  slows down in the plasma to a group velocity  $v_{g0} \ll c$ . Adiabatic spatially uniform variation of the magnetic field changes the radiation frequency to  $\omega_1$  and increases the group velocity to  $v_{g1} \gg v_{g0}$ . The emerging pulse is compressed to  $T_1 = T v_{g0} / v_{g1}$ . (Reference 29)

An example of the pulse slowing down and subsequent manipulation is first discussed in Reference 29 in the somewhat esoteric context of magnetized plasma. Pulse duration, frequency, and (for multiple pulses) repetition rate can be controlled by storing (or slowing down) electromagnetic waves and subsequently changing the system's parameters. The essence of the compact pulse manipulator is shown in Figure 14. The pulse is slowed down inside the compact plasma device and manipulated by changing the magnitude of the magnetic field. The advantage of slowing the pulses down is three-fold. First, the device can be made smaller, resulting in size savings. Second, the temporal scale on which the system has to be manipulated is lengthened because the pulse is moving slowly. Finally, the potentially large ratio between  $v_{g1} \gg v_{g0}$  results in the more dramatic dynamic range of possible pulse compression ratios. Plasma-based

devices may not be appropriate in the aerospace context because of their large size, power requirements, large magnetic coils, and so forth.

Fortunately, metamaterials offer some exciting opportunities for slowing down electromagnetic waves as has been recently recognized (Reference 30). Specifically, the authors have theoretically demonstrated that an axially varying heterostructure with a metamaterial core of negative refractive index can be used to efficiently and coherently bring light to a complete standstill. One of the most remarkable aspects of the approach is that it works for relatively broadband pulses. The broadband capability is achieved through "tapering" (or axial variation) of a metamaterial's parameters such as the effective  $\epsilon$  and  $\mu$ . Due to tapering, each frequency component of the wave packet is stopped at a different guide thickness, leading to the spatial separation of its spectrum and the formation of a 'trapped rainbow'. In Reference 30, the authors have actually opted for a physical tapering of the waveguide (that is, reducing the thickness of the NIM waveguide along the length of the waveguide), although other approaches such as varying  $\epsilon$  and  $\mu$  will also work.

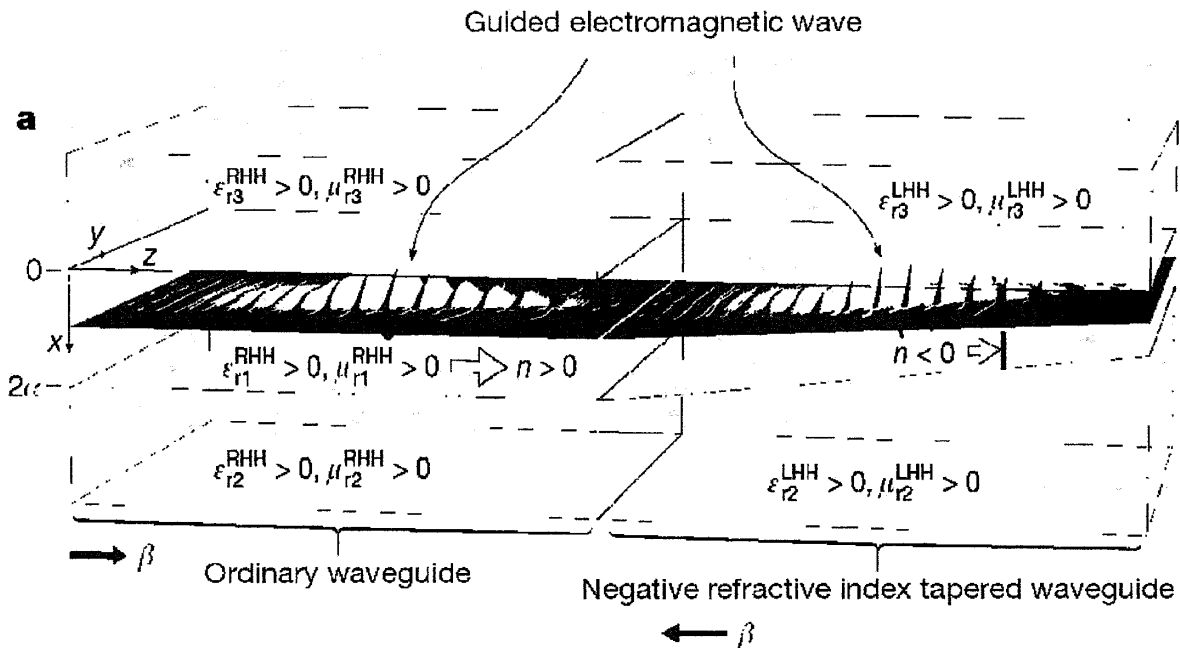


**Figure 15. Trapped Rainbow: A Waveguide with Negative Index Core Can Stop Light.** A guided wave packet is efficiently injected from the ordinary waveguide to the left-handed heterostructure LHH (see also Figure 4), inside which it propagates smoothly owing to the slow (adiabatic) reduction in the thickness of the core. The smallest (red) frequency components of the wave are stopped at the smallest core thicknesses of the LHH, while the largest (blue) components stop at correspondingly larger core thicknesses. (Reference 30)

The schematic of the light-stopping structure based on the waveguide with a negative index core (dubbed left-handed heterostructure, or LHH, in Reference 30) is shown in Figure 14. Although light stopping is possible in other guided configurations that do not necessarily require  $\mu$  to be negative (for example, a metal-dielectric-metal waveguide would suffice), the key here is that perfect impedance matching can be achieved for the metamaterials-based waveguides with the negative index core. That is very important for maximizing the coupling efficiency from the regular waveguide to the LHH. Although Reference 30 does not present any specific ideas as to what could be done with the

slowed down and/or stopped light, the schematic shown in Figure 13 provides some key ideas. Moreover, the prospect of producing a low-loss negative index material in the optical domain still remains somewhat distant. Therefore, it may be worthwhile to examine other approaches to slowing down light that have emerged in the past few years.

Stopping and/or slowing down light is an old idea originating from the atomic concept of Electromagnetically Induced Transparency (EIT). The phenomenon has been considered to be purely quantum mechanical until several groups have demonstrated that it has some classical analogies (Reference 31). Remarkably, at least one group has demonstrated in the past year that EIT can be achieved using plasmonic metamaterials (Reference 32). The idea is to create a plasmonic "molecule" consisting of a radiative element coupled with a subradiant (dark) element. The plasmonic molecule showed electromagnetic response that closely resembles the electromagnetically induced transparency in an atomic system. Because of its subwavelength dimension, this electromagnetically induced transparency-like molecule was shown to be suitable as a building block to construct a "slow light" plasmonic metamaterial. The specific design of the plasmonic molecule is shown in Figure 15.

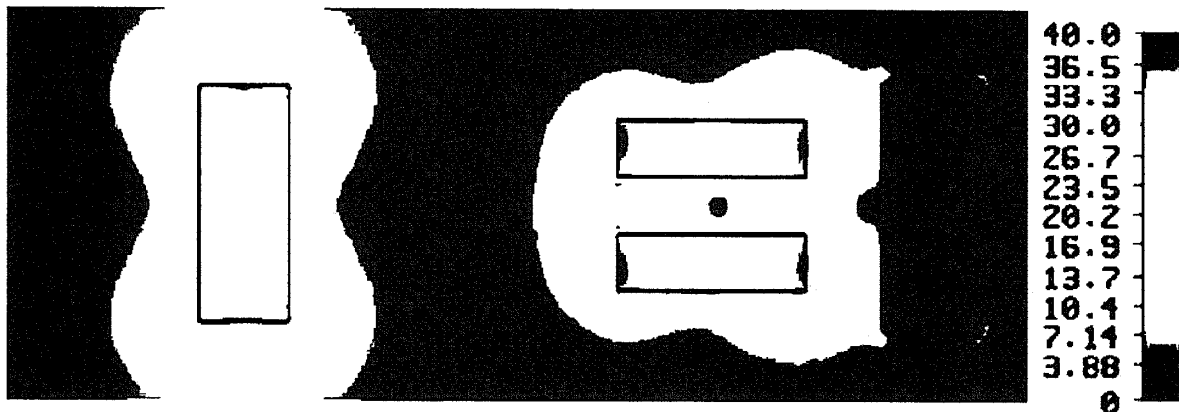


**Figure 16. "Plasmonic Molecule" Exhibiting EIT.** Left: Radiative element (metal strip) by itself gets strongly polarized by the incident EM wave, resulting in weak transmission/strong reflection. Right: Radiative element coupled to the "dark" element (two strips). Dark element possesses a non-radiative quadrupole resonance which is excited by the radiative element and de-polarizes the radiative element. The result: vanishing reflection, high transmission. Color bar:  $\left| \frac{E}{E_0} \right|$  normalized to the incident laser field at  $\lambda = 700$  nm. (Reference 32)

This specific plasmonic molecule consists of the "dark state" (two parallel plasmonic antennas oriented perpendicular to the incident vertical electric field) and the "radiative state" (single plasmonic antenna oriented parallel to the electric field). The quality factor of the "dark antenna" state is an order of magnitude higher than that of the "radiative" antenna. When the "radiative" antenna is spatially separated from the "dark" antenna (or when the dark antennas are not present at all), all or most of the incident radiation is reflected from an array of "radiative" antennas whenever the resonance frequency of the antenna coincides with that of the laser. In this example, the long antenna is 128 nm long, and the resonance wavelength is at  $\lambda = 700$  nm. The key effect here is that the resonance of the "dark" antenna should be at the same wavelength.



Because the exploited resonance has a quadrupole nature, it is slightly red-shifted. For that reason, the length of the "dark" antenna is 100 nm. When the two antennas are brought together, the radiative antenna polarizes the dark antenna, which, in turn, depolarizes the radiative antenna. As a result, the dipole moment of the coupled system is drastically reduced, the reflection drops and transmission increases to almost 100 percent (limited only by losses). Most of the energy is now stored inside the non-radiative (dark) antenna.

If multiple layers of dark/bright antennas are employed as shown in Figure 16, then one can achieve one of the most important manifestations of EIT; "slow" light. Slow light can have many interesting technological applications because (a) slow light is easy to manipulate by changing the structure's parameters (as described in the section on tunable metamaterials), and (b) slow light has a high field intensity (enhanced by the ratio of the free-space propagation speed to the slow propagation speed), therefore, all nonlinear processes are enhanced for slow light. Such nonlinear processes may include harmonics generation, optical diode action (see the section on non-reciprocal optical elements), and many others.

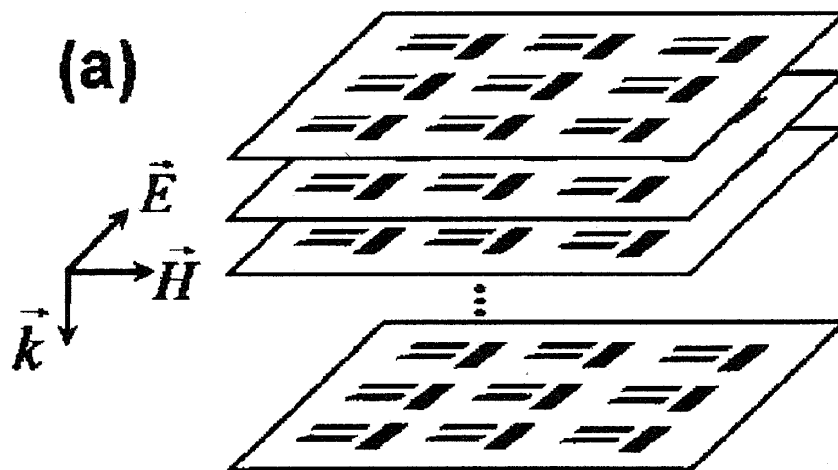


**Figure 17. True Multi-Layer Metamaterial With a Unit Cell Shown in Figure 15:** radiative antenna (single metal strip) coupled to a dark antenna (two perpendicular metal bars). Such metamaterial exhibits "slow" light propagation along the incidence direction (slowed down by a factor 30 or more). (Reference 32)

It is important to realize that the geometry suggested in Reference 32 is not unique. For example, the dark and radiative antennas need not reside in the same plane. Nor is the effect of EIT (and the related phenomenon of slow light) limited to the optical domain. Both infrared and microwave-range designs have started emerging. These frequency domains are likely to be of greater use for advanced aerospace platforms than the visible range targeted by most studies.

## Metamaterials for Energy Harvesting

One of the most important applications of metamaterials is related to developing "perfect absorbers" of infrared electromagnetic radiation, be it in the mid-to-long infrared part of the spectrum (making it relevant for night vision, harvesting of the Earth glow mid-infrared radiation, and so forth) or in the near-to-mid-IR spectrum (making it relevant for day-time infrared photography of the earth terrain). For example, day-time infrared photography relies on the different sunlight reflectivities of surfaces (for example, snow, brick walls, concrete walls, grass, and so forth), and can easily distinguish between those surfaces. This reflectivity differential tends to be the greatest between 2-3 microns, and rapidly decays toward longer wavelengths. Open sky contains very little infrared radiation which explains why infrared imaging/photography is very important for aerial and satellite surveys. Because light scattering in the atmosphere scales as  $\lambda^{-4}$ , imaging through the atmosphere in the visible range is impossible, and infrared imaging becomes important. This is especially true for the  $1 < \lambda < 4 \mu\text{m}$  range. For longer wavelengths ( $\lambda > 10 \mu\text{m}$ ) this brightness differential is largely gone because the emission spectrum is dominated by thermal emission. In fact, the Earth glow maximum is around  $\lambda > 10 \mu\text{m}$ , with most of the energy contained in the  $3 \mu\text{m} < \lambda < 14 \mu\text{m}$  range. This longer wavelength (mid-to-far IR) spectral range is also very important. It can be used for night-time energy scavenging by high-altitude satellites and other aerospace platforms.

There has been a surge of activity in this area, first in the microwave/THz part of the electromagnetic spectrum (References 33, 34), and subsequently in mid-to-far infrared (Reference 20). The concept of narrow-band metamaterials-based absorbers introduced in Reference 33 has the potential for developing highly efficient bolometer arrays. When applied to the infrared part of the spectrum, it can be used for space navigation, especially when weak infrared signals from specific stellar objects need to be picked up and discriminated from other radiation sources. For such applications, the narrow-band "perfect" absorption is highly suitable. An array of such bolometers would reject (reflect) all undesirable frequencies and focus on the single wavelength characteristic of the source of interest. Moreover, if an array of different (for example, tuned to different frequencies) narrow band detectors can be deployed, then the hyper-spectral imaging capability could bring additional benefits. For example, absolute temperatures of a radiation source (that is, stellar bodies) could be accurately determined, and could improve the accuracy of space navigation further.

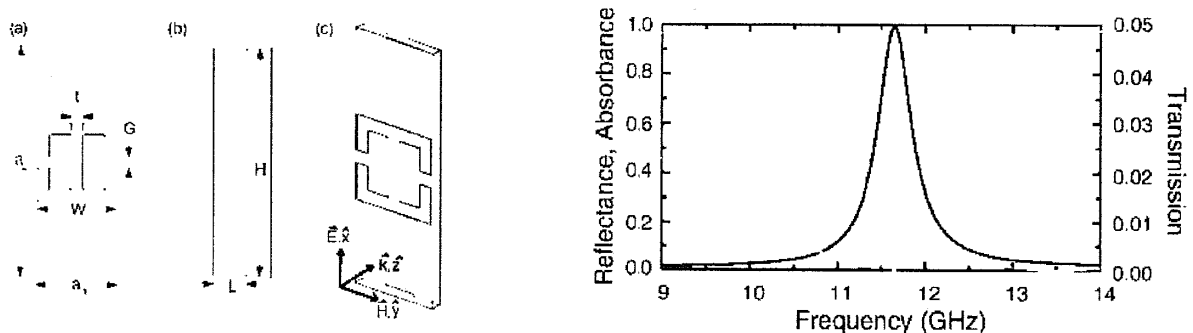


**Figure 18. "Perfect" Narrow-Band Microwave Absorber.** (a-c): Unit cell design. Right panel: simulated absorption/transmission/reflection. (Reference 33)

One possible design for the microwave frequency band is shown in Figure 17. High absorption is accomplished by reducing reflections to zero. This is accomplished by choosing metamaterials parameters such that  $\epsilon_{eff}(\omega_r) = \mu_{eff}(\omega_r)$  at the resonant frequency  $\omega_r$ . Note that both the real and imaginary parts of the permittivity and permeability must be equal to each other, and that the imaginary parts don't necessarily need to be small for absorber applications. In fact, it is desirable that they are not too small, thereby enabling 100 percent absorption within a single layer of metamaterial. The above design can be scaled down to the THz range, as was later demonstrated in Reference 34. It is difficult to find strongly absorbing materials at THz frequencies that are compatible with standard photolithography. Thus, a potential application of these metamaterial structures is as absorbing elements in thermal detectors. A strong absorption coefficient is also necessary to have a small thermal mass. This is important for optimizing the temporal response of thermal detectors. The metamaterial presented here has a 6 micron thick film (that is,  $\lambda/50$  thickness for THz radiation) and 70 percent absorptivity, which yields an absorption coefficient of  $2000 \text{ cm}^{-1}$ .

One drawback of the original design was the narrow angular range of the absorber. The absorption dropped dramatically when the incidence angle was as small as 20 degrees. The reason for that is a relatively large unit cell of the metamaterial. In fact, when the unit cell size is larger or comparable to  $\lambda/2n$ , where  $n$  is the refractive index of the substrate, it is inappropriate to call such structure a "metamaterial". A true impedance-matched metamaterial would, in fact, always have a very broad angular response.

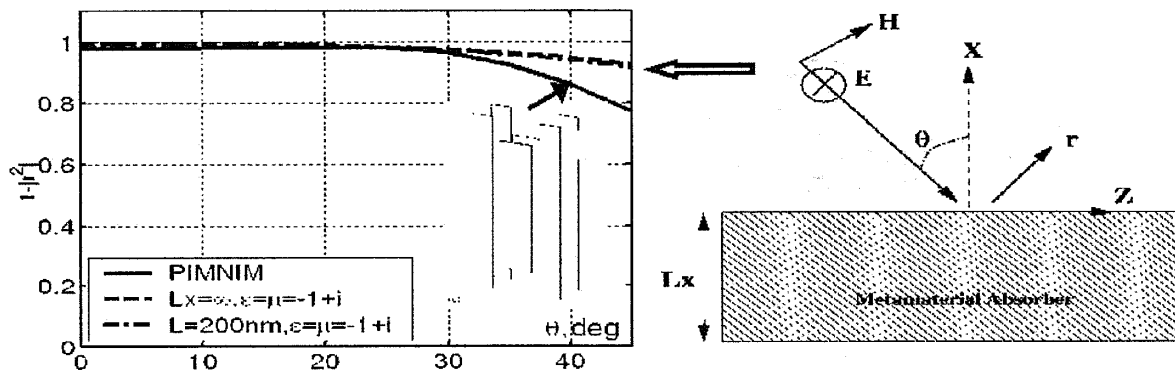


**Figure 19. Wide-Angle Plasmonic Absorber Based on Negative Index Metamaterial.** Right panel: schematic of an absorption-measuring experiment. A generic metamaterial with  $\epsilon_{yy} = \mu_{zz} = -1 + i$ ,  $\mu_{xx} = 1$  is assumed. Left panel: angular dependence of the absorption for a generic and specific (shown in the inset) metamaterial. Both exhibit wide-angle absorptivity. (Reference 20)

This fact can be expressed by a simple formula for the absorption coefficient  $A$  (Reference 20):

$$A = 1 - \frac{\left| \frac{\cos \theta - \sqrt{\epsilon_{yy} / \mu_{zz} - \sin^2 \theta} / (\mu_{xx} \mu_{zz})}{\cos \theta + \sqrt{\epsilon_{yy} / \mu_{zz} - \sin^2 \theta} / (\mu_{xx} \mu_{zz})} \right|^2}{(4)}$$

where we've assumed that, for normal incidence, this metamaterial is impedance-matched:  $\epsilon_{yy} = \mu_{zz} = -1 + i$ . Equation 4 can be simplified under the assumption of  $|\epsilon_{yy}| \gg 1, \mu_{xx} = 1$ :  $A \approx 1 - \tan^4(\theta/2)$ , implying that  $A \approx 0.97$  even for  $\theta = \pi/6$ . The challenge, if course, is to design a true impedance-matched optical metamaterial. Success has been achieved in designing such a metamaterial (Reference 20).

The recently published design is shown in Figure 19. The unit cell consists of two layers of plasmonic antennas; the cut-wire antenna that imparts magnetic (as well as some electric) response to this metamaterial, and the continuous-wire antennas that impart a purely electric response. It is found that the wide-angle capability could be very important for several applications. Wide-angle power absorption efficiency is desirable for miniaturizing photodetectors or microbolometers down to the wavelength size.

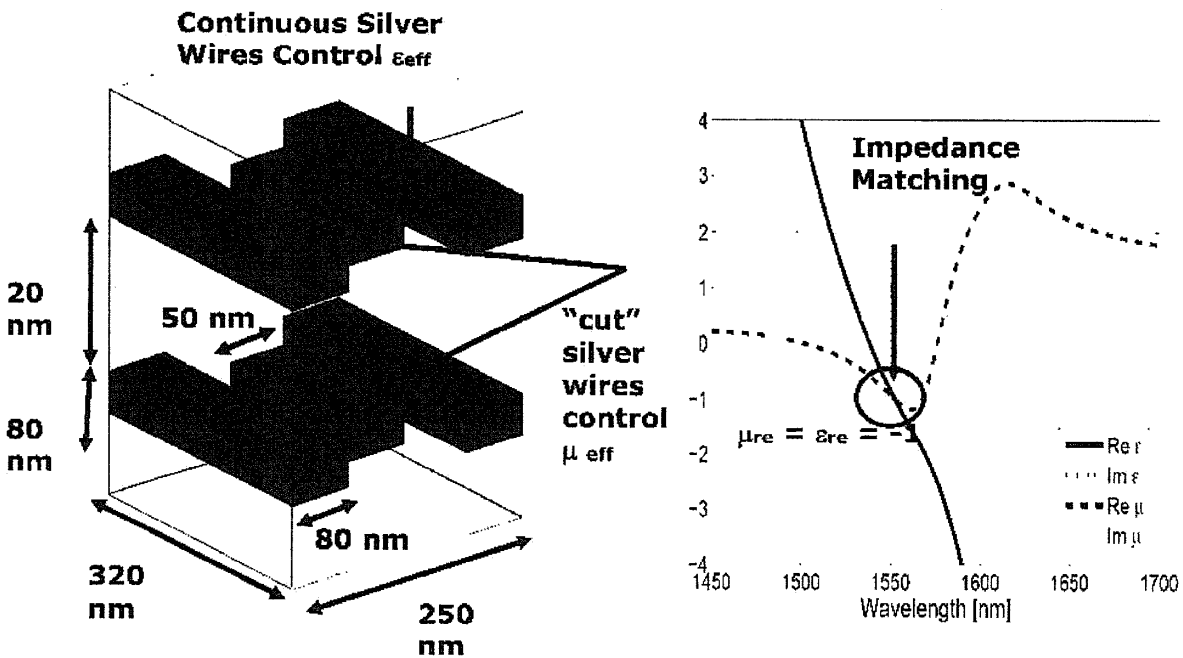


**Figure 20. Specific Design of a Wide-Angle Plasmonic Absorber Based on Negative Index Metamaterial Operating at  $\lambda=1550$  nm.** Left panel: Schematic of the silver-based plasmonic structure. Right panel: Extracted permittivity and permeability for the normal incidence demonstrate impedance matching:  $\epsilon_{yy} = \mu_{zz} = -1 + i$ . (Reference 20)

For example, to focus light on a wavelength-sized photodetector or micro-bolometer requires high-NA optics (a NA=0.5 or higher). Therefore, a photodetector should be able to absorb light incident at 30 degree angle. For advanced aerospace platforms it is easy to envision a scenario where an airborne platform is powered by a high-power infrared laser source located on Earth. If the wavelength falls inside the transparency window of the atmosphere (between 3 and 4  $\mu\text{m}$ , and also around 10  $\mu\text{m}$ ), then such a

prospect is not too farfetched because scattering in mid-infrared by atmospheric gases is essentially zero. For such a remote powering scenario to be feasible, one would need a highly efficient absorber at the specific wavelength corresponding to that of the source. Moreover, as the space platform is moving, it is desirable that the absorption remain high even for non-normal incidence angles.

The second application is for thermophotovoltaics (TPV) (Reference 35). Some type of thermophotovoltaic converter will almost undoubtedly be installed on the advanced aerospace platforms of the future. Presently even advanced (experimental) electric cars are using TPV cells to convert the heat from their engines into electricity. Such converters have already been shown to be capable of increasing the range of electric vehicles by a factor of 3. We believe that metamaterials could play an important role in developing highly efficient TPV cells. By virtue of Kirchhoff's law, emissivity of a thermal emitter approaches the blackbody limit only if the absorptivity approaches unity. Moreover, wavelength-selective radiators can dramatically improve the efficiency of current generation in a TPV cell if their emission spectrum is matched to the bandgap of the TPV converter. For example, a typical TPV converter, GaSb, has the bandgap of EG = 0.7 eV that would be ideally suited to a wavelength-selective radiator operating in near infrared around  $\lambda = 1.7 \mu\text{m}$ .

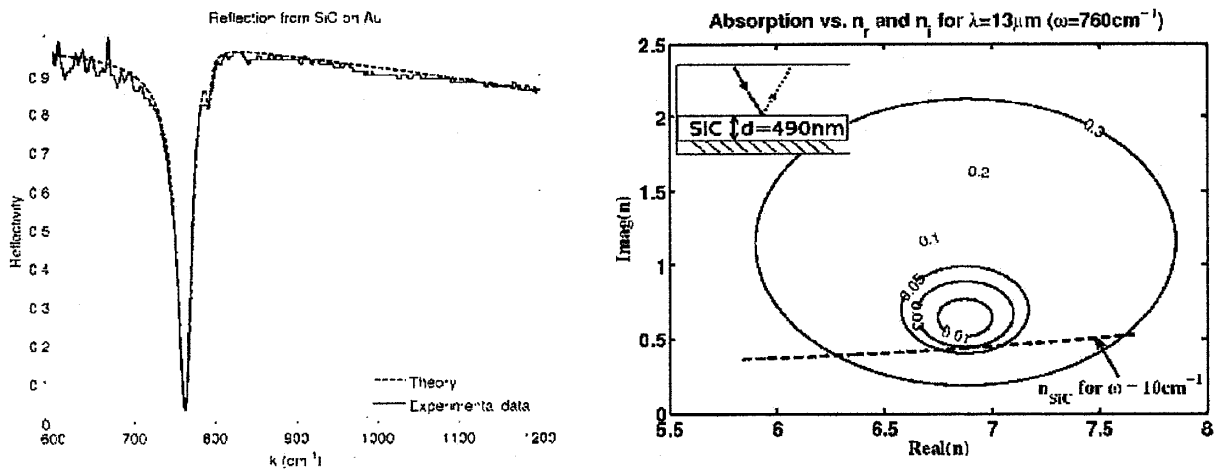


**Figure 21. (Left) Experimental Result, Reflectivity Versus Wavelength, that Inspired the Proposed Effort: A Modestly Absorbing Material (SiC) Turns Into a "Perfect Mid-IR Absorber" When a  $\lambda/4$ -Thick SiC Film Is Backed by a Metal Mirror. (Right): Theoretical Plot - Constant Reflectivity Contours Plotted in the  $(\text{Real}(n), \text{Imag}(n))$  Space. High material absorptivity  $\text{Imag}(n)$  is required to achieve perfect absorption ( $R=0$ ). Posed question: can a metamaterials-based semi-transparent mirror enhance absorption and result in an almost-perfect ultra-thin absorber?**

The perfect absorbers shown in Figures 17-19 may be too complex for practical applications. Metamaterials tend to be lossy because of the large field concentration in the metal. Therefore, work has recently started working on a new type of metamaterial (so-called CMMs mentioned in the Introduction), that could potentially make weakly-absorbing semiconductors (that is, Si in the visible) absorb much stronger. The goal here is to make a thin (although not necessarily a very sub-wavelength) absorber backed up by a sheet of CMMs which would prevent reflections and result in a very high absorption. Applications that are considered are essentially the same as for the "perfect" absorbers described above. For example, satellites can use the Earth glow for nighttime battery recharging. The collected power is quite high; 1 m<sup>2</sup> of black surface at